FABRICATION AND CHARACTERIZATION OF SHAPE MEMORY ALLOY (SMA) - MAX PHASE BILAYERS AND COMPOSITES

A Dissertation

by

ANKUSH DILIP KOTHALKAR

Submitted to the Office of Graduate and Professional Studies of
Texas A&M University
in partial fulfillment of the requirements for the degree of

DOCTOR OF PHILOSOPHY

Chair of Committee,	Ibrahim Karaman
Co-Chair of Committee,	Miladin Radovic
Committee Members,	Dimitris Lagoudas
	Karl T. Hartwig
Head of Department,	Ibrahim Karaman

December 2015

Major Subject: Materials Science and Engineering

ABSTRACT

With the rapid growth of the transportation industry (automotive and aerospace), the demands for the control of noise and enhancing the stability of structures, through the development of high damping materials are continually increasing. In the last two decades, increasing attention is being given to develop high damping materials for various applications. The aim of this study is to develop high damping material by combining these two unique material systems, a NiTi (SMA) with a Ti_3SiC_2 (MAX phase) which are individually excellent materials for damping applications. Another goal here is to investigate whether large recoverable shape change in SMAs during thermo-mechanical cycling can generate residual stresses and defects that could further enhance damping capability of the novel SMA-MAX phase composites.

In this study, NiTi-Ti_3SiC_2 composites are processed using spark plasma sintering (SPS) technique and microstructurally characterized using scanning electron microscopy (SEM) to study the distribution of NiTi, Ti_3SiC_2 and remnant porosity in the composite. The highest energy dissipation is observed for the thermo-mechanically cycled (TC) composite followed by the as-sintered (AS) composite, pure NiTi and pure Ti_3SiC_2 when compared at the same applied stress levels. Both the AS and TC composites exhibited higher damping up to 200 MPa stress than any of the metal – MAX phase composites reported in the literature to date.

Interfaces play a crucial role in determining the overall properties and performance of the composites. Bulk components of NiTi (SMA) and Ti_3SiC_2 (MAX phase) are successfully joined using pressure assisted diffusion bonding. Interfaces thus formed are micro-structurally characterized where the interfacial structure consists of NiTi / Ti_2Ni / Ti_5Si_3 / NiTiSi / Ti_3SiC_2. Nano-indentation showed that the elastic moduli of the phases in the interface are close to that of Ti_3SiC_2 while their hardness is higher than that of both Ti_3SiC_2 and NiTi.

Four-point bend delamination tests are used to study the fracture behavior of the NiTi-Ti_3SiC_2 interface under mixed mode loading configuration for bilayer specimens. NiTi starts to deform plastically in the region between the inner loading points prior to crack propagation suggesting the formation of strong, tough interface. This is contrary to most literature studies wherein crack propagation occurs prior to onset of plastic deformation in the metallic phase, because of the weak interface. Thus, this study demonstrates the interplay between the interfacial and yield strength of the metallic phase in determining interfacial fracture behavior. Fracture occurs along the interface between Ti_3SiC_2 and NiTiSi phase, occasionally inside the Ti_3SiC_2 phase and also in the different phases in the reaction layer. Formation of strong interface enables efficient load transfer between SMA and MAX phase leading to the observation of excellent damping in composites. In conclusion, this study demonstrates the potential of novel SMA-MAX phase composites for high damping applications.

DEDICATION

To my family and friends for their support, sacrifice and patience.

ACKNOWLEDGEMENTS

I would like to begin by thanking my advisor and research mentor, Dr. Ibrahim Karaman. It is his guidance, support, encouragement, and caring personality that made my doctoral journey exciting and fruitful. Whenever I needed him, he was there for me. He always encouraged me to think independently and ask questions, backed me up no matter what happened, gave me the freedom to pursue my ideas and was encouraging even when things did not work as planned. He provided me ample opportunities to travel to attend conferences and summer schools. It gave me a chance to meet eminent researchers, peers and develop a broad understanding of materials science and engineering. He is a constant source of encouragement and motivation for me. I feel privileged and honored to get a chance to complete my doctoral degree under his guidance. For this, I remain forever indebted to him.

Next I would like to thank for my co-advisor, Dr. Miladin Radovic for his excellent and thought provoking insights on my research. He taught me how to think about a problem at a very fundamental level. After every research meeting with him, I felt excited about the prospects and potential of my current and future research. One can never leave his office without getting excited about the possibilities for future work.

I would like to thank my committee members, Dr. Dimitris Lagoudas and Dr. Karl Ted Hartwig for their willingness to serve on my committee and provide valuable

feedback. It is because of Dr. Lagoudas that I understood the importance and usefulness of collaboration in research.

I would like to thank Dr. Indranil Manna, who guided and mentored me during my short stint as a summer research fellow at IIT Kharagpur. It was his encouragement and support that led me to pursue graduate school. Thank you to Dr. Krishanu Biswas, my undergraduate thesis supervisor who taught me the fundamentals of scientific research. I would like to thank Dr. Charudatta Galande for guiding me during the application process for graduate school.

A big thank you goes to Dr. Sandip Basu, who helped me a lot in early days of my graduate life and made my transitions, from being an undergraduate to a graduate student, smooth. I consider myself lucky to find a research mentor in the form of friend very early on, in my graduate life. I would like to thank my MURI project collaborators, Dr. Brian Lester, Dr. Ross Mclendon, Keith Ballard, Hieu Truong, Huili Gao and their then advisors, Dr. John Whitcomb, Dr. Ozden Ochoa. Collaboration with the modeling groups helped me get a very different perspective from the one that of an experimentalist. Thanks to Dr. Alper Cerit for helping me out with experiments on joining and interfacial characterization. A special thanks to Dr. Liangfa Hu and Dr. Rogelio Benitez for helping me out with the materials processing and testing, necessary for carrying out experiments for my doctoral degree. I learned a lot about work ethics and commitment from Dr. Liangfa Hu. I learned a lot about hands on laboratory work and how to fix things in the laboratory from Dr. Rogelio Benitez.

Next I would like to thank all the current and past MESAM group members who made working in the laboratory exciting and fun. Just by being around the energetic researchers in the laboratory, I got to learn a lot about experimental hands on research. Thanks to Dr. Ji Ma, Dr. James Monroe, Dr. Ebubekir Dogan, Dr. Ruixian Zhu, Dr. Nevin Ozdemir, Dr. Kadri Can Atli, Dr. Pinar Karpuz, Dr. Alper Evirgen, Dr. Li-Wei Tseng, Dr. Nick Bruno, Dr. Shu Juan Wang, Dr. Anup Bandopadhyay, Sonia Razavi, Murat Kaynak, Nick Barta, Ceylan Hayrettin, Brian Franco, Hande Ozcan, Matthew Vaughan, Omer Karakoc, Wahaz Nasim and Michael Bass. Thanks to Dr. Radovic's research group members Pradeep Gudlur, Peipei Gao, Amy Bolon, Patrick Mahaffey, and Matthew Westwick.

I would like to thank other faculty and research staff at Texas A&M University, for helpful discussions and teaching me characterization equipment respectively, starting with Dr. Raymundo Arroyave, Dr. Ray Guillemette, Dr. Hansoo Kim, Tom Stephen and Rodney Inmon. Thanks to all the materials science and engineering department staff starting with Jan Gerston, Holley Toschlog, Hanna Prichard and Jules Henry who are always ready to help in all administrative matters.

Having a social life outside of research is very important and provides a much necessary break from research. I would like to extend a special thanks to all my roommates and friends starting with Shamik Basu, Akshay Parchure, Satyajit Bagul, Tejas Lendhe, Dr. Yogesh Babbar, Swanand Kadhe, Dr. Swapnil Ghodge, Sneha Chawla, Madhavi Sinha, Neelam Maheshwari, Samyukta Sethuraman, Aditya Desai, Sameer Jape, Kartikeyan Bisen and Nithin Thomas. Life in College Station would not be

the same without you. I will cherish the memories we shared together for the rest of my life or till the time my brain allows me to remember.

Thanks to all my friends in the cricket team especially “DADA” team members and the Aggie Cricket Club, for giving me a chance to play alongside you and making my weekends really memorable. I really cherish the time spent together on the cricket ground. Thanks to Swanand Kadhe for teaching me how to act again in College Station and the whole acting group for giving me an opportunity to be a part of the drama group. Thanks to all the members of the dancing group “Rangeela”, for giving me a chance to learn dancing and the motivation to perform on stage, especially Mahima Suresh and Samyukta Sethuraman for patiently teaching me dance steps and tolerating my struggle while learning the dance steps.

Thank you to all my friends, colleagues, the department faculty and staff for making my time at Texas A&M University a great experience. I also want to extend my gratitude to Air Force Office of Scientific Research (AFOSR) for financially supporting me throughout my doctoral studies.

Finally, I would like to thank the most important people in my life, my family, mother (Anjali Kothalkar), father (Dilip Kothalkar), uncle (Ramesh Kothalkar) and my lovely sister (Avanti Kothalkar) for their unconditional love, sacrifice, support, encouragement, and patience. This would not have been possible without your emotional and financial support. Words will never be able to express my gratitude towards you. You all deserve this doctoral degree.

NOMENCLATURE

DSC	Differential Scanning Calorimetry
EBSD	Electron Backscatter Diffraction
EDS	Energy Dispersive Spectroscopy
WDS	Wavelength Dispersive Spectroscopy
EPMA	Electron Probe Micro Analyzer
SEM	Scanning Electron Microscope
SMA	Shape Memory Alloy
SME	Shape Memory Effect
SPS	Spark Plasma Sintering
Wt.	Weight %
M_s	Martensite start
M_f	Martensite finish
A_s	Austenite start
A_f	Austenite finish
W^{NiTi}	Weight % of NiTi in the composite
$W^{Ti3SiC2}$	Weight % of Ti_3SiC_2 in the composite
$\Delta H^{comp.}$	Enthalpy of transformation of the composite
ΔH^{NiTi}	Enthalpy of transformation of pure equiatomic bulk NiTi
V_f^{NiTi}	Volume fraction of NiTi (vol. %) in the composite

ρ^{NiTi}	Theoretical density of NiTi
$\rho^{Ti3SiC2}$	Theoretical density of Ti_3SiC_2
$P_{overall}$	Volume fraction of overall porosity (vol. %) in the composite
$\Delta H^{A \rightarrow M}$	Enthalpy of transformation from Austenite to Martensite
J	Joule
g	Gram
°C	Degree Celsius
ΔT	Temperature Difference
AS	As Sintered
TMC	Thermo-mechanically Cycled
MMC	Metal Matrix Composites
CMC	Ceramic Matrix Composites
PMC	Polymer Matric Composites
CTE	Coefficient of Thermal Expansion
DMA	Dynamic Mechanical Analysis
nA	Nano Ampere
keV	Kilo Electron Volt
MPa	Mega Pascal
HTSMA	High Temperature Shape Memory Alloys

TABLE OF CONTENTS

Page

LIST OF FIGURES

LIST OF TABLES

Page

1. INTRODUCTION*

1.1 Motivation

With the rapid growth of the transportation industry (automotive and aerospace), high precision instruments, systems having tiny, highly sensitive electronic components, the demands for the control of noise and enhancing the stability of structures, and instruments are continually increasing. This necessitates the development of high damping materials, systems and/or structures which can suppress mechanical vibration, attenuate wave propagation, and stabilize structures and highly sensitive systems. Reducing noise and vibration of structures may also lead to the increase in their fatigue life leading to the improvement in their durability.

There are two ways of obtaining high-damping behavior, either by external or internal means. External means imply obtaining structural or system damping through air damping and absorbers, joint friction; and intrinsic means include material damping by using high damping materials [1]. The aim of this study is to employ the latter, material damping, through the development of high damping materials. This could contribute to the overall weight savings by completely removing or reducing the

*Part of this section is reprinted with permission from "Thermomechanical Response and Damping Behavior of Shape Memory Alloy–MAX Phase Composites" by Kothalkar et. al., Metallurgical and Materials Transactions A, 45, 1-13, [2014] by Springer and "Interfacial study of NiTi–Ti_3SiC_2 solid state diffusion bonded joints" by Kothalkar et. al., Materials Science and Engineering: A, 622, 168-177, [2015] by Elsevier

requirement for special active control devices, energy absorbers or dampers [1, 2]. Material damping capacity is defined as the amount of the energy dissipated during mechanical vibration under cyclic loading in the material [2].

In the last two decades, increasing attention has been placed on developing high damping materials for various applications such as reducing noise and vibration of structures, increasing the fatigue life, and improving the durability of cutting tools. Amongst the various classes of high damping materials, a large portion of research is dedicated towards the developing shape memory alloys for damping applications. The feasibility of using SMAs for seismic applications, i.e. protection of civil construction from earthquakes, has also been explored. The reason for extensive studies on SMAs is that the energy dissipation in SMAs is at least an order of magnitude higher than most structural metallic materials [3]. Another group of materials that also shows high mechanical damping capacity is nanolayered ternary ceramics, known as MAX phases. These materials are under extensive investigation for their unusual non-linear, hysteretic, elastic behavior, unlike most ceramics. They possess excellent combination of properties such as high stiffness, thermal and electrical conductivity, and fracture toughness while being readily machinable along with high damping capacity. For example, Ti_3SiC_2 belonging to the group of MAX phases, dissipates 25% of the mechanical energy while showing full recovery up to 1 GPa stress [4], under cyclic compression at room temperature. The mechanical damping observed in MAX phases is comparable to some woods and orders of magnitude higher than most structural ceramics with comparable stiffness [5].

Composite processing offers an opportunity for improving the damping behavior by modifying the microstructure and introducing various energy dissipation sources [2]. Hence, a metal/ceramic interpenetrating composite of two high damping materials, a NiTi SMA with a Ti_3SiC_2 MAX phase, is selected in this study. Combining two different classes of materials, such as a ceramic with a metal or alloy, naturally leads to the formation large number of interfaces between them. Large differences in thermal expansion coefficients (CTE) are bound to generate thermal mismatch strains possibly leading to the generation of crystallographic defects such as dislocations, mechanical twins around the interfacial region. These defects should play a vital role in contributing to the energy dissipation of the composite. The motivation behind choosing an SMA over other metals, apart from SMAs having high damping capacity, is to utilize the unique shape memory effect to introduce defects in both constituents, MAX phases and SMAs, and modify the microstructure of the composite. Thus by combining SMAs with the MAX phase, the aim here is to investigate whether large recoverable shape change in SMAs during thermo-mechanical cycling can generate residual stresses and defects that could further enhance damping capability of the novel SMA-MAX phase composites.

After selecting the different constituents of the composite, SMA and MAX phases in this case, it is the nature and properties of the interface that play a crucial role in determining the overall properties and performance of the composite. For example, load transfer across the interface determines the stiffening and strengthening of the composite, crack deflection/bridging affects the toughness and relaxation of stresses at the interface influences the ductility [6]. Thus, it is very important to carry out a

comprehensive microstructural characterization of the formation and evolution of the interfacial microstructures, interfacial fracture behavior and the correlations between them for complete understanding and development of composite materials. Diffusion bonding is selected in this study as the joining technique because it is capable of joining of wide variety of materials for industrial applications, is simple and does not require large capital investment and offers significant advantages over other conventional joining techniques such as welding [7].

One of the basic failure mechanisms affecting the fracture resistance of the composites is the debonding and fracture along the interfaces between the two constituent phases [8]. Thus, by measuring interfacial fracture toughness, correlations with the overall composite properties can be established. In composites, when the constituents have widely different elastic moduli, the modulus mismatch leads to shearing of the crack surfaces resulting in mixed-mode stress state [9]. Also, most real life applications which involve interface fracture problems experience mixed mode loading. Thus, for efficient and safe design of structures involving interfaces between dissimilar materials, it is important to characterize the interface fracture behavior under mixed mode loading configurations [10].

In summary, the aim of the proposed study is to process, characterize and study the mechanical damping of the SMA (NiTi) - MAX phase (Ti_3SiC_2) composites and improve their damping behavior through introduction of residual stresses and defects using shape memory effect of SMAs. As the interface plays an important role in determining the behavior of the composite, another goal here is to join bulk components

of NiTi and Ti_3SiC_2, microstructurally characterize the interface after different joining conditions and study interfacial fracture behavior under mixed mode loading conditions.

1.2 Shape Memory Alloys

1.2.1 Introduction

Shape Memory Alloys (SMA) belong to a unique class of metallic materials that undergo solid to solid martensitic phase transformation from a high temperature austenite phase to a low temperature martensite phase. Shape memory effect (SME) refers to the ability of SMAs to recover their original predeformed shape after deformation when heated above a particular temperature or on application of sufficient magnetic field. Shape recovery in SMAs is due to the thermoelastic martensitic phase transformation. Simply put, SMAs can find applications where they can be deformed using an external force and will come back to (or remember) their original shape when sufficient external stimuli such as thermal or magnetic is applied. Pseudoelasticity or Superelasticity (SE) is the ability of SMAs to recover large mechanical deformation immediately on unloading, under isothermal conditions, in high temperature austenite phase due to stress-induced martensitic transformation. Besides the unique shape memory effect (SME) and superelasticity, SMAs have the ability to absorb and dissipate large mechanical energy under applied mechanical cyclic loading. SMAs thus find applications in fields ranging from aerospace, automotive, biomedical to seismic applications for vibration damping. NiTi, the most characterized and widely used SMA, is a benchmark SMA that has been used for various applications in medical industry [11]

and different engineering fields [12] because of its excellent shape memory performance combined with good ductility, strength, corrosion resistance and damping capability.

1.2.2 Applications

SMAs find applications in various fields such as aerospace, automotive, appliance, automation and control, electronics, safety along with many others [13]. SMAs have been used in these industries since many decades now. In 1970s, SMAs were used in F-14 fighter jets for coupling of hydraulic lines [14]. An active aerodynamic device with SMA actuators, also known as variable geometry chevrons was used on commercial aircraft Boeing 777-300 ER [15-17], installed on a GE90-115B jet engine. The chevron reduced the noise during take-off and increased cruise efficiency during the remaining flight (Figure 1.1). NiTi thermovariable rate springs are used in automatic transmissions of Mercedes Benz for smooth gear shifting, domestic applications such as to control hot water flow, and the opening of door in the self-cleaning oven [18-21].

SMAs have been used for their good vibration damping capability in small spacecraft such as microsatellite for low shock release mechanisms [24-26]. SMAs also has applications in civil structures for seismic vibration control such as base isolation systems, cable stayed bridges due to their excellent damping capabilities [27]. European commission funded a project named MANSIDE (Memory Alloys for New Seismic Isolation Devices) which led to the implementation and testing of two full scale SMA isolation devices: for buildings and bridges, and energy dissipating braces for framed

structures [28, 29]. In august 2000, release tests were carried out on a building in southern Italy which demonstrated full scale applicability of SMA based isolated devices. The building weighed around 1500 tons, consisted of a 3 story R/C structure having dimension of 13.3m by 22.6m. Figure 1.2 (a) and (b) show the building equipped with the SMA based isolation device and the full scale isolation device itself respectively. The tests demonstrated excellent performance of the SMA based isolation devices in structural vibration isolation. For other applications and their in depth description, the reader is referred to the review articles [13, 30, 31].

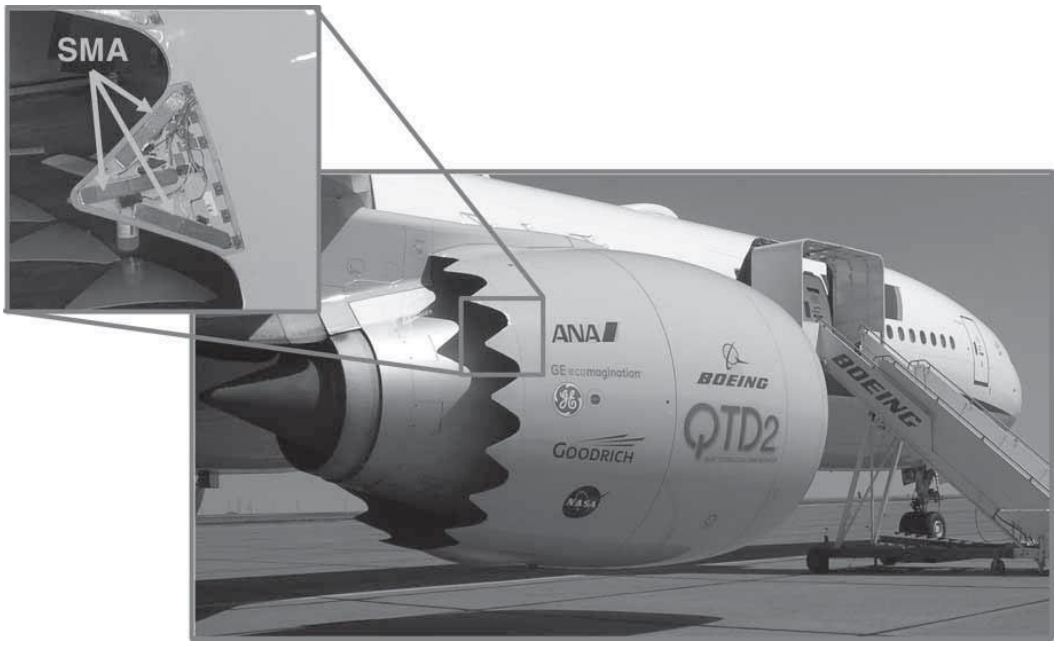

Figure 1.1 Variable geometry chevron flight tested by Boeing for noise reduction. Inset shows the position of SMA actuators which control the bending providing the structure with morphing capability [22, 23].

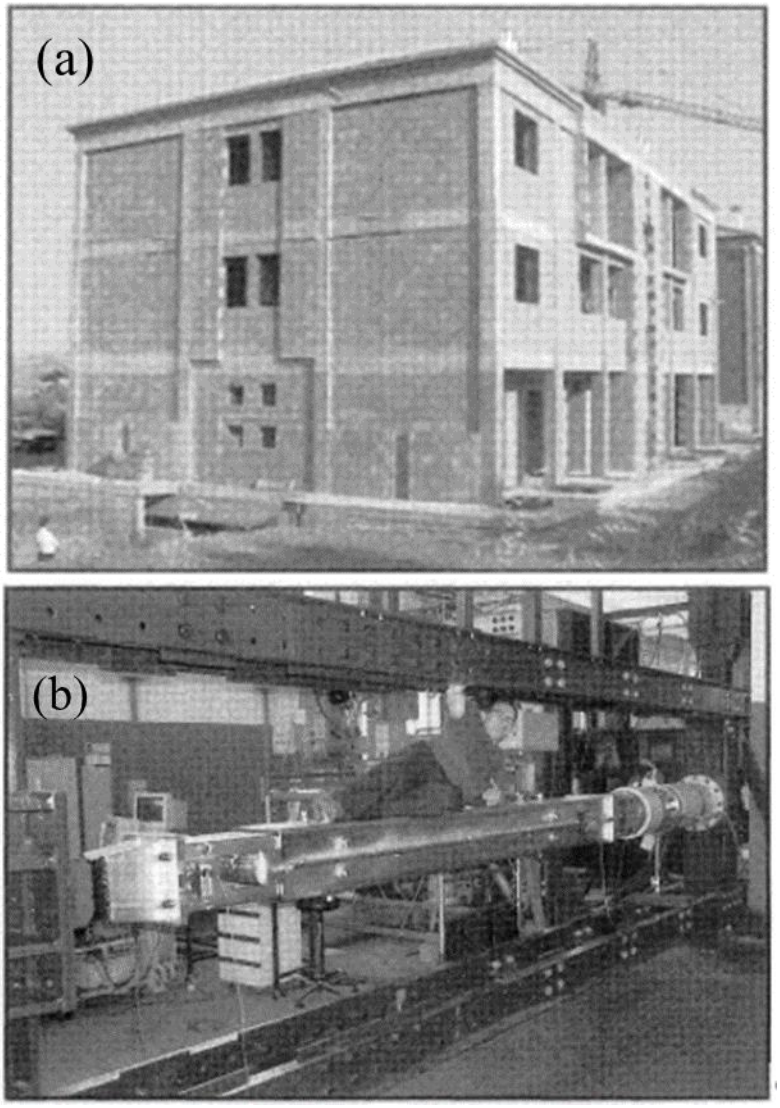

Figure 1.2 (a) SMA based isolation system employed in the building, (b) Full scale view of the isolation device [28].

1.2.3 Thermomechanical Behavior

Shape memory alloys show many unique characteristics, including the two widely observed and utilized phenomenon in applications, shape memory effect and Pesudoelasticity or Superelasticity. Here, our primary focus is on the shape memory

effect. SMAs can exist in two different phases, namely high temperature austenite and low temperature martensite, and three different crystal structures, namely austenite, twinned and detwinned martensite. When martensite is heated, it starts to transform into austenite at austenite start temperature A_s, and completely transforms into austenite at austenite finish temperature A_f. When the austenite is cooled, transformation to martensite starts at martensite start temperature M_s, and ends at martensite finish temperature M_f. When austenite is cooled under no stress, transformation occurs with no macroscopic shape change. The structure thus obtained is referred to as "self-accommodated" or twinned martensite. Change in the crystal structure from cubic (austenite) to monoclinic (martensite) in NiTi produces large local strain. This large local strain is accommodated by forming a twinned martensite structure in NiTi. Austenite to martensite transformation may occur in several 'ways', called martensite lattice correspondence variants [30]. Symmetry of austenite and martensite determines the number of possible variants; for example, 12 lattice correspondence variants can be formed when a cubic austenite transforms to a monoclinic martensite [32]. Under stress free conditions, all the different variants in the martensite are energetically equally favorable. However, when this self-accommodated martensite is deformed at constant temperature, some variants grow at the expense of others and form a single variant martensite. This process is called martensite reorientation or martensite detwinning and is always accompanied by macroscopic shape change. When this detwinned martensite is heated past A_f, it recovers its original shape prior to deformation as it completely transform into austenite. This shape recovery is referred to as one way shape memory

effect (OWSME) (Figure 1.3). Thus, remembering the shape it had prior to deformation in detwinned martensite. On cooling under no stress from austenite to temperatures lower than M_f again results in twinned martensite state.

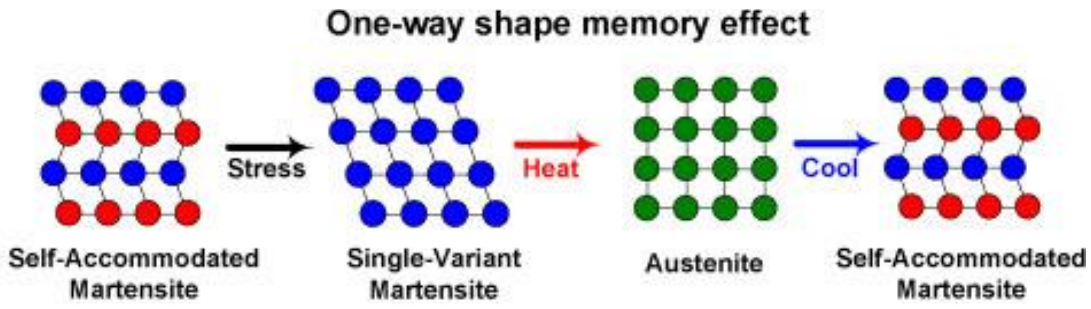

Figure 1.3 Demonstration of the one way shape memory effect (OWSME) [30]

In two way shape memory effect (TWSME), austenite directly transforms to detwinned martensite even when no external stress is applied and this transformation is accompanied by corresponding macroscopic shape change. On heating, it transforms back to austenite with macroscopic shape change. Thus, in TWSME, it remembers both shapes, in detwinned martensite and austenite whereas in OWSME, it remembers only one shape. TWSME is also referred to as reversible SME. TWSME is observed in materials that have experienced specific thermomechanical cycling path (also referred to as training) [33]. Training leads to permanent changes in the microstructure by introducing defects. These defects lead to directional residual internal stresses which favor the formation of one of the several possible variants leading to detwinned

martensite. Plastic deformation of martensite leading to directional arrangement of dislocations or retained martensite in the structure due to prior thermo-mechanical treatment is one of the several mechanisms that can cause generation of directional internal stresses in SMA's [33-36]. In this study, both the OWSME and TWSME of SMA-MAX phase composites are extensively characterized; their evolution with applied stress and the mechanisms contributing to the generation of residual internal stress are investigated.

1.2.4 Energy Dissipation/Damping Behavior

Besides the unique shape memory effect (SME) and Superelasticity, SMAs also possess high mechanical damping capacity in both, austenite and martensite phase. The energy dissipation capacity of materials is related to the different microstructural mechanisms leading to the internal dissipation of mechanical energy. The mechanism of reversible stress induced martensitic transformation in austenite and hysteretic movement of twins, twin boundaries and martensite variant interfaces in martensite contributes to their high damping capacity [3, 37-47]. This high damping capability of the SMAs can be utilized to suppress undesirable mechanical vibration and wave propagation. Collective results from fundamental, small scale to elaborate, large scale studies conclude that the SMAs can be effectively used for vibration control of structures through vibration isolation and energy absorption mechanisms [31]. The reason for extensive studies on SMAs is that the energy dissipation is at least an order of magnitude higher in SMAs than most structural metallic materials [3]. Thus, the idea behind

combining a SMA with a MAX phase (discussed in detail section 1.3) is to utilize the high damping capacity of both materials to obtain improvement in the overall damping capability.

1.3 MAX Phases

1.3.1 Introduction

More than 60 ternary carbides and nitrides with the general formula $M_{n+1}AX_n$ (MAX phases), where n = 1, 2, or 3, M is an early transition metal, A is an A-group element (from columns 13–16 in the periodic table), and X is C and/or N, have unusual and unique combination of metallic and ceramic properties [48, 49] (Figure 1.4). Like metals, they have high thermal and electrical conductivity [51], good thermal shock resistance [52] and damage tolerance [53], and are most readily machinable. Like ceramics, they have low density, high Young's modulus [54, 55], good high temperature strength and creep resistance [56-58] along with good corrosion resistance [59]. The unit cells of the MAX phases are characterized by near close-packed M layers interleaved with layers of a pure A-group element, with the X atoms filling the octahedral sites between the former [60].

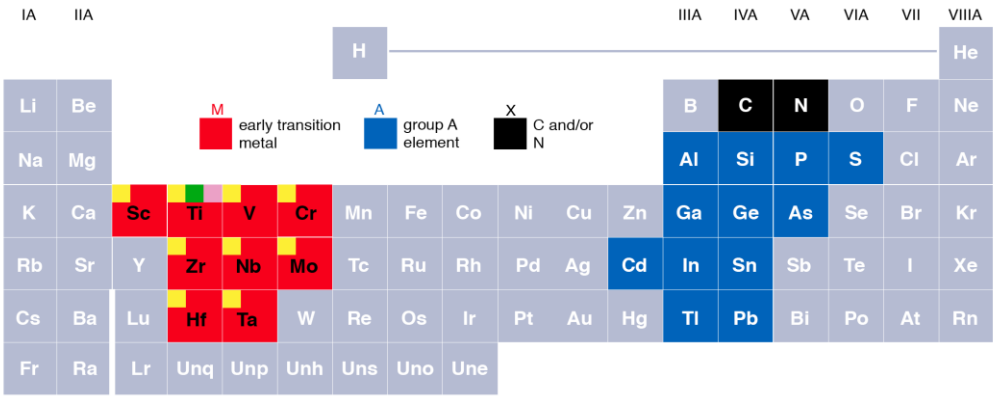

Figure 1.4 Possible combination of elements that form the MAX phases where M is an early transition metal [red], A is an A group element [blue] and X is C or N [black], reprinted from [50]

Among all the MAX phases known till date, Ti_3SiC_2 is the most characterized and well known one with low density (4.52 g/cm^3 [48]) and high elastic modulus (343 GPa [5]). Like other MAX phases, Ti_3SiC_2 shows spontaneous fully reversible, strain rate independent hysteretic stress-strain loops when cyclically loaded in compression [4] or tension [58]. Thus, a significant portion of the mechanical energy - about 25% at 1 GPa in the case of Ti_3SiC_2 - can be dissipated during each cycle [4]. At this time, Incipient Kink Bands (IKBs) that form during loading and annihilate during unloading are believed to be one of the factors contributing to the unusual hysteretic (or pseudoelastic) behavior [4]. IKBs are fully reversible dislocation loops observed in plastically anisotropic solids which nucleate on easy slip planes [61]. Mechanisms of energy dissipation are described in detail in section 1.3.4. Above brittle-to-plastic transition temperature, i.e. above 1000 - 1100°C, stress-strain response of Ti_3SiC_2 becomes a strong function of temperature and deformation rate, and it can be plastically deformed to strains exceeding 25% even in tension [58, 62, 63]. Along with high

damping capacity, Ti_3SiC_2 possesses high temperature strength; good high temperature oxidation resistance and good machinability making it a potential candidate for high temperature structural applications.

1.3.2 Applications

MAX phases possess a remarkable set of properties. Currently, they are being developed for applications such as resistive heating elements and electrodes, gas burner nozzles, foil bearings, rotating electrical contacts, drilling tools and heat exchangers [64] (Figure 1.5). For example, by utilizing excellent thermal and electrical properties of MAX phases, company named 3-ONE-2, LLC have developed heating elements made of Ti_2AlC (211-Maxthal ®) [67]. As gas burner nozzles, they have been shown to perform better than steel under sulphur containing natural gas corrosive atmospheres, owing to their high corrosion and oxidation resistance. Drilling tools made up of diamonds in MAX 312 have been developed by 3-ONE-2 and Hilti [64]. These materials were reported to be much better than the current diamond/Co for drilling of concrete. Ti_3SiC_2-hydroxypatite composites have been developed and displayed favorable properties for bio-applications [68], owing to the bioinertness of Ti_3SiC_2 [69]. Honeywell is developing MAX phase based materials such as Ta_2AlC/Ag, which have low friction and wear properties for foil bearing applications [64].

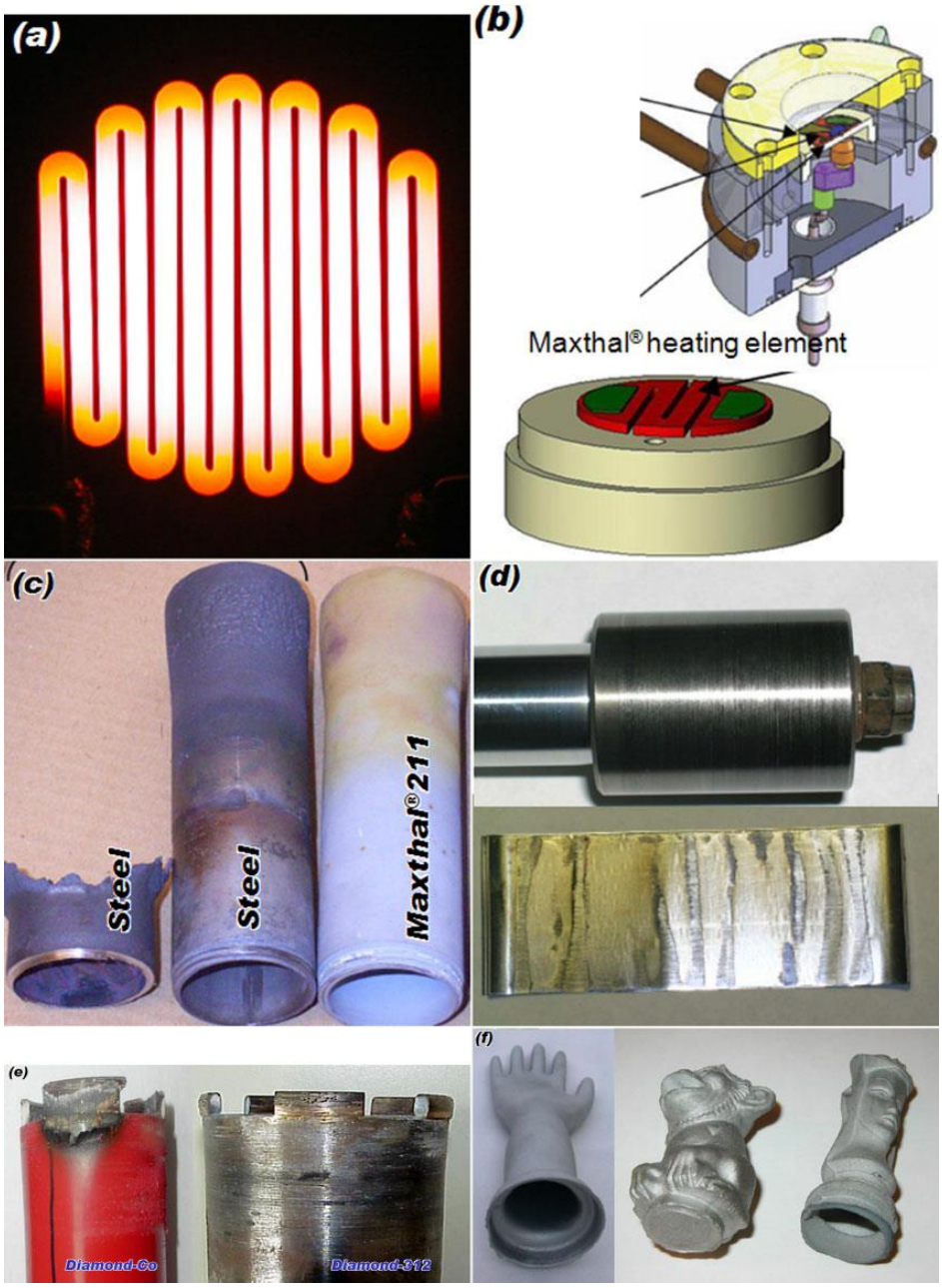

Figure 1.5 Few current and potential applications of MAX phases (a) Ti_2AlC Heating element at 1723 K (courtesy 3-ONE-2, LLC), (b) reactor cell with Maxthal 211 heating elements [65], (c) Comparison of Maxthal gas burner nozzles and 353MA steels after one year at 1773 K (courtesy 3-ONE-2, LLC and Kanthal), (d) Condition after 10,000 cycles in a rig: Ta_2AlC/Ag shaft and superalloy foil [66], (e) Diamond-Co and Diamond-Ti_3SiC_2 concrete dry drills (courtesy 3-ONE-2, LLC and Hilti), (f) Three-dimensional shapes of MAX phases obtained after slip casting and sintering (courtesy 3-ONE-2, LLC)

As MAX phase possess high fracture toughness and energy dissipation capabilities apart from high temperature strength and oxidation and corrosion resistance, they are an excellent candidate for applications in aerospace industry. Owing to the low density of these materials, these materials have also been considered as light weight armor materials. Investigations have demonstrated the potential use Ti_3SiC_2 as parts of add-on ceramic armor [70, 71]. Apart from these applications being developed, severe potential applications include directly heated catalyst support and exhaust gas filters for automobiles, oxidation resistant films or coatings, cladding materials for nuclear applications [64, 72].

1.3.3 Fracture Toughness

Nanolayered ternary ceramics, also known as MAX phases, have considerably higher fracture toughness (K_{1c}: 5.5 – 16 MPa-$m^{1/2}$) than monolithic ceramics and most ceramic matrix composites [9]. MAX phases in general and especially Ti_3SiC_2 are known for their high fracture toughness and R-curve behavior [60, 73]. MAX phases are believed to possess one of the highest values of fracture toughness ever reported for a monolithic, single phase, non-transforming ceramic [60]. Table 1.1 lists room temperature fracture toughness (K_{1c}) values of select few MAX phases and select few ceramics.

Table 1.1 Room temperature fracture toughness (K_{1c}) values of select few MAX phases [60] and select few ceramics [9].

	Material	**K_{1c} MPa $m^{1/2}$ (room temperature)**
MAX phases	Ti_3SiC_2	7-16
	Ti_3AlC_2	6.9-9.5
	Ti_2AlC	6.5
	Ta_2AlC	7.7
	Nb_4AlC_3	7.1
Ceramics	Sodalime glass	0.5-1
	Magnesium Oxide	3
	Alumina	1-3
	Silicon Carbide	2-4
	Silicon Nitride	3-5

MAX phases have much higher fracture toughness than most regular ceramic materials. These materials display higher degree of grain bridging, sliding and frictional pullout mechanisms, similar to processes observed in Al_2O_3 [74], Si_3N_4 [75], and SiC [76]. Apart from these mechanisms, Ti_3SiC_2 also shows crack bridging through heavily deformed lamellae, along with significant amount of delamination and bending [73]. These mechanisms contribute to the high fracture toughness values of Ti_3SiC_2. Deformation and distortion of laminae, which are formed due to delamination along the weaker basal planes, contributes to the increased toughening observed in these materials [77]. The ability of MAX phases to contain damage through the mechanisms of

delamination and kinking of individual grains makes them an exceptionally good damage tolerant material [60]. Fracture toughness of MAX phases may be further improved by addition of ductile metallic materials such as SMAs. Thus, this study on the fabrication and characterization of the SMA-MAX phase composites will serve as a precursor to future fracture toughness studies on the SMA-MAX phase composites.

1.3.4 Mechanical Hysteresis/ Energy Dissipation

MAX phases are known for their unusual non-linear, hysteretic, elastic behavior, unlike most ceramics. On cyclic compression under very high loads, they show full recovery, dissipating large amounts of mechanical energy in the process. For example, under cyclic compression at room temperature, Ti_3SiC_2 dissipates 25 % of the mechanical energy while showing full recovery up to 1 GPa [4]. Inset in Figure 1.6 shows that full recovery is observed in fine grain Ti_3SiC_2 under uniaxial compression at room temperature. Figure 1.6 shows the comparison of stress–strain curves at room temperature for different materials: fine and coarse-grained Ti_3SiC_2, Al_2O_3 and Al. As expected for Al_2O_3 and Al under linear elastic region, no hysteretic dissipative behavior is observed. But for fine and coarse-grained Ti_3SiC_2 microstructures, reversible, hysteretic behavior is observed wherein the area under the loop represents the amount of energy dissipated in that loading-unloading cycle. Mechanical damping observed in MAX phases is comparable to some woods and orders of magnitude higher than most structural ceramics with comparable stiffness [5].

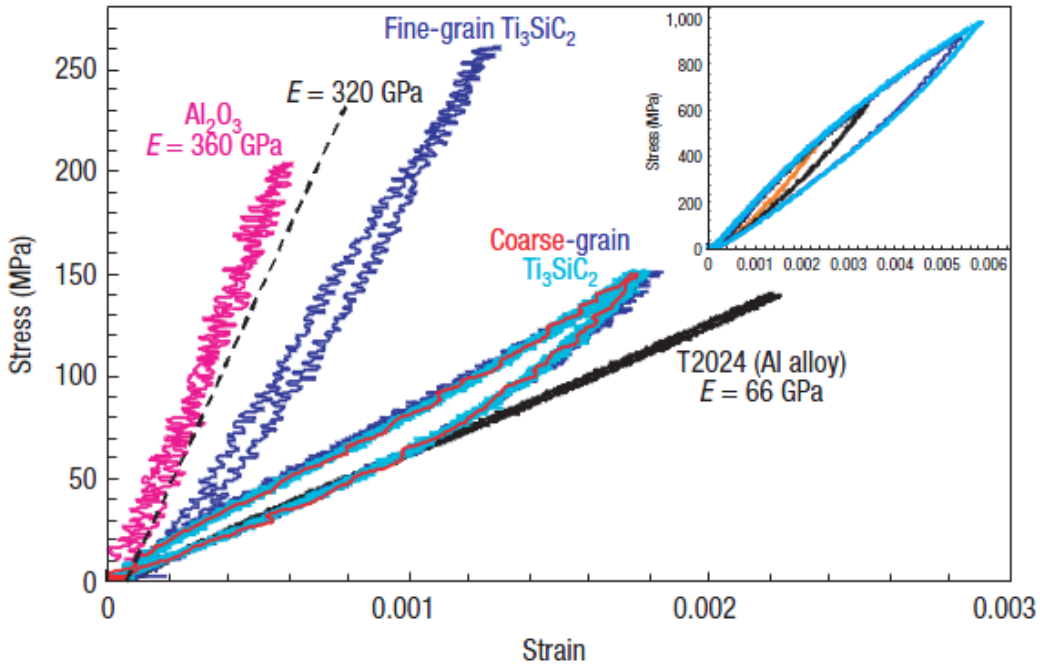

Figure 1.6 Comparison of stress–strain curves at room temperature for different materials: fine and coarse-grained Ti_3SiC_2, Al_2O_3 and Al [4]. The dashed line represents the response expected from Ti_3SiC_2 without non-linear behavior. E is Young's modulus. Inset and figure axes are identical. Reprinted with permission from NPG

Various models including the Kinking Nonlinear Elastic (KNE) model [78-81], Microcracking model (MC) [82] and Reversible Flow (RF) model [83] have been proposed to explain the non-linear hysteretic behavior of MAX phases and account for the energy dissipation during each of the loading-unloading cycles. As per the KNE model, formation, growth and annihilation of incipient kink bands (IKB), reversibly under stress is responsible for the observed energy dissipation in the MAX phases. According the MC model, friction caused by the microcracks and crack surfaces formed because of delamination during loading lead to the hysteretic behavior in the MAX

phases. RF model suggests that plastic anisotropy or Bauschinger-like effect is responsible for the reversible macroscopic deformation in the MAX phases. However, no single model can explain all the phenomena observed in the deformation of MAX phases. In a recently published article on deformation of Ti_2AlC, the authors show that the above mentioned models are valid only in certain stress ranges and all of them are required to completely characterize the hysteretic behavior of MAX phases in the complete stress range [84]. That study classifies the uniaxial deformation of fine and coarse grain Ti_2AlC under compression in four different stress regions (Figure 1.7): region I where the behavior is completely linear elastic; region II where deformation and energy dissipation can be explained by the RF model; region III where reversible movement or bowing of dislocation walls, unlike proposed by the KNE model, is responsible for the observed cyclic hardening and large energy dissipation; and region IV where MC model along with the RF and reversible movement of dislocation walls simultaneously contribute to the observed behavior. As the energy dissipation in pure MAX phases depend on stress or strain experienced by them, energy dissipation capacity of the SMA-MAX phase composites is bound to be affected by the load distribution among these phases.

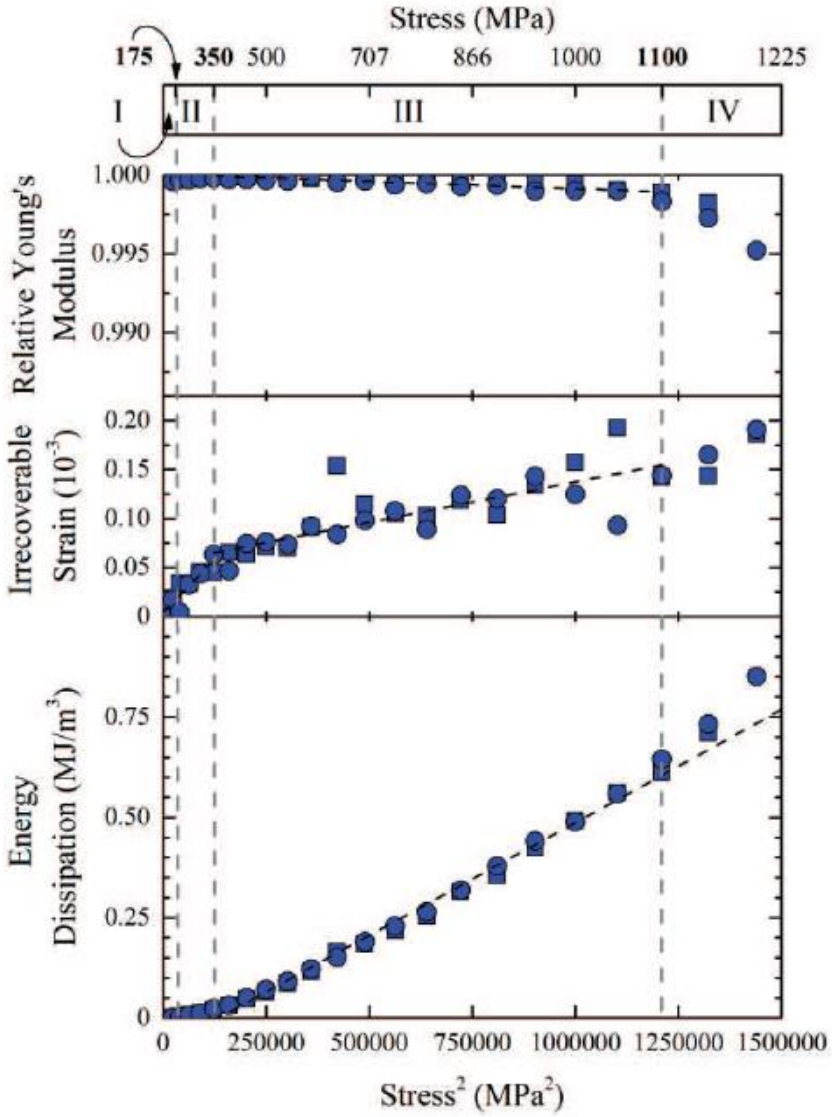

Figure 1.7 Bottom, middle and top plots show the W_d, irrecoverable strain from first load-unload cycle and relative young's modulus respectively, as a function maximum applied stress squared [84]. Square and circular represent two different samples. Average grain diameter and thickness were 6 ±3 μm and 5 ±2 μm respectively

Thus, the aim in this study is to process SMA-MAX composites having strong interface for better load transfer and maximize the individual contribution to the overall

composite damping capacity. This necessitates the extensive interfacial characterization between these two components under various processing conditions along with its fracture strength.

1.4 Joining and Interface Fracture

1.4.1 Joining

Recently, the ability to reliably manufacture large components of engineering ceramics has improved along with better understanding of its processing techniques. Still, most engineering applications require them to be joined with other materials, mostly metals. Metal-ceramic joining is not easy, mainly due to two reasons, nature of atomic bonding and large differences in coefficients of thermal expansions (CTE) [85]. Most ceramics have much lower coefficient of thermal expansions than metals. Thus, when they are cooled from joining or bonding temperatures, metals contract more than ceramics leaving the latter under tensile state of stress, making the joint or the ceramic prone to failure.

MAX phases, as described in section 1.3.1, possess a combination of metallic and ceramic properties, as they are stiff but readily machinable ceramics, with excellent thermal and electrical conductivity. This combination of properties is attributed to the nature of atomic bonding and layered crystal structure [60]. MAX phases possess a combination of metallic, ionic and covalent bonding [86], which is responsible for metallic as well as ceramic like behavior. Considering these two facts, that MAX phases

have partial metallic bond character and higher CTE than most ceramics, it makes them suitable for joining with metals.

Several studies have been conducted to investigate the feasibility of joining MAX phases with other metals and study their reactions and stability at elevated temperatures [87-95]. Joining of Ti-6Al-4V with Ti_3SiC_2 in the temperature range of 1200-1400°C showed that below 1350°C, the mechanism for bonding is solid state diffusion whereas above it is liquid state diffusion [90]. Diffusion bonding of Ni with Ti_3SiC_2 in the temperature range of 800-1100°C suggested that the diffusion of Ni into Ti_3SiC_2 is the key step in the bonding process [91]. Study on the stability of Ti_3AlC_2 in presence of Cu in the temperature range of 800-1050°C found that at 800-950°C, partial loss of Al occurs from Ti_3AlC_2 into Cu leading to the formation of Cu (Al) solid solution whereas above 950°C, Ti_3AlC_2 decomposed and transformed into TiC_x [88]. Reactions between Ti and Ti_3SiC_2 were investigated in the temperature range of 1000-1300°C [95]. They found out that Ti_3SiC_2 decomposes in two different ways: by de-intercalation of Si and formation of TiC_x by remaining Ti and C; and secondly, by separation of C from Ti_3SiC_2 and further reaction of C with Ti. The common theme in these studies is the successful joining of the MAX phases with various metals without an interlayer and the loss of "A" element from the MAX phases contributing to the formation of new reactive phases. The leaching out of the "A" element from the MAX phase is expected as it is the most weakly bonded element in MAX phases [86]. As the SMA-MAX composites are being studied in this research, it makes sense to systematically study the joining of SMA-MAX phase without an interlayer between them to characterize the possible

reaction phases between SMAs and MAX phases. Thus, this study will also serve as a basis for understanding the reactivity of MAX phases with NiTi at elevated temperatures and designing and controlling the microstructures of SMA-MAX phase joints and composites.

1.4.2 Mixed Mode Interface Fracture

Fracture of a metal/ceramic interface plays an important role in many areas of technological relevance, including decohesion of thin films/substrate systems used in microelectronic devices [96, 97], thermal barrier coatings for turbine blades [98], multilayer capacitors, layered structural composites, and adhesive joints [99]. Interfaces are a critical part of multiphase composites, and their properties play a crucial role in determining the overall properties and performance of the composite. For example, load transfer across the interface determines the stiffening and strengthening of the composite, crack deflection/bridging along the interface affects the toughness of the composites [6]. Fracture in a metal or ceramic matrix composite will occur either along the interface or in one of the individual constituent phases. As a precursor for studying the fracture of the composites, it is important to understand and quantitatively characterize fracture behavior of the interface between the constituents.

The fracture toughness is a critical parameter in determining the applicability of a composite to various engineering fields, especially for structural applications. The critical strain energy release rate (G_c) (J/m^2) is a measure of the resistance to crack propagation. The parameter G_c has been studied extensively for different composite

systems [100-110]. Crack propagation can occur in one of the three fracture modes: mode I, II, and III (also referred to as the opening, shearing and tearing mode respectively). Mixed mode refers to a combination of these modes. Most real life applications involving interfacial fracture experience mixed mode loading. Thus, for efficient and safe design of structures involving interfaces between dissimilar materials, it is important to characterize the interface fracture behavior under mixed mode loading configurations [10].

Several tests have been utilized to characterize the interfacial fracture toughness under mixed mode loading configurations [111-117], but the most relevant here is the four point bend delamination test [113]. One of the advantages of using four-point bend delamination test is that the moment between the inner loading points is constant [112]. Thus, the strain energy release rate becomes independent of crack length between the inner loading points. The assumption being that the crack grows along the interface and the critical strain energy release rate (G_c) of the interface does not vary significantly. This makes the experiment easier to conduct as it removes the necessity to monitor the crack length during testing

The analytical solution for calculating the critical strain energy release rate (G_c) for the four point bend delamination test as a function of the critical load, P_c, is given by equations 1-5 [113] below

$$G_c = \frac{M^2\left(1-\nu_2^2\right)}{2E_2}\left(\frac{1}{I_2}-\frac{\lambda}{I_c}\right) \quad (1)$$

$$\lambda = \frac{E_2(1-\nu_1^2)}{E_1(1-\nu_2^2)} \quad (2)$$

$$I_c = \frac{h_1^3}{12} + \lambda\frac{h_2^3}{12} + \lambda h_1 h_2 \frac{(h_1+h_2)^2}{4(h_1+\lambda h_2)} \quad (3)$$

$$I_2 = \frac{h_2^3}{12} \quad (4)$$

$$M = \frac{Pl}{2b} \quad (5)$$

where a subscript of 1 and 2 corresponds to the top and bottom layer respectively, λ is a function of elastic properties of each layer, I_2 is the second moment of area of the bottom layer, and I_c is the second moment of area of the composite. Other geometric parameters are shown in Figure 1. Using the Euler-Bernoulli beam theory and assuming plane strain conditions, the strain energy release rate can be obtained analytically by subtracting the strain energy stored in the cracked beam from that stored in the uncracked beam [113]. For the derivation of the analytical solution of the strain energy release rate and the assumptions involved, the reader is referred to the following article [113]. In this study the aim is to characterize the interfacial fracture toughness of NiTi-Ti_3SiC_2 bilayers under mixed mode delamination beam test utilizing the equations 1-5 described above. Thus, this study will also be useful in understanding the fracture behavior of the SMA-MAX phase composite, as interfaces may play a vital role in determining composite's fracture behavior.

1.5 Ceramic and Metal Matrix Composites

Composites are known to mankind since many centuries in the form of naturally occurring wood, seashells or manmade materials such as steel. The recognition of this concept of combining two distinct form of materials to obtain better or improved properties as compared to individual constituent materials is pretty recent. Since then, the field of composites has grown rapidly with applications found in aerospace, transportation industry including automotive and railways, electronic packaging, recreational products and sporting equipment among many others. Composites are often utilized to achieve combination of properties that is not easily achievable in conventional monolithic materials. For example, metallic materials are ductile but have lower strength. Ceramic materials have high strength but are brittle. By combining metals with ceramics, a combination of moderate strength and ductility can be achieved.

1.5.1 SMA-Ceramic Composites

SMAs are multifunctional materials with ample current and potential applications. The ever increasing need for materials that can retain their multifunctionality while providing conventional materials performance has led to the combination of the SMAs in other materials. By combining SMAs with other functional or structural materials, either as matrix or reinforcements, optimal combination of properties relevant to specific applications can be achieved. By incorporating SMAs in other materials, the concept of tuning the properties has also been suggested, which has tremendous potential to cater to the needs of advanced engineering applications [118].

SMA being a smart material, a lot of research effort has been dedicated in the last two decades to develop smart/intelligent materials and structures with multifunctional and adaptive properties [118]. SMAs have been combined with PMCs [119-123], MMCs [124-129] and CMCs [130-132] either in embedded form or bonded to these materials for various applications ranging from actuators, sound and vibration control, for impact damage and creep resistance in structures. Several studies have been conducted where ceramic reinforcement has been added to study shape memory behavior in the presence of ceramic particles [133-141]. On the other hand, NiTi has also been added as a toughening agent in ceramics to improve the toughness of the ceramics [130-132, 142].

The advantage of SMAs over conventional metallic materials is the presence of SME. Due to the macroscopic shape change during SME, SMAs can introduce internal stresses in the SMA based composites which can lead to improvement in the desired properties. For example, utilization of the shape memory effect of NiTi particles dispersed inside the aluminum metal matrix composites (MMCs) to strengthen them has also been proposed [143]. The strengthening mechanism suggested is as follows: already prestrained SMA particles incorporated in the Al matrix upon heating will undergo reverse transformation and recover original shape, thus introducing residual compressive stresses in the matrix. Hence, one of the reasons for studying a composite of two high damping materials, a NiTi SMA with a Ti_3SiC_2 MAX phase, is to investigate whether the large recoverable shape change in NiTi during thermo-mechanical cycling can generate residual stresses that could further enhance its overall damping capability.

1.5.2 MAX Phase – Metal Composites

Recently, several studies have been reported on the MAX phase-metal composites in an attempt to tailor/optimize properties of MAX phases for different applications by adding metallic phases. The first metal - MAX phase composite reported was of Cu/Ti_3SiC_2 system demonstrating superior mechanical properties and higher electrical conductivity as compared to Cu/graphite composites as electro-friction materials [144]. Since then, mechanical strength of Cu has been enhanced by reinforcing it with different MAX phases such as Ti_3SiC_2 [145-146], Ti_3AlC_2 [147-148] and Ti_2SnC [149] without significantly decreasing its electrical conductivity. The tribological performances of Ag/Ta_2AlC and Ag/Cr_2AlC composites, as new solid lubricant materials against Ni-based superalloys and alumina, have also been investigated in the temperature range of ambient to 550°C [66]. There have been few studies on processing, compressive properties and tribological performances of Al/Ti_3SiC_2 composites [150]. In another study, Ni/Ti_3SiC_2 and Co/Ti_3SiC_2 composites were fabricated but poor wettability of Ni or Co with Ti_3SiC_2 resulted in inhomogeneous microstructures [151].

Most recently, two materials with high mechanical damping were combined in Mg/Ti_2AlC [152] and Mg/Ti_3SiC_2 [153] composites in order to produce light-weight but stiff materials with superior mechanical damping capabilities. These composites displayed fully reversible hysteretic stress-strain loops under uniaxial cyclic compression at room temperature, that dissipate more elastic mechanical energy in each cycle than either pure Mg or MAX phase [152-153]. As SMAs also possess high damping capacity similar to Mg, the aim here is to combine SMAs with the MAX phase to obtain high

damping and investigate whether SME of SMAs can be utilized to generate residual internal stresses and defects which can further increase their overall damping capacity.

2. RESEARCH OBJECTIVES

The aim of the proposed study is to process, characterize and study the mechanical and thermomechanical behavior of the SMA (NiTi) - MAX phase composites. As the interface plays an important role in determining the behavior of the composite, the aim here is also to join bulk components of NiTi and MAX phase, microstructurally characterize the interface under different processing conditions and obtain the fracture toughness of the interface. Thus, the proposed study can be broadly classified into two parts: study of composites and interfaces as summarized in Figure 2.1

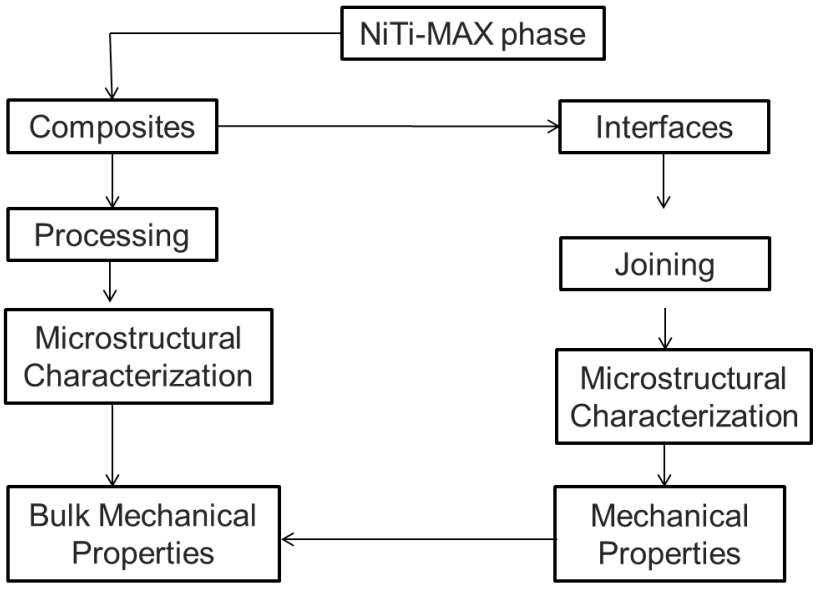

Figure 2.1 Schematic showing the overview of the proposed study

The objectives of this study are

1) To process, for the first time, the novel SMA (NiTi) – MAX phase composites using SPS;
2) To microstructurally characterize the composites using scanning electron microscopy (SEM);
3) To thermo-mechanically characterize the shape memory behavior of the composite, by doing differential scanning calorimetry (DSC), isobaric heating-cooling experiments under uniaxial compressive stresses;
4) To study the damping behavior of as-sintered composites under uniaxial quasistatic compressive cyclic loadings at room temperature, as both MAX phases and SMAs possess good damping capability;
5) To investigate the introduction of residual stresses by thermo-mechanical cycling and their effect on damping behavior of the composites;
6) To join bulk components of SMAs and MAX phases using pressureless and pressure assisted diffusion bonding in a tube furnace and SPS;
7) To investigate the formation and evolution of microstructures in the diffusion bonded interface at elevated temperatures using SEM and also the new phases formed in the interface using SEM, energy and wave dispersive spectroscopy (EDS/WDS) and electron back scatter diffraction (EBSD).
8) To propose a reaction mechanism for the newly formed phases and study the growth kinetics of the interfaces;

9) To evaluate the mechanical properties such as hardness and elastic moduli using nanoindentation and fracture toughness of the interface using mixed mode four point bend delamination test;

   Thus, this study will serve as a basis for understanding the reactivity of MAX phases with NiTi at elevated temperatures and designing and controlling the microstructures of NiTi-MAX phase joints and composites.

3. EXPERIMENTAL METHODS*

3.1 Spark Plasma Sintering (SPS)

3.1.1 NiTi-MAX Phase Composites Processing

To keep the reaction layer to minimum and retain original individual components in the composite, a fast processing technique called spark plasma sintering (SPS), is used in the current study. SPS employs uniaxial loading while applying a pulsed DC voltage which results in rapid heating rates enabling fast densification of materials at lower temperatures compared to conventional sintering techniques. The relatively low temperatures combined with small processing times ensure tight control over interfaces, grain growth, and microstructure in the materials.

Ti_3SiC_2 powders (Sandvik, Sweden) with the particle sizes of 45~90 μm and equiatomic NiTi powders (gas atomized from an alloy ingot with the nominal composition of 50 at. % Ni) with the particle sizes of 88~105 μm are used to process all the composite samples in this study. The Ti_3SiC_2 powders are mixed with 50 vol. % of equiatomic NiTi powders by ball milling and placed in a graphite die in the SPS machine (Thermal Technology LLC, Model # SPS 25-10). Inside the SPS chamber, vacuum is held at 10^{-6} torr for 10 minutes and then argon is backfilled to a pressure of 2 torr. Then

---

*Part of this section is reprinted with permission from "Thermomechanical Response and Damping Behavior of Shape Memory Alloy–MAX Phase Composites" by Kothalkar et. al., Metallurgical and Materials Transactions A, 45, 1-13, [2014] by Springer and "Interfacial study of NiTi–Ti_3SiC_2 solid state diffusion bonded joints" by Kothalkar et. al., Materials Science and Engineering: A, 622, 168-177, [2015] by Elsevier

the samples are heated to 960 ~ 1000°C at 200°C/min and held at the target temperature for 3 ~ 20 minutes. Uniaxial pressure of 100 MPa is applied before starting the heating cycle and maintained till the sample cooled to ambient temperature.

Bulk equiatomic NiTi (acquired from SAES Getters in cold drawn condition and solution heat treated at 800°C for 1 hour in vacuum), and bulk Ti_3SiC_2, reaction sintered at 1400°C for 8 hours using hot isostatic pressing (HIPing), were also used in this study to compare their properties with that of the composites. The average grain size of the reaction sintered bulk Ti_3SiC_2 was 10 μm and that of solution heat treated NiTi was around 50 μm.

Table 3.1 lists all the processing conditions and the porosity contents for the composites synthesized using SPS. The density and the overall porosity of the sintered samples were determined by alcohol immersion method based on the Archimedes' principle, as specified in ASTM C20-00 [154]. The theoretical density of 5.48 g/cm^3 for fully dense 50 vol. % NiTi/Ti_3SiC_2 composite was calculated by taking the weighted average of 50 volume % NiTi and 50 volume % Ti_3SiC_2 with densities of 6.45 g/cm^3 [155] and 4.52 g/cm^3 [48], respectively. Calculation of theoretical density assumes that no new reaction phases are formed after sintering.

According to the NiTi binary phase diagram, liquid phase starts to form at around 980°C in the Ti-rich region of the phase diagram [156]. To avoid the formation the liquid phase, 960°C and 8 minutes were initially selected as the starting processing condition. The SPS # 1 composite had a porosity of 16.7 %. To decrease the porosity content, sintering time was increased to 20 minutes keeping everything else the same.

No significant change in porosity was observed. Temperature was then increased to 980 and 1000°C but time was reduced to 10 and 3 minutes respectively, in order to keep the reaction between the two phases as low as possible. The porosity values obtained for all the processing conditions listed in Table 3.1 is within the error limits of each other.

Table 3.1 Processing conditions of 50 vol. % NiTi/Ti_3SiC_2 composites and their porosity values.

Sample	Sintering temperature (^oC)	Time (mins)	Pressure (MPa)	Total Porosity (Vol. %)
SPS # 1	**960**	**8**	**100**	**16.7 ± 1.1**
SPS # 2	**960**	**20**	**100**	**16.5 ± 0.8**
SPS # 3	**980**	**10**	**100**	**16.4 ± 1.1**
SPS # 4	**1000**	**3**	**100**	**17.2 ± 0.9**

3.1.2 NiTi-Ti_3SiC_2 Joining

Bulk equiatomic NiTi having transformation temperatures of 40, 67, 75 and 107°C for martensite finish (M_f), martensite start (M_s), austenite start (A_s), and austenite finish (A_f) respectively, was acquired from ATI Wah Chang (Rotary forged at 800°C followed by air cooling). Pre-alloyed powders (unsieved) obtained from Sandvik Sweden was used to process fully dense Ti_3SiC_2 in the SPS under following conditions:

1325°C, 100 MPa, 15 minutes, heating/cooling rate of 50°C/min, loading rate of 50 MPa/min at 1000°C (inside the SPS chamber, vacuum was held at 10^{-6} torr for 10 minutes and then argon was backfilled to a pressure of 2 torr). 40 mm diameter discs of NiTi and Ti_3SiC_2 were cut using wire electric discharge machining (EDM). Each Ti_3SiC_2 disc was further cut into two symmetric halves by EDM. All samples were polished using standard metallography techniques followed by ultrasonic cleaning in ethanol prior to joining. Spark Plasma Sintering (SPS) machine (Thermal Technology LLC, Model # SPS 25-10) was used to join the discs under following conditions: 1000°C, 40 MPa, 30 minutes, heating/cooling rate of 50°C/min under 5 MPa pre-stress, loading rate of 35 MPa/min at 1000°C (inside the SPS chamber, vacuum was held at 10^{-6} torr for 10 minutes and then argon was backfilled to a pressure of 2 torr).

3.2 Horizontal Tube Furnace

Bulk equiatomic NiTi having transformation temperatures of 45, 61, 76 and 94°C for martensite finish (M_f), martensite start (M_s), austenite start (A_s), and austenite finish (A_f) respectively, was acquired from SAES Getters in cold drawn condition. Bulk Ti_3SiC_2 samples were reaction sintered from Ti, SiC and C powder mixtures at 1400°C, for 8 hours using hot isostatic pressing. The NiTi and Ti_3SiC_2 samples were cut using wire electrical discharge machining (EDM) to the sizes of 10 x 5 x 2 mm^3 samples. These samples were surface grinded to remove the EDM layer, followed by mechanical polishing prior to joining. A customized loading fixture of rectangular alumina plates with one hole at each corner along with appropriate alumina screws and bolts was

prepared to hold both the NiTi and Ti_3SiC_2 samples on top of each other during bonding at joining temperatures. At room temperature, the whole fixture with samples between them was compressed to a uniaxial stress of 150 MPa and unloaded to 20 MPa in an MTS Insight electromechanical test frame. Holding the load that corresponds to stress at 20 MPa, the bolts were tightened in the fixture and the load was removed afterwards. The objective of initial pre-loading was to achieve good, intimate contact between the mating surfaces. The fixture was then placed in an alumina boat in the tube furnace (MTI Corporation, Model GSL 1600X) to carry out bonding experiments. The vacuum level in the tube furnace was held at 2×10^{-2} Pa for 5 minutes followed by purging with ultra-high purity Argon. The purging process was repeated once again before heating the samples to desired temperatures in flowing argon environment as it is important to have an oxygen free atmosphere to prevent the formation and growth of oxide films at elevated temperatures. The presence of oxide layer on either of the mating surfaces prevents their contact and degrades the kinetics of interface creation by hindering the diffusion [157]. Heating/cooling rate of 5°C/min was used during bonding experiments in the tube furnace.

3.3 Microstructural Characterization

3.3.1 SEM

The microstructures of the as-sintered samples were characterized using field emission scanning electron microscopes (FE – SEM, Quanta 600 FEG, FEI, Oregon, USA and JSM-7500F, JEOL, Tokyo, Japan) after standard metallographic polishing

procedure. Energy dispersive spectroscopy (EDS) was used for quantitative analysis of different phases, through EDS spot analysis. The cross-sections of the bonded NiTi-Ti_3SiC_2 samples were cut using a low speed diamond saw before mounting in epoxy, and polished using standard metallographic procedures up to final step of polishing with 1 µm diamond paste followed by ultrasonic cleaning in ethanol. The microstructures of the interfaces were characterized using a field emission scanning electron microscope (FE – SEM, Quanta 600 FEG, FEI, Oregon, USA). Rectangular bars of the dimension (32 x 5 x 2) mm were cut from the bilayer discs using EDM. Both the surfaces of the all the bars were polished using standard metallography techniques up to final step of polishing with 0.25 µm diamond paste followed by ultrasonic cleaning in ethanol. Observation of pre-crack and microstructural characterization of the interface was done using a field emission scanning electron microscope (FE – SEM, Quanta 600 FEG, FEI, Oregon, USA). One surface of each bar was spray painted by a white paint followed by a sticking a scale printed on it using a glue. This was done to obtain the maximum contrast on the surface to monitor crack propagation using a digital camera during four point bend testing.

3.3.2 DSC

TA Instruments, Q20^{TM} differential scanning calorimeter (DSC), was used to ascertain the phase transformation in the composites after sintering in the SPS. Specimens were cut using diamond saw and grinded using 180 grit SiC paper so that they could fit in a DSC pan which was 5 mm in diameter and 2 mm in thickness. The

specimens were thermally cycled 10 times between 0 and 150°C at a heating – cooling rate of 10°C/min. The slope line extension method was used to determine the stress free transformation temperatures from the peaks observed in DSC curves [158]. The transformation temperatures and enthalpies were determined from the second cycle in the DSC curves.

3.3.3 EPMA/WDS

Electron micro probe analysis (EPMA) was used for quantitative analysis of different phases in the interface, through the spot analysis. An excitation voltage of 15keV and a beam current of 10 nA was used in the spot analysis. Energy dispersive spectroscopy (EDS) line scan was also carried out to determine the elemental distribution across the interface.

3.3.4 EBSD

Electron backscattered diffraction (EBSD) was used to determine the reaction phases in the interface. An additional polishing step using a 0.05 µm colloidal silica solution was necessary for the EBSD characterization. The SEM used for the characterization was a Zeiss Ultra Plus FEGSEM, equipped with an Oxford Instrument AZtec EDS and Electron Backscatter Diffraction (EBSD) system and a Nordlys nano EBSD detector. The accelerating voltage was set at 20 keV and the working distance was between 10 and 12 mm. The step size used to scan the area of interest was 50 nm.

3.4 Thermomechanical Characterization

Isobaric heating-cooling experiments under uniaxial compressive stresses were conducted to study the shape memory behavior and the evolution of transformation temperatures, transformation and irrecoverable strains as a function of applied stress on NiTi and the NiTi/Ti_3SiC_2 composites. Evolution of two way shape memory effect (TWSME) was also studied after each isobaric heating-cooling cycle. Compression samples with the dimensions of 4 x 4 x 8 mm^3 were cut using wire electrical discharge machining (EDM). An MTS Insight electromechanical test frame and an MTS 12.7 mm gage length extensometer, (Model # 632.53 E-14) with a strain range of ± 20% attached on the WC grips, were used for the thermo-mechanical experiments. Specimens were heated by conduction from the hot grips around which heating bands were wrapped. Liquid nitrogen was circulated through the copper tubes wrapped around the grips to cool the specimens. Temperature was measured using three K-type thermocouples with one directly attached on the specimen and one on each grip. Specimens were thermally cycled between 20 and 150°C at a heating-cooling rate of 8°C/min which was used to maintain a small and steady difference between the temperatures of the grips and specimen throughout the experiment.

3.5 Mechanical Property Characterization

3.5.1 Energy Dissipation

Uniaxial cyclic compression tests were performed on similar compression specimens at room temperature in the MTS Insight test frame. A 3mm gage length

extensometer with a range of ± 8% directly attached to the sample was utilized for accurate strain measurements. Two loading-unloading cycles were performed at each stress starting at 50 MPa with 25 MPa increments up to 250 MPa under displacement control mode with a crosshead displacement rate of 0.005 mm/s. Upon reaching 250 MPa, they were cycled once at each stress with 25 MPa decrements down to 50 MPa. Energy dissipation per unit volume per loading-unloading cycle (W_d) was calculated at each stress level from the area inside the stress-strain loop for all the specimens. Both the mechanical tests, namely isobaric heating-cooling under compression (thermo-mechanical cycling) and cyclic compression tests at room temperature were performed only on NiTi/Ti_3SiC_2 composite processed at 980°C (referred to as SPS # 3 in Table 3.1). Based on the low porosity and high amount of transformable phase of NiTi in the NiTi/Ti_3SiC_2 composite, SPS # 3 was selected for these mechanical tests. Two batches of SPS # 3 composites were prepared for the mechanical tests. On the first batch, only cyclic compression tests were performed to measure energy dissipation of as-sintered composite. On the second batch of as-sintered (AS) composites, isobaric heating-cooling tests (thermo-mechanical cycling) were performed under compression to characterize shape memory behavior which was followed by cyclic compression tests to determine energy dissipation of thermo-mechanically cycled (TC) composites. The compression axis in all the experiments was perpendicular to the loading direction in the SPS.

3.5.2 Nanoindentation

The nano-indentation measurements across the NiTi-Ti_3SiC_2 interface were conducted using an Agilent Technologies G200 Nanoindenter and a diamond Berkovich indenter tip. A maximum penetration depth of 250 nm was used for all the indents. An array of indents was made to map the elastic modulus and hardness of different phases in and around the NiTi- Ti_3SiC_2 interface.

3.5.3 Vickers Micro-Hardness Test

Vickers Micro-Hardness tests were also carried out across the interface for qualitative analysis. A series of indentation loads (0.1, 0.2, 0.3 and 0.5 kg) were used to obtain indents on the interface using diamond pyramidal indenter. For each indent, a dwelling time of 13 seconds at peak load was used. Post Vickers SEM was used to observe the indentations and regions around them. Both the nano-indentation and Vickers micro-hardness tests were conducted at ambient temperature where NiTi is in fully martensite phase.

3.5.4 Four Point Bend Tests

Tests were carried using a four point bend fixture obtained from TESTRESOURCES Model G238X attached to a MTS Insight electromechanical test frame with a MTS load cell of 2.5 kN under displacement control at a constant displacement rate of 0.002 mm/s. Inner and outer loading span of 14 and 28 mm respectively, was used during the tests. A pre-load of 15 N was applied to ensure contact

with the sample. SEM Micrographs of the interface were obtained after the tests to characterize the crack propagation path.

4. THERMOMECHANICAL RESPONSE OF COMPOSITES*

4.1 DSC

Figure 4.1 shows a typical DSC curve of the NiTi/Ti_3SiC_2 (SPS # 3) composite. The presence of peaks in the DSC curve suggests martensitic phase transformation in the NiTi phase of the SPS # 3 composite. Area under the cooling (heating) peak represents the enthalpy of transformation from austenite to martensite (respectively, martensite to austenite). As the enthalpy of transformation is the amount of energy required for the transformation per gram of the composite, it is possible to obtain the weight and volume fraction of the transformable NiTi phase present in the composite by comparing it with the enthalpy of pure NiTi using the equations 6-8 below.

$$W^{NiTi} = \frac{\Delta H^{comp.}}{\Delta H^{NiTi}} \times 100 \quad (6)$$

$$W^{Ti3SiC2} = 100 - W^{NiTi} \quad (7)$$

$$V_f^{NiTi} = \frac{(W^{NiTi} / \rho^{NiTi})}{[(W^{NiTi} / \rho^{NiTi}) + (W^{Ti3SiC2} / \rho^{Ti3SiC2})]} \times (100 - P_{overall}) \quad (8)$$

W^{NiTi} is the weight % of NiTi, $W^{Ti3SiC2}$ is the weight % of Ti_3SiC_2 in the composite, $\Delta H^{comp.}$ is the enthalpy of transformation of the composite, ΔH^{NiTi} is the enthalpy of

*Part of this section is reprinted with permission from "Thermomechanical Response and Damping Behavior of Shape Memory Alloy–MAX Phase Composites" by Kothalkar et. al., Metallurgical and Materials Transactions A, 45, 1-13, [2014] by Springer

transformation of pure equiatomic bulk NiTi, V_f^{NiTi} is the volume fraction of NiTi (vol. %) in the composite, ρ^{NiTi} is the theoretical density of NiTi, $\rho^{Ti3SiC2}$ is the theoretical density of Ti_3SiC_2, $P_{overall}$ is volume fraction of overall porosity (vol. %) in the composite.

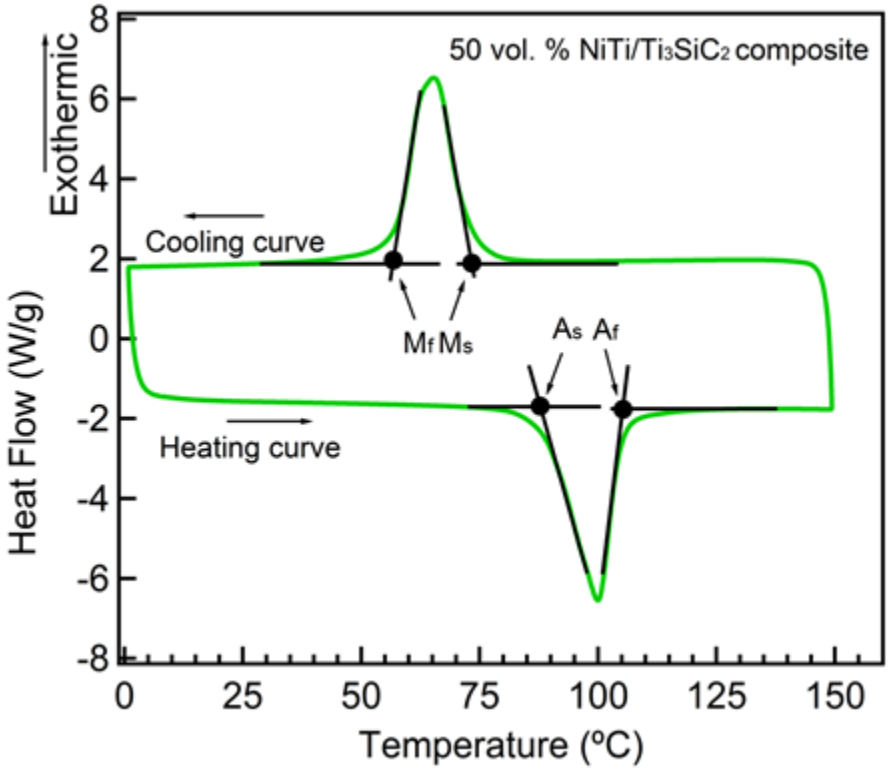

Figure 4.1 Differential scanning calorimetry (DSC) curve clearly showing the transformation in the SPS # 3 composite. It also depicts the method for determining the transformation temperatures

Table 4.1 lists the values of the transformation temperatures (M_s: Martensite start and A_f: Austenite finish, directly determined from the DSC curve shown in Figure 4.1), the enthalpy of transformation ($\Delta H^{A\rightarrow M}$), the weight and volume % of the transformable NiTi phase for all the composite samples. The table also compares their transformation temperatures and enthalpy values to that of pure equiatomic bulk NiTi. A slight decrease is observed in the transformation enthalpy ($\Delta H^{A\rightarrow M}$) of the composite as the sintering temperature is increased from 960 to 980°C. However, a sharp decrease in transformation enthalpy is evident when the sintering temperature is increased to 1000°C even though the sintering time is reduced to only 3 minutes. As the NiTi is the only transformable phase in the composite, the enthalpy has a direct correlation to the amount of NiTi transforming in the composite. SPS # 4 has the lowest and SPS # 1 has the highest amount of transformable NiTi present in the composite. This is assuming that the new reaction phases formed do not transform.

Calculation of the volume fraction of the transformable phase is based on the assumption that weight and volume fraction of the reaction phases is small as compared to individual NiTi and Ti_3SiC_2 phases. The observed vol.% of the transformable NiTi in the composite is 10 to 18% less than that of starting powders of the composite which had 50 vol. % NiTi. Possible explanations for lower volume percentage of transformable NiTi are: (a) the consumption of some NiTi by the reaction with Ti_3SiC_2 during sintering leading to the formation of new non-transforming phases such as Ti_2Ni, Ti_5Si_3 and NiTiSi at the interface [159]; (b) formation of Ti_2Ni precipitates in NiTi due to the Ni diffusion towards the interface with Ti_3SiC_2, and (c) the presence of dislocation density

which can partially inhibit transformation. It has been reported earlier that cold work or presence of high dislocation densities can be the reason for non-transforming NiTi [133, 160]. The investigations on NiTi/TiC composites reported that not all the NiTi present in the composites transforms [133].

Table 4.1 Summary of the DSC results for 50 vol. % NiTi/Ti_3SiC_2 composites, their transformation temperatures and enthalpies, and the amount of transforming phase in the composite

Sample name	Enthalpy of transformation, Austenite to Martensite, ($\Delta H^{A\rightarrow M}$) (J/g)	Martensite start (M_s) (°C)	Austenite finish (A_f) (°C)	$\Delta T = A_f - M_s$ (°C)	Wt. % of the transformable NiTi phase in the composite	Vol. % of the transformable NiTi phase in the composite*
SPS # 1	**17.6**	**74**	**110**	**36**	**57.7**	**40.6**
SPS # 2	**17.5**	**73**	**108**	**35**	**57.4**	**40.5**
SPS # 3	**17.5**	**71**	**104**	**33**	**57.4**	**40.5**
SPS # 4	**14.6**	**71**	**104**	**33**	**47.4**	**32.0**
Pure NiTi (bulk)	**30.5**	**78**	**114**	**36**	-	-

*Initial powder mixture (before sintering) contained 50 vol% of transformable NiTi

In the current study, the composites are cooled from sintering temperatures to room temperature under 100 MPa stress. Residual stresses created by thermal expansion

mismatch and the transformation strains under 100 MPa stress may get relieved through the formation of dislocations, thus reducing the amount of transforming NiTi phase. The fact that the transformation temperatures observed in NiTi/Ti_3SiC_2 composites are close to that of equiatomic NiTi eliminates the possibility of compositional changes being the reason of non-transforming NiTi in the composites (Table 4.1). All the NiTi/Ti_3SiC_2 composites show similar transformation temperatures and temperature hysteresis ($\Delta T = A_f - M_s$).

4.2 Thermo-mechanical Cycling of As-Sintered (AS) SPS # 3 Composite

The aim here is to investigate whether the composites show reversible shape change or not, and how it is affected by the magnitude of applied stress. One of the goals of this work is also to evaluate energy dissipation potential of the novel NiTi/Ti_3SiC_2 composites and understand the effect of thermo-mechanical treatment on the energy dissipation in the composites rather than to optimize the processing conditions.

Figure 4.2 shows a detailed flowchart of thermal cycling under uniaxial compressive stresses for the SPS # 3 composite. To begin with, a minimum constant stress of 10 MPa is applied during thermal cycling to accurately measure strain changes due to the transformation in the NiTi phase of the composite. Stress is increased incrementally to 50, 75 100, 150 and 200 MPa in the austenite phase and at each stress, the composite is thermally cycled once from the austenite to martensite phase and back, in order to obtain its stress-temperature relationship. At the end of thermal cycle at each of the 100, 150 and 200 MPa stresses, the composite is unloaded to 10 MPa in the

austenite phase and thermally cycled once to study the evolution of TWSME with prior thermo-mechanical treatments. The thermal cycling at different stresses is performed on the same specimen. Bulk pure equiatomic NiTi is also subjected to the same thermal history for meaningful comparison with the SPS # 3 composite.

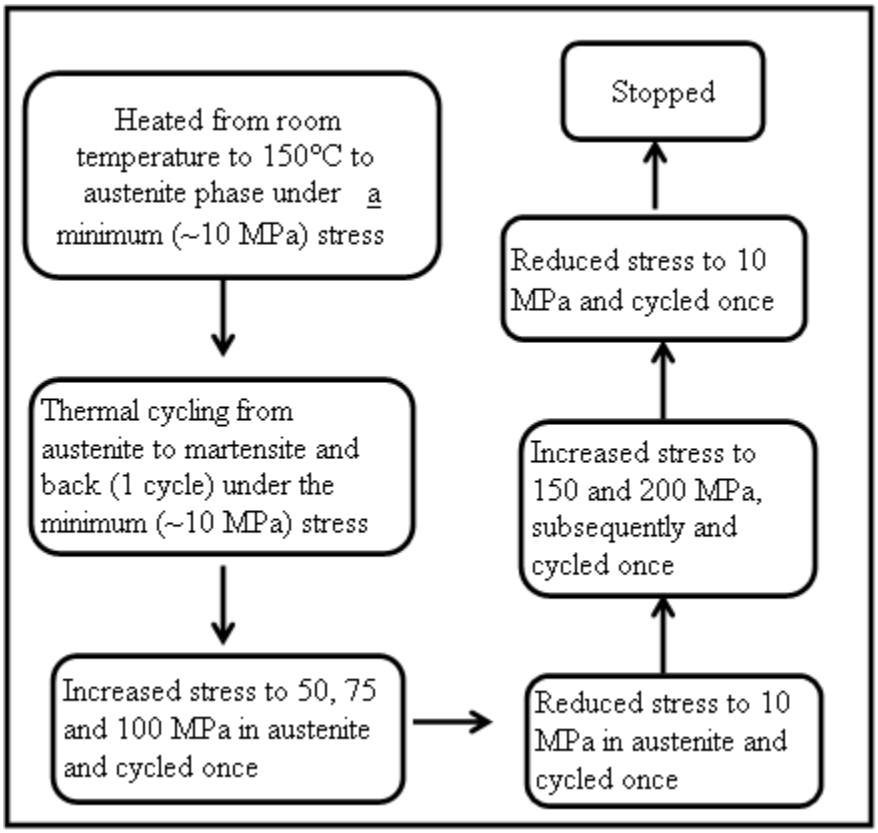

Figure 4.2 Flowchart of thermal cycling under compressive stresses for SPS # 3 composite and pure equiatomic NiTi. All the cycles at different stresses are on the same sample

4.2.1 One Way Shape Memory Effect

Figures 4.3 and 4.4 show strain versus temperature plots under increasing compressive stresses for the SPS # 3 composite and pure NiTi respectively. The 75 MPa stress cycle in both the composite and the NiTi is omitted for clarity. It is observed that important shape memory characteristics such as transformation temperatures, transformation and irrecoverable strains change as a function of stress for both the composite and bulk NiTi. These are analyzed in detail in the following sections. Figure 4.5 includes a schematic showing the method for measuring transformation temperatures, transformation and irrecoverable strains in the NiTi and the composite.

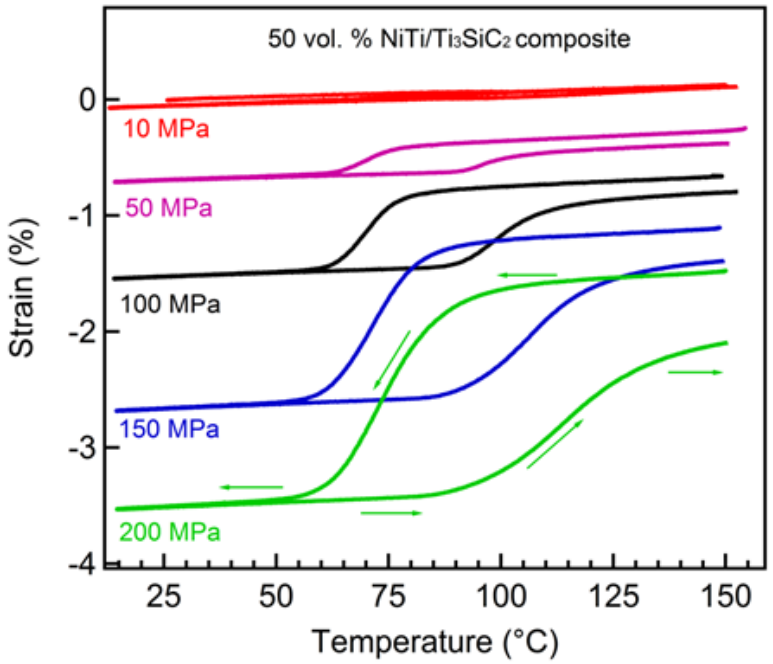

Figure 4.3 Strain versus temperature plots under increasing compressive stresses for SPS # 3 composite

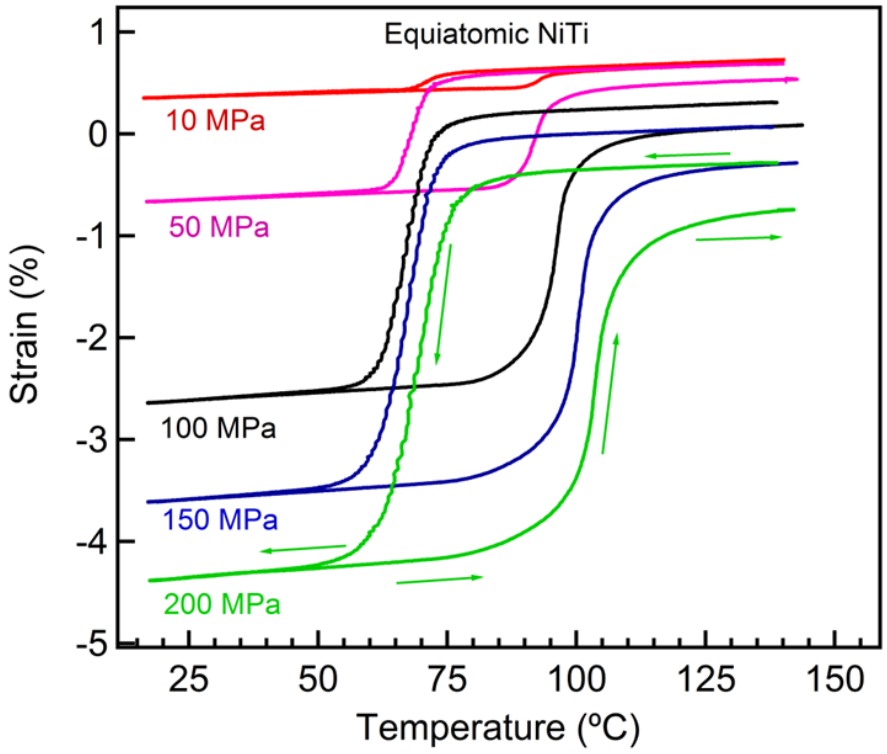

Figure 4.4 Strain versus temperature plots under increasing compressive stresses for equiatomic bulk NiTi

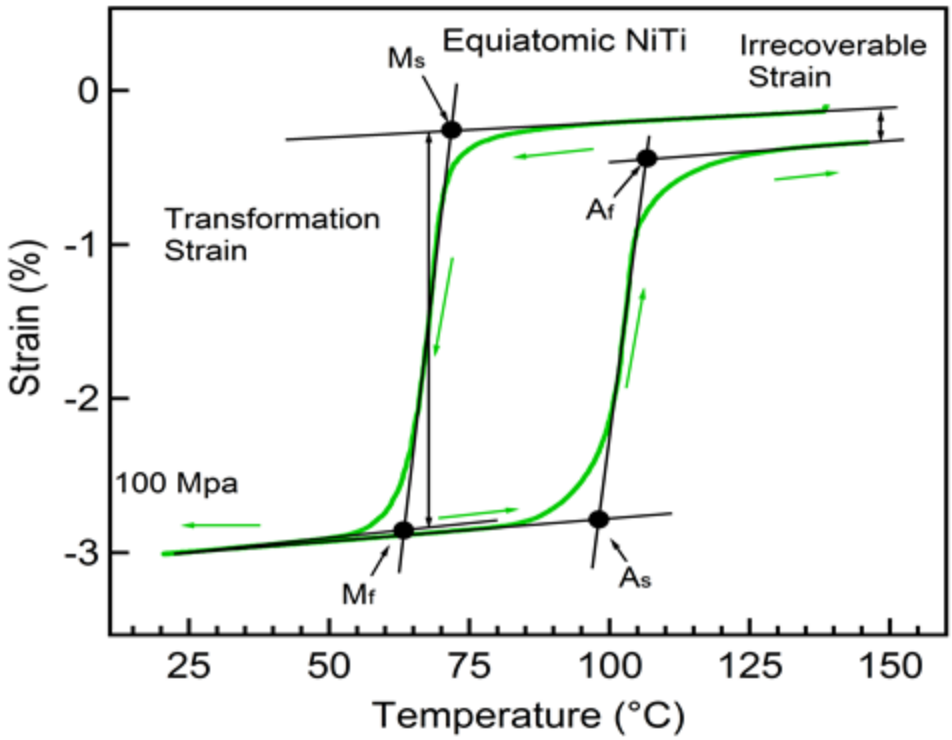

Figure 4.5 Schematic depicting the method used for measuring transformation temperatures and transformation and irrecoverable strains of NiTi and composites

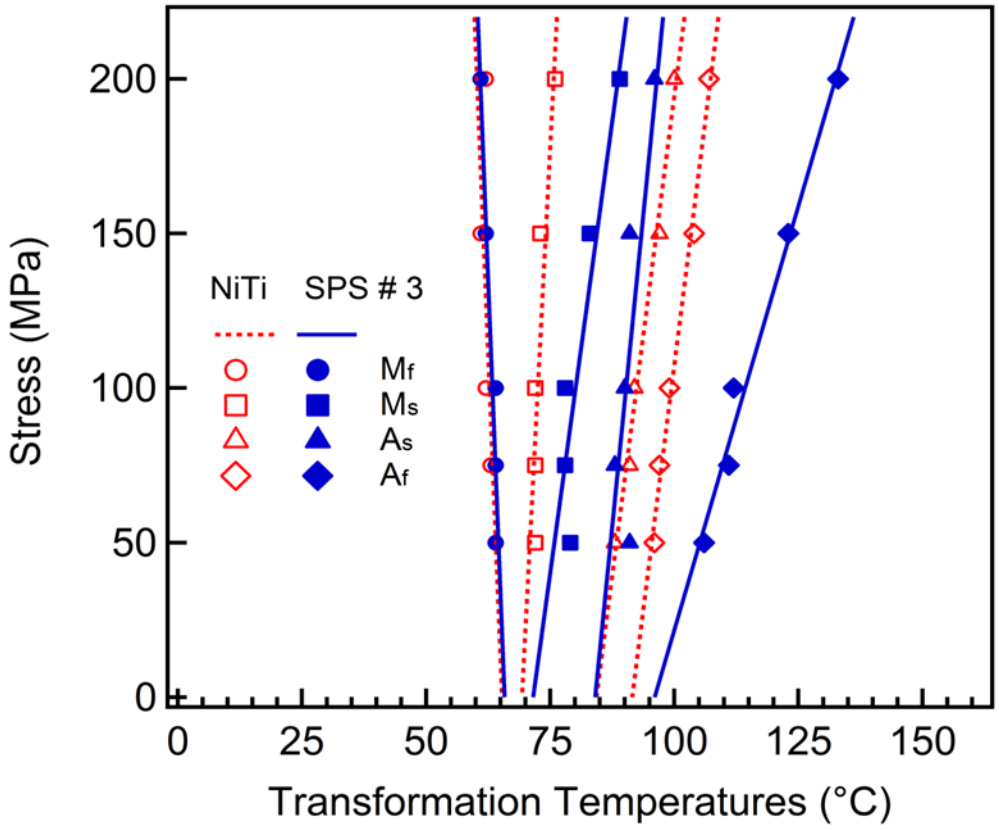

Figure 4.6 Evolution of the transformation temperatures with increasing compressive stresses (Clausius-Clapeyron plot) for the SPS # 3 composite (solid lines) and its comparison with that of bulk NiTi (dotted lines)

4.2.1.1 Evolution of Transformation Temperatures with Stress

Stress-temperature plots of the SPS # 3 composite and pure NiTi are shown in Figure 4.6. Owing to the fact that martensitic transformation involves shear deformation, application of stress assists in the martensitic transformation. This leads to the shift of martensitic transformation temperatures to higher values under external stresses. Pure NiTi nicely follows this trend as both the austenite (martensite) start, A_s (M_s), and

austenite finish, A_f, temperatures are shifted by almost the same amount at each stress value.

For the SPS # 3 composite, M_s and A_f are shifted to higher values whereas M_f and A_s remain almost the same or are slightly lowered, as compared to those of pure NiTi under the same external stress level. This shift in transformation temperatures leads to the broadening of the transformation ranges (i.e. A_f-A_s and M_s-M_f) at each stress. The most probable reason for the observed increase in M_s and A_f values in the composite is the creation of local stress concentrations due to porosity and non-transforming reaction phases at the interface between NiTi and Ti_3SiC_2. These stress concentrations lead to early initiation of forward and reverse transformation in the composite as compared to pure NiTi.

There are two reasons that can lead to lowering of M_f and A_s temperatures when compared with unreinforced NiTi. First, the presence of non-transforming ceramic regions around the NiTi can cause a back stress due to the volume and shape mismatch when the martensite plates nucleate and propagate, thus requiring higher driving force to finish the transformation [133, 136]. Reorientation/detwinning cannot be completed because of the presence of constraints and thus the reverse transformation is easier which leads to reduction in A_s. It is well-known in SMAs that the A_s temperature of reoriented/detwinned martensite is notably higher than that of twinned martensite. Moreover, the stiffness of the NiTi phase is further lowered during the transformation, thus decreasing the stress experienced by the NiTi phase [161]. This may lead to a decrease (respectively, increase) in the forward (respectively, reverse) transformation

finish temperatures. Numerous other investigations have also reported a decrease in M_f and A_s [162, 163]. The lower M_f and A_s values as compared to pure NiTi are also in agreement with the earlier reported observations on NiTi/TiC composites where TiC was added as a reinforcement of up to 20 vol. % [133, 136]. However, the increase in M_s and A_f values does not agree with the observed behavior in NiTi/TiC composites [133, 136] and that predicted by micromechanical modeling of SMA-ceramic composites [161]. The difference lies in the nature of the SPS # 3 composite, which is interpenetrating and contains some residual porosity and reaction layers whereas in the aforementioned studies [133, 136, 161], the discrete reinforcements added has a maximum volume fraction of 20% with little or no porosity and reaction layers.

4.2.1.2 Evolution of Transformation and Irrecoverable Strains with Stress

In SMAs which show only one way shape memory effect, when the austenite is cooled below M_f temperatures under almost zero stress, austenite transforms into martensite with several possible variants with no notable macroscopic shape change. The structure thus obtained is referred to as “self-accommodated” martensite since the different variants form to minimize the shape change and thus the energy. When the self-accommodated martensite is stressed at constant temperature, some variants grow at the expense of others and form a single variant martensite. This process is called martensite reorientation or detwinning and is always accompanied by macroscopic shape change. When polycrystalline SMAs are cooled under low stresses from austenite to martensite, some grains for twinned and others detwinned martensite depending on the grain

orientation and minimum stress required for detwinning. Formation of detwinned martensite is accompanied by macroscopic shape change measured as transformation strain shown in Figure 4.5. As the stresses are increased, more detwinned martensite forms and higher transformation strains are observed. The transformation strains increase with the applied stresses for pure NiTi and SPS # 3 composite as shown in Figure 4.7. Smaller transformation strains are observed in SPS # 3 composite as compared to pure NiTi due to the following reasons: first, the SPS # 3 composite has less than 50 vol. % of pure transformable NiTi; secondly, the stress experienced by the NiTi phase in the composite is less than the applied external stress because the stiffer Ti_3SiC_2 phase carries most of the stress; and lastly, the Ti_3SiC_2 phase puts a constraint on the amount of detwinning occurring by not allowing the martensite to detwin in order to maintain the compatibility across the interfaces.

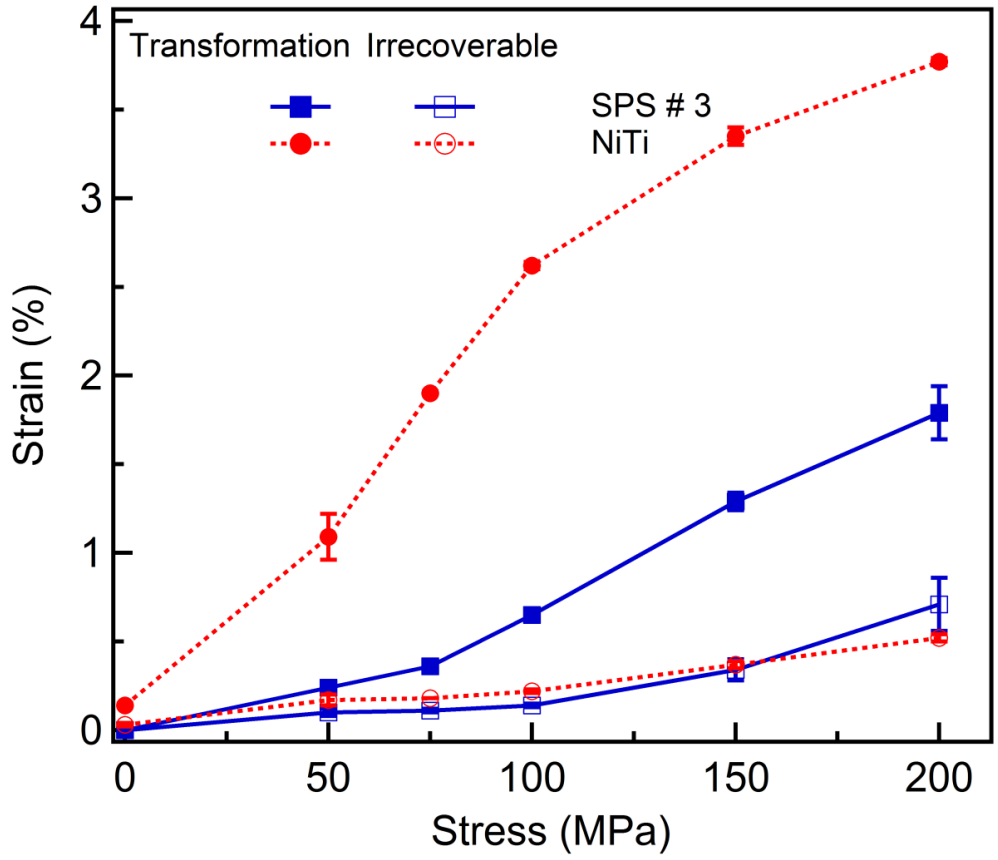

Figure 4.7 Evolution of the transformation (red color)) and irrecoverable (blue color) strains with increasing compressive stresses for SPS # 3 composite and its comparison with that of bulk NiTi

Irrecoverable strains in SMAs is usually caused by generation and motion of dislocations (transformation induced plasticity) and remnant martensite that does to transform back to austenite even after heating above A_f (retained martensite). Thus, irrecoverable strains increase on increasing the applied stresses due to higher transformation induced plasticity and amount of retained martensite, as observed in Figure 4.7. Interestingly, the irrecoverable strains for the SPS # 3 composite is very close to that of pure NiTi, even after having large difference in the transformation strains, at

each stress value. The ratio of the irrecoverable to transformation strains of the SPS # 3 composite and pure NiTi at each stress provides a better comparison for the reversibility of the martensitic transformation in the composite and the pure NiTi (Figure 4.8). This ratio is much higher for the SPS # 3 composite than that of pure NiTi which suggests that more factors are contributing towards the irrecoverable strain in the SPS # 3 composite than those mentioned above for pure SMAs (NiTi). Irrecoverable strain in the composite is arguably a sum of two contributions: irrecoverable strain in NiTi and irrecoverable strain in Ti_3SiC_2. Irrecoverable strain in NiTi can be further categorized into two parts: one caused by dislocations and retained martensite in NiTi, irrespective of the presence of Ti_3SiC_2 around it; second caused by generation of dislocations and retained martensite due to the presence of Ti_3SiC_2 in the NiTi region, especially closer to the interface between NiTi and Ti_3SiC_2. Irrecoverable strain in Ti_3SiC_2 could be due to dislocation glide in individual grains and their bending or kinking. Some of the irrecoverable strain in Ti_3SiC_2 can possibly come from delamination, that does not propagate, but remains contained within the grain.

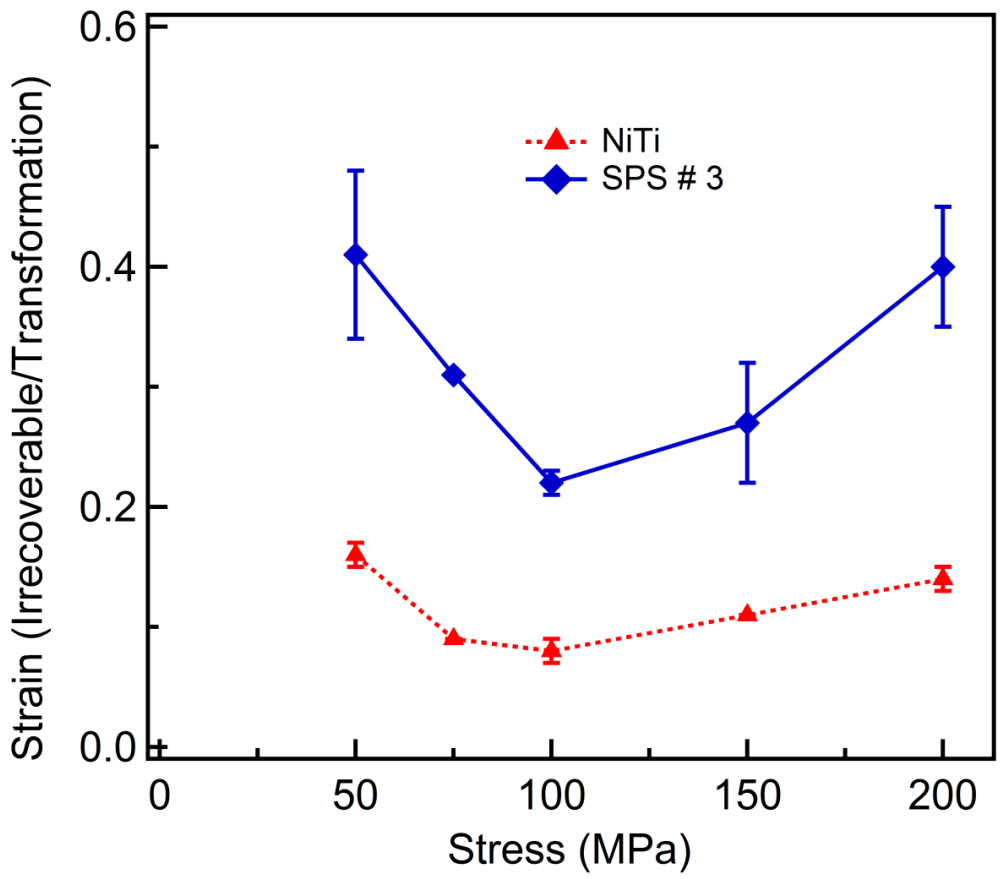

Figure 4.8 Comparison of the ratio of irrecoverable to transformation strains of SPS # 3 composite with that of bulk NiTi at different compressive stresses

During the transformation from austenite to martensite, high local strains and thereby high local stresses are generated due to the geometric constraints imposed by the Ti_3SiC_2 phase. Stress as high as 700 MPa have been reported in the literature when SMA is prevented from returning to high temperature phase upon heating due to external constraints [164]. These high stresses coupled with local stress intensity factors induced by pores and voids can generate very high local stresses causing deformation of Ti_3SiC_2.

In fully dense Ti_3SiC_2, deformation is completely reversible up to 1 GPa stress under compressive loadings at room temperature [4]. However, the presence of porosity in the composite may cause irrecoverable deformation in Ti_3SiC_2 at lower stresses than mentioned above, thus contributing to the total irrecoverable strain of the SPS # 3 composite. It is difficult to estimate quantitative contributions of each factor at this time and specially designed experiments and/or finite element modeling are needed to estimate them.

4.2.2 Two Way Shape Memory Effect (TWSME)

Figures 4.9 and 4.10 show the two way shape memory strain versus temperature plots for the SPS # 3 composite and pure equiatomic NiTi, respectively. Firstly, the as-sintered SPS # 3 composite is thermally cycled under minimum stress (10 MPa) to determine whether the residual stresses generated during cooling from the sintering temperatures are sufficient to cause transformation. No significant TWMSE strain is detected in the composite. As previously described, to investigate the formation of internal stress and study its evolution, the SPS # 3 composite is thermally cycled once under minimum stress (10 MPa) after cycling each at 100, 150 and 200 MPa stress. Transformation strains obtained during thermal cycling at 100, 150 and 200 MPa stresses and two way shape memory (TWSM) strains obtained under minimum stress after cycling at these stresses are compared for the SPS # 3 composite and pure equiatomic NiTi in 4.11 Compressive TWSM strains are observed for both the SPS # 3 composite and the NiTi and are found to increase with stress, similar to transformation

strains. As the stress under which the samples are cycled is increased, further dislocation storage occurs leading to more plastic deformation of martensite and more retained martensite in austenite, consequently higher internal stresses and TWSM strains are obtained as shown in Figure 4.11.

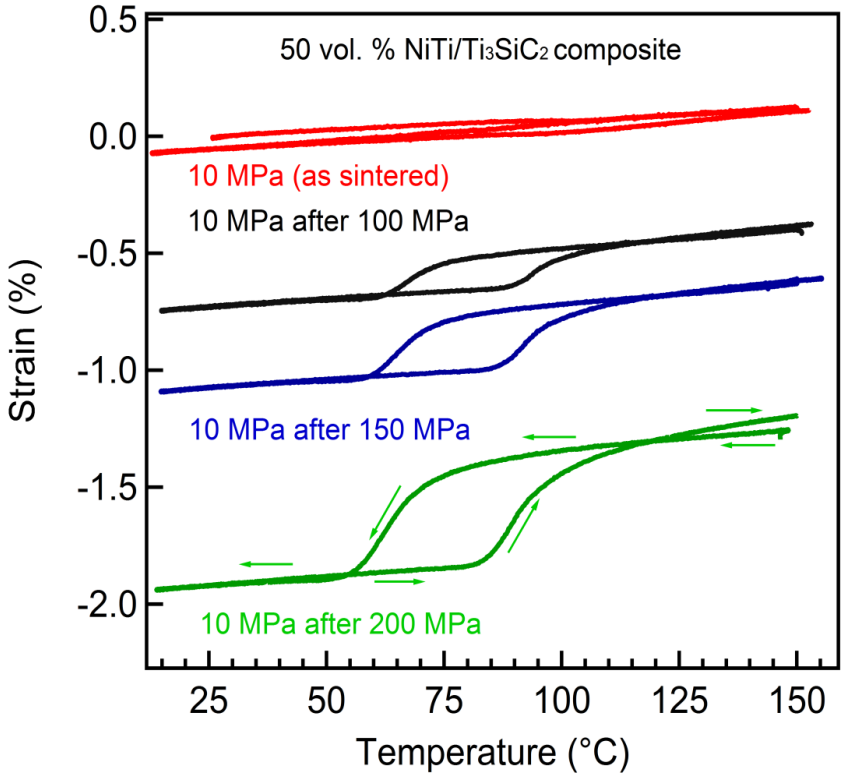

Figure 4.9 Evolution of two way shape memory effect (TWSME) with increasing compressive bias stresses during prior thermo-mechanical cycling for the SPS # 3 composite

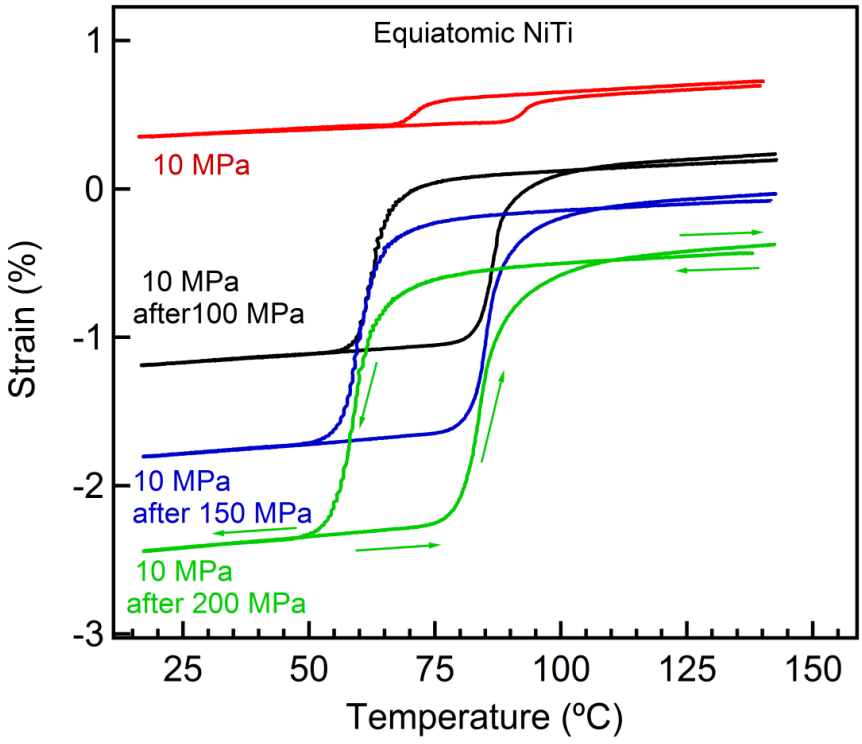

Figure 4.10 Evolution of two way shape memory effect (TWSME) with increasing compressive bias stresses during prior thermo-mechanical cycling for the equiatomic bulk NiTi

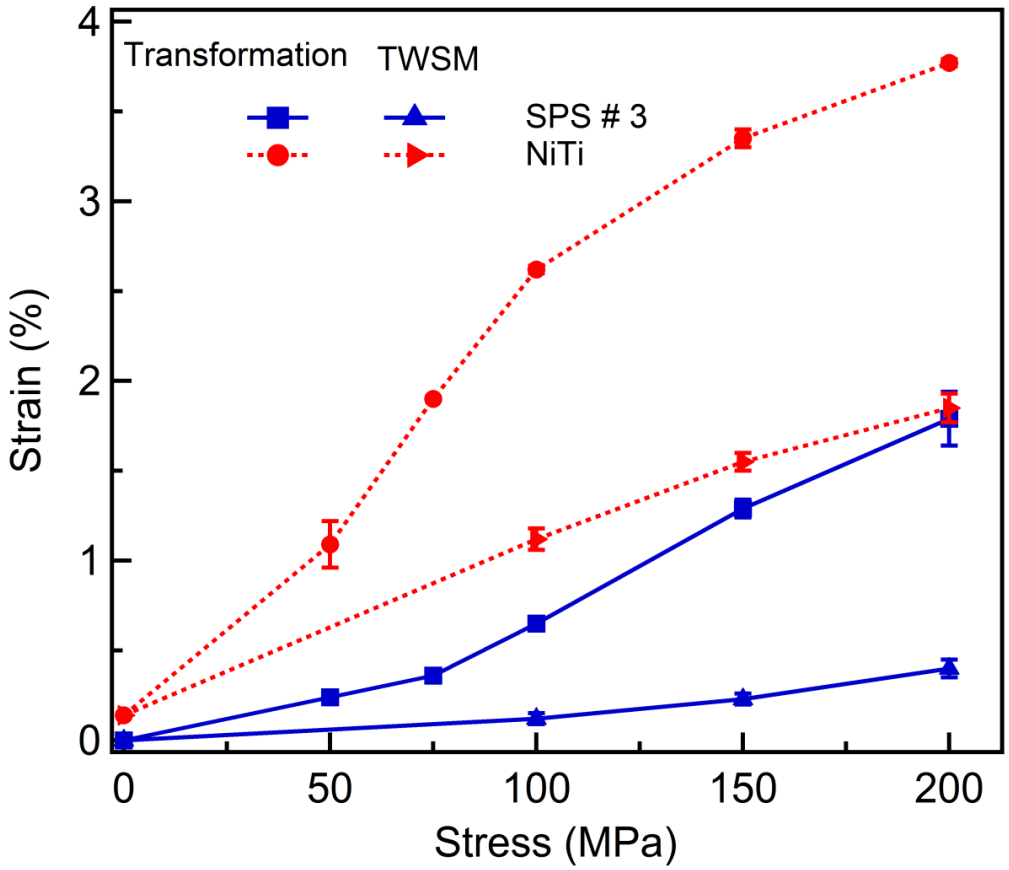

Figure 4.11 Evolution of the transformation and two way shape memory (TWSM) strains with increasing compressive stresses for the SPS # 3 composite and its comparison with that of bulk NiTi

Lower TWSM strains in the SPS # 3 composite are obtained as compared to pure NiTi after thermal cycling at same stresses. This is due to the fact that the composite shows lower transformation strains as the amount of transformable NiTi and the stress experienced by the NiTi phase in the composite is less than that in bulk NiTi. Similar to irrecoverable and transformation strain comparison described in the previous section, the ratio of the TWSM to transformation strain of the SPS # 3 composite and pure NiTi at

each stress provides a better comparison (Figure 4.12). This ratio is much lower for the SPS # 3 composite than that of pure NiTi, which indicates that the formation of directional internal stresses is hindered by the presence of the Ti_3SiC_2 phase.

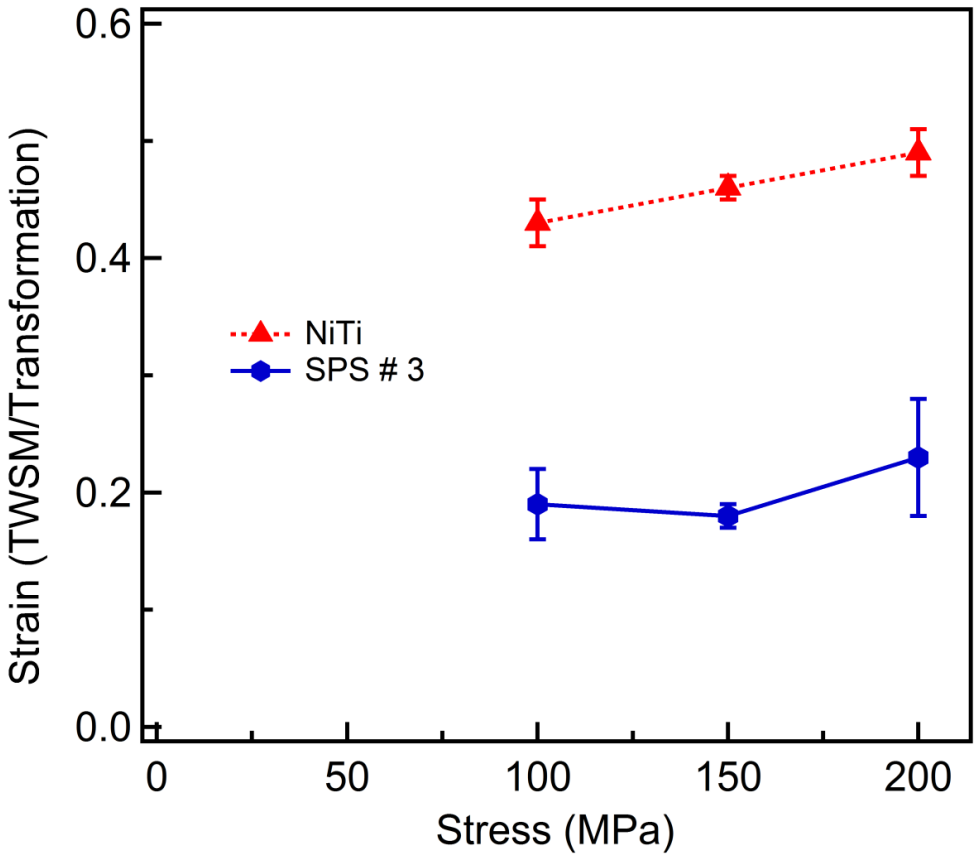

Figure 4.12 Comparison of the ratio of two way shape memory (TWSM) strain obtained at 10 MPa to transformation strain of the SPS # 3 composite with that of bulk NiTi after cycling at same stresses of 100, 150 and 200 MPa

4.3 Summary

- Microstructural characterization via scanning electron microscopy clearly depicted the presence of two distinct, interconnected phases, NiTi and Ti_3SiC_2, along with some remnant porosity in the composites. Martensitic transformation in NiTi/Ti_3SiC_2 composites was confirmed by the transformation peaks observed using differential scanning calorimetry. One way and two way shape memory effects were observed in the composites during thermo-mechanical characterization.
- The stress-temperature phase diagrams of the composites are analyzed and compared to those of pure NiTi. For the composite, M_s and A_f are shifted to higher values whereas M_f and A_s stayed the same or are shifted to slightly lower values, as compared to pure NiTi, at each stress. The increase in the M_s and A_f is due to the creation of local stress concentrations when external load is applied as a result of porosity and non-transforming reaction phases at the interface between NiTi and Ti_3SiC_2. Lowering of M_f and A_s is attributed to two factors: firstly, the presence of non-transforming ceramic regions around the transforming NiTi may cause a back stress due to deformation mismatch when the martensite plates propagate, thus requiring higher driving force to finish the transformation. Secondly, the stiffness of the NiTi phase is lowered during the transformation, thus decreasing the stress experienced by the NiTi phase, leading to a decrease (respectively, increase) in the forward (respectively, reverse) transformation finish temperatures.
- Transformation and irrecoverable strains in the composites show similar trend as observed in pure NiTi; both increase with increasing applied external stress.

However, the ratio of irrecoverable to transformation strains of the composite is higher when compared to that of pure NiTi and the additional irrecoverable strain is caused because of the constraints imposed by the Ti_3SiC_2 phases around the transforming regions in NiTi and possible deformation of Ti_3SiC_2 phase (e.g. formation of permanent kink bands).

- Similar to the one way effect, increase in TWSM strain is observed with increase in applied external stress during prior thermo-mechanical cycling. The ratio of TWSM to transformation strain in the composite is lower than that in pure NiTi because the presence of Ti_3SiC_2 interpenetrating regions and the complex stress state at the interface between NiTi and Ti_3SiC_2 upon transformation prevents the accumulation of enough directional internal stresses that lead to TWSME.

5. ENERGY DISSIPATION BEHAVIOR OF COMPO SITES*

5.1 Energy Dissipation

Both the as-sintered (AS) and thermo-mechanically cycled (TC) SPS # 3 composites, show fully reversible, closed, non-linear hysteretic stress-strain loops when loaded in compression. During cyclic loading with increasing maximum stress, the first loop is always slightly open while the second loop is closed. This behavior, typical for pure MAX phases [153], is also observed in bulk NiTi in martensite. During cyclic loading with decreasing maximum stress, all the loops at and below 200 MPa are closed for both the composites (AS and TC) and their individual constituents (NiTi and Ti_3SiC_2). W_d, energy dissipation per unit volume per loading-unloading cycle, is calculated at each peak stress by measuring the area inside the stress-strain loops. Energy dissipation is calculated only from the fully reversible, closed hysteretic loops during cyclic loading from decreasing maximum stress. Figure 5.1 shows one representative engineering stress-strain loop at 200 MPa for each material, namely fully dense pure Ti_3SiC_2, pure NiTi, TC pure NiTi, AS and TC SPS # 3 composites. The energy dissipation is the highest for the TC composite followed by AS composite, pure NiTi, TC pure NiTi and fully dense pure Ti_3SiC_2. To compare the energy dissipation

---

*Part of this section is reprinted with permission from "Thermomechanical Response and Damping Behavior of Shape Memory Alloy–MAX Phase Composites" by Kothalkar et. al., Metallurgical and Materials Transactions A, 45, 1-13, [2014] by Springer

capacity at varying stress levels for different materials, the energy dissipation (W_d) is plotted as a function of maximum stress squared in Figure 5.2. For pure Ti_3SiC_2 phases, a linear dependence of W_d on σ^2 is predicted and experimentally observed where σ is the maximum applied stress [56]. On plotting W_d as a function of σ^2 for the pure NiTi and

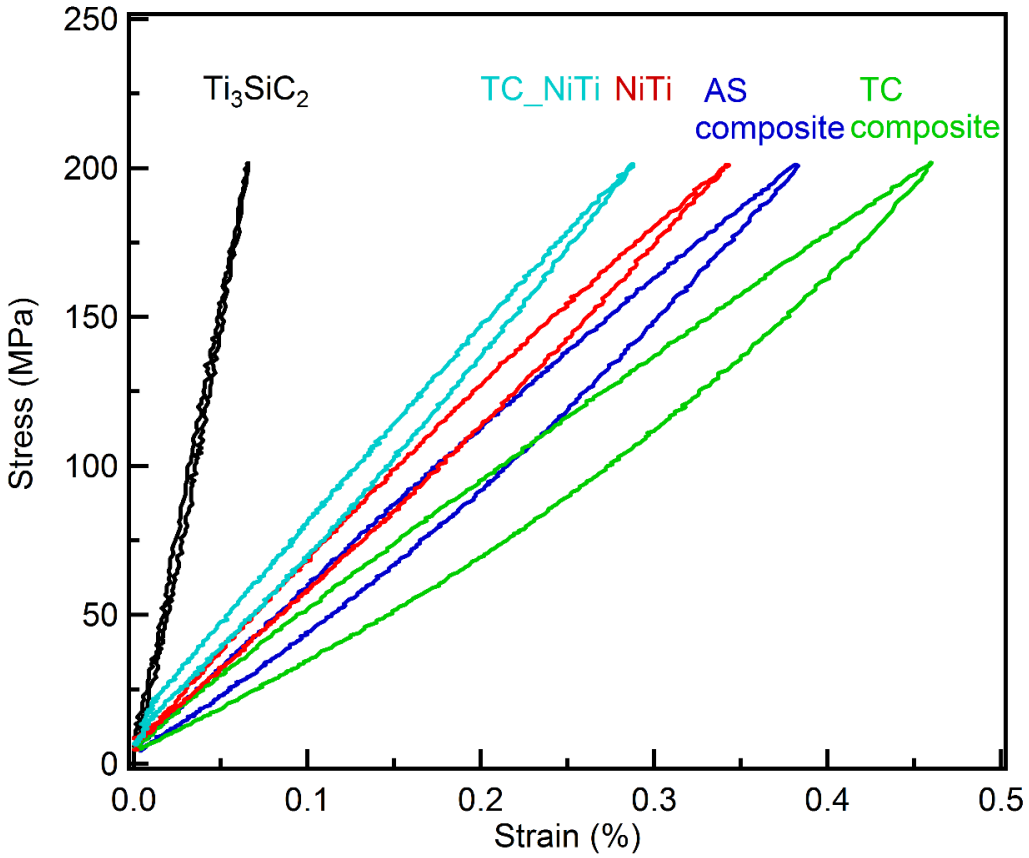

Figure 5.1 Engineering stress-strain loops at 200 MPa for each material, namely pure NiTi, fully dense pure Ti_3SiC_2, thermo-mechanically cycled (TC) pure NiTi, as-sintered (AS) and TC SPS # 3 composites

NiTi/Ti_3SiC_2 SPS # 3 composites, a linear dependence is observed where all the straight lines have an R^2 value > 0.96 except for pure NiTi which has a value of 0.91. As shown in Figure 5.3, the highest dissipation, (W_d), is observed at all stress values for the TC composite followed by AS composite. Pure NiTi and TC pure NiTi have similar dissipation and W_d is the lowest for pure Ti_3SiC_2. At 200 MPa applied stress,

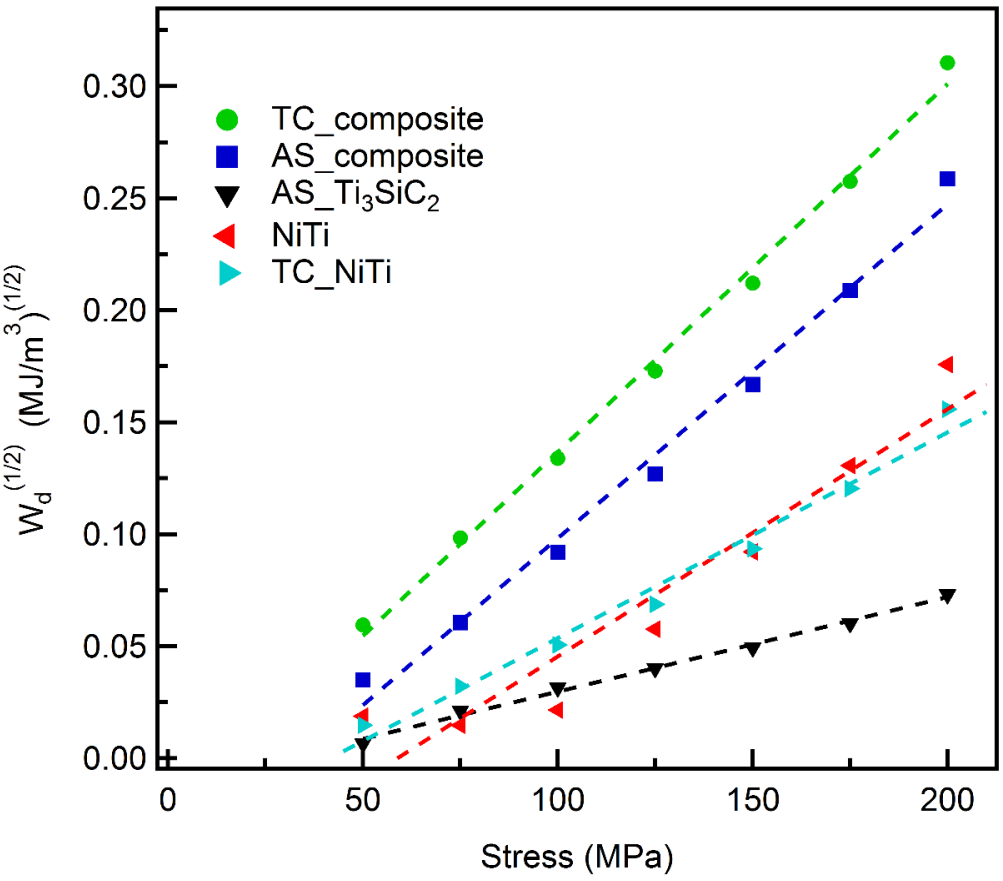

Figure 5.2 Energy dissipation per unit volume per loading-unloading cycle (W_d) as a function of maximum applied stress squared for each material, namely pure NiTi, fully dense pure Ti_3SiC_2, thermo-mechanically cycled (TC) pure NiTi, as-sintered (AS) and TC SPS # 3

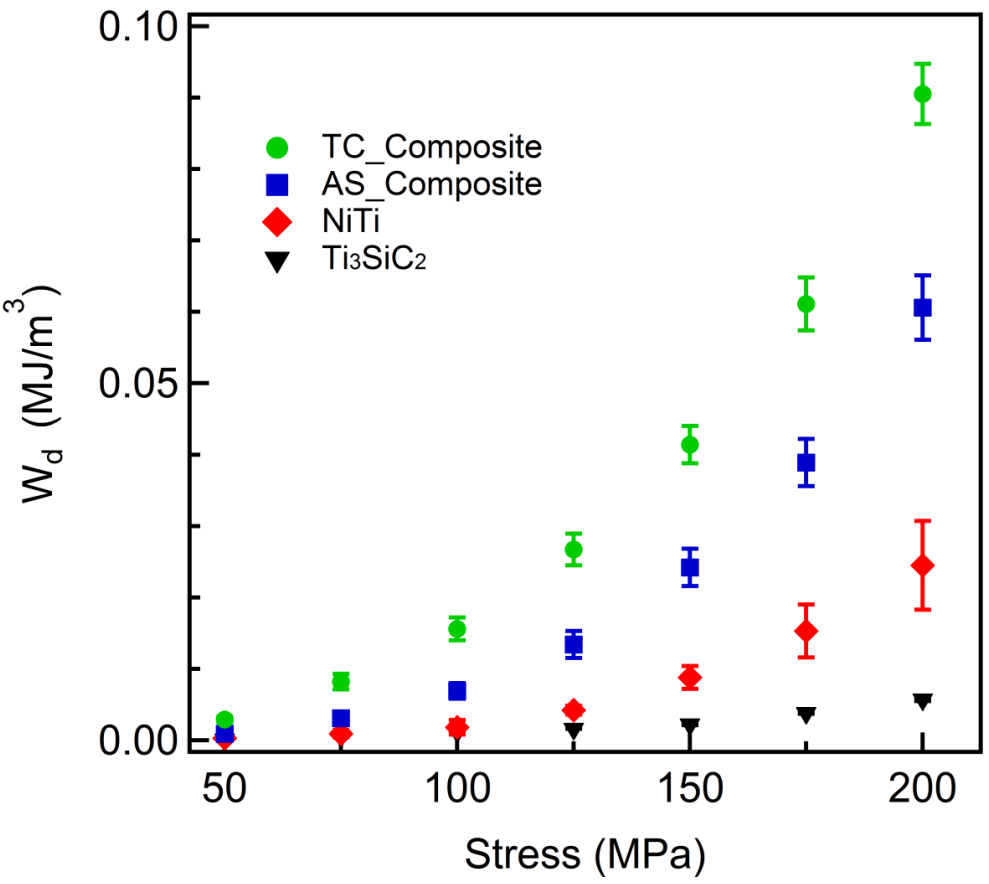

Figure 5.3 Energy dissipation per unit volume per loading-unloading cycle (W_d) as a function of maximum applied stress for pure NiTi, fully dense pure Ti_3SiC_2, as-sintered (AS) and thermo-mechanically cycled (TC) composite

W_d in the TC composite is eighteen times larger than that of fine grain (FG) fully dense pure Ti_3SiC_2 and three times larger than pure NiTi. In AS composite, W_d is thirteen times larger than that of FG fully dense pure Ti_3SiC_2 and two times larger than that observed in pure NiTi. Among all the works on the metal/MAX composites in the literature, energy dissipation has only been reported in Mg/Ti_3SiC_2 composites at stresses below 200 MPa [153]. Both the TC and AS composites of the present study

show higher W_d than Mg/Ti_3SiC_2 composites at similar stresses. W_d in the TC composites is higher by an order of magnitude when compared to Mg/Ti_3SiC_2 composites at similar stresses.

5.2 Damping in As-Sintered (AS) Composites

The major contributing factors for the high energy dissipation observed in the SPS # 3 composite are the damping contributions from pure Ti_3SiC_2, pure NiTi away from the interface, and in regions of NiTi closer to the interface between NiTi and Ti_3SiC_2 phases, and the presence of porosity. MAX phases in general and Ti_3SiC_2 in particular are known to be good damping materials. As stated earlier, Ti_3SiC_2 dissipates 25% (0.7 MJ/m^3) of the mechanical energy while being compressed to 1 GPa stress at room temperature [4]. One of the possible mechanisms for the high energy dissipation in the MAX phases is due to the reversible formation and annihilation of incipient kink bands (IKBs) during loading-unloading cycles [4]. As Ti_3SiC_2 is the stiffer phase in the SPS # 3 composite, it carries most of the stress. Thus, the stress experienced by Ti_3SiC_2 is higher than the applied external stress, which leads to higher damping contribution of the Ti_3SiC_2 phase to the overall damping of the composite.

In addition, SMAs are also known to be high damping materials in both, austenite and martensite state. In the current study, all the mechanical cycling experiments aimed at measuring energy dissipation are performed at room temperature, at which equiatomic NiTi is in martensite state. The damping in martensite is due to hysteretic movement of twin boundaries and interfaces between the different variants,

the latter found to be a necessary requirement for high damping [165]. Moreover, microstructural features in martensite plates such as dislocations, stacking faults and other defects also contribute to high damping of SMAs [35]. Although the stress experienced by NiTi is lower than the externally applied stress to the composite, twinning has been experimentally observed using neutron diffraction in pure NiTi at stresses as low as 33 MPa [166].

Another important contributing factor for damping in the composites which is not present in pure bulk NiTi or Ti_3SiC_2 phases should be the damping caused by the twins and twin boundaries possibly formed due to the residual stress relaxation occurring in the interface between the NiTi and Ti_3SiC_2 phases. On cooling the composites from sintering temperatures, elastic and thermal mismatch caused by the differences in the elastic modulus and thermal expansion coefficients respectively, between Ti_3SiC_2 phase and NiTi should lead to the generation of residual stresses in the interface. Additional mismatch stresses are generated between NiTi and Ti_3SiC_2 phases due to volumetric and shape changes upon transformation in NiTi. These stresses may get relaxed by the formation of relaxation twins in the NiTi regions near the interface. Several studies on metal matrix composites (MMCs) reinforced with ceramic fibers, suggest that interface thermal stresses promote the formation of highly mobile dislocation zones in the metal matrix near the interfaces [167-168]. In NiTi, stress for twin formation is lower than stress for formation of dislocations. Hence, in the SPS # 3 composite, more relaxation twins are expected to form thereby contributing to the overall energy dissipation of the composite. For multiphase materials such as MMCs reinforced with ceramic fibers, a

model has been developed and supported with experimental results, which divides the contributions to overall damping into three parts: the fibers, the matrix far from the fibers and the high dislocation density zones, also called microplastic zones, around the fibers [169]. This aforementioned model for multiphase materials substantiates the argument that interface region in the SPS # 3 composite is a contributing factor to its overall damping. As the NiTi and Ti_3SiC_2 phases are present in equal volume fractions in the SPS # 3 composite, contribution due to interface twinning towards overall damping cannot be neglected.

It is quite well known that the higher the percentage of the porosity in the MAX phase, the higher the energy dissipation (W_d) gets as compared to a fully dense MAX phase [170, 171]. Porosity reduces the threshold stress for kink band formation which is an effect of reduction in shear moduli [171]. It has been shown that 18 % porosity in FG pure Ti_3SiC_2 leads to an increase in the energy dissipation (W_d) by a factor of 6 at a stress of 200 MPa when compared to a FG fully dense Ti_3SiC_2 [171]. In the current study, the SPS # 3 composite has 16.4 % overall porosity mostly due to incomplete sintering of MAX phase. Thus, it is only fair to argue that 16.4 % porosity in the SPS # 3 composite enhances the dissipation capacity several folds and thereby significantly increases the overall damping capacity of the composite.

In summary, four factors that result in an increase in the damping observed in the as-sintered NiTi/Ti_3SiC_2 composite as compared to pure individual constituents are: first, higher stresses experienced by the Ti_3SiC_2 phase due to difference in elastic moduli of the NiTi and Ti_3SiC_2 phases present in the composite which lead to higher damping in

the Ti_3SiC_2 phase; second, damping due to hysteretic movement of twins and twin boundaries in NiTi phase; third, newly formed twins and twin boundaries in the NiTi near the interface region due to relaxation of residual stresses in the composite; and lastly the presence of porosity in the composite. As of now, it is difficult to comment on the quantitative contributions of each of the four possible factors to the overall damping of the composite.

5.3 Damping in Thermo-mechanically Cycled (TC) Composites

As stated earlier, energy dissipation of the martensitic phase in SMAs is strongly related to the mobility of twin interfaces and other structural defects inherent to the martensitic phase such as vacancies, dislocations and grain boundaries [172]. These defects in the microstructure are significantly influenced by the thermo-mechanical treatment which also indirectly affects the overall energy dissipation of the material. Thermo-mechanical cycling leads to the generation of internal stresses, as observed in the form of TWSME in the SPS # 3 composite. This internal stress in turn leads to the reduction in the stress required for detwinning. Hence, when an external stress of, for example, 200 MPa is applied, more twin boundaries move in TC than AS composites leading to higher energy dissipation, W_d, in TC than AS composites. As previously stated, irrecoverable strain in the SPS # 3 composite is due to the generation of dislocations in the bulk NiTi and in the regions near the interface along with irrecoverable strain in Ti_3SiC_2 phase. Dislocations, twins and other defects near the interface region created due to thermo-mechanical cycling may affect the overall energy

dissipation capability of the composite. It has been shown that interaction of dislocations with other lattice defects could influence the energy dissipation capacity [173]. Also, several studies observed a correlation between the damping capacity and generation and motion of dislocations around the interfaces between multiphase materials [169, 174]. The nature of interaction of these defects with Ti_3SiC_2 phase which itself shows reversible kinking behavior while loading is not clear at this time. In the TC SPS # 3 composite, various mechanisms of damping, namely hysteretic movement of interfaces and twin boundaries in NiTi phase, incipient kink band formation in Ti_3SiC_2 phase and dislocation damping in the interface region are operative simultaneously. The dislocations and other defects formed due to thermo-mechanical cycling coupled together with the reasons listed in the as-sintered NiTi/Ti_3SiC_2 composite result in an increased damping in the composite as compared to pure constituents.

To the best of author's knowledge, both the TC and AS NiTi/Ti_3SiC_2 composites show higher energy dissipation, W_d, than all the metal/MAX composites reported in the literature to date, up to 200 MPa stress. Also, W_d in TC composites is higher by almost an order of magnitude when compared to Mg/Ti_3SiC_2 composites at similar stresses [153]. In summary, the novel SMA / MAX phase composites show promising properties as a high damping material at low stresses and the present work highlights the ability to enhance the performance with suitable thermo-mechanical loading paths.

5.4 Summary

- All the composites show fully reversible, closed, non-linear hysteretic stress-strain loops up to the stress of 200 MPa. The as-sintered (AS) NiTi/Ti_3SiC_2 composite shows higher energy dissipation than its individual components. At 200 MPa applied stress, the energy dissipation measured in the AS composite is thirteen times larger than fine grain fully dense pure Ti_3SiC_2 and two times larger than pure NiTi. This increase is due to the following reasons: First, higher stress experienced by the Ti_3SiC_2 phase due to difference in elastic moduli of NiTi and Ti_3SiC_2 phases which lead to higher damping in the Ti_3SiC_2 phase; second, damping due to hysteretic movement of twins and twin boundaries in NiTi phase; third, newly formed twins and twin boundaries in the NiTi phase near the interface region due to relaxation of residual stresses in the composite; and lastly, the presence of porosity.
- The highest energy dissipation, (W_d), is observed at all stress values for the thermo-mechanically cycled (TC) composite followed by the as-sintered (AS) composite. At 200 MPa, the energy dissipation, W_d, in the TC composite is eighteen times larger than fine grain fully dense pure Ti_3SiC_2 and three times larger than pure NiTi. The superb energy dissipation capacity of the composite is attributed to the dislocations and other defects formed due to thermo-mechanical cycling leading to more twin boundary motion in addition to the reasons listed for the AS composite. At this time, this hypothesis is unsubstantiated with experimental results and the need for specially designed experiments and finite element modeling cannot be overemphasized.

6. JOINING AND MICROSTRUCTURAL CHARACTERIZATION OF BILAYER*

6.1 Microstructure of the Bonded NiTi-Ti_3SiC_2 Interface

Figure 6.1 shows the cross sectional views of the microstructure of NiTi-Ti_3SiC_2 interface after diffusion bonding at 800, 900 and 1000°C for 1, 5 and 10 hours. All the microstructural images are shown on the X-Y plot where the X-axis is the bonding time and the Y-axis the bonding temperature. In all the micrographs in Figure 6.1, the lighter region on the left is equiatomic NiTi and the dark grey region on the right is Ti_3SiC_2. In between the two, the interface is marked with vertical dotted red lines to denote the start and end of the reaction layer in the interface. The numbers on each of the image are the lengths of the horizontal black lines which represents the average interface thickness. Evolution of the interface thickness with time at different temperatures along with the kinetics of the reaction will be described later in section 6.3. As it can be seen in Figure 6.1, bonding has been observed for all conditions except at 800°C for 1 hour. In our previous study, NiTi and Ti_3SiC_2 have been joined in the temperature range of 1100-1200°C using pressureless liquid phase assisted diffusion bonding [87], however, no bonding was observed at 1000°C, most likely due to poor contact between the two surfaces in the absence of any preloading stress.

---

*Part of this section is reprinted with permission from "Interfacial study of NiTi–Ti_3SiC_2 solid state diffusion bonded joints" by Kothalkar et. al., Materials Science and Engineering: A, 622, 168-177, [2015] by Elsevier

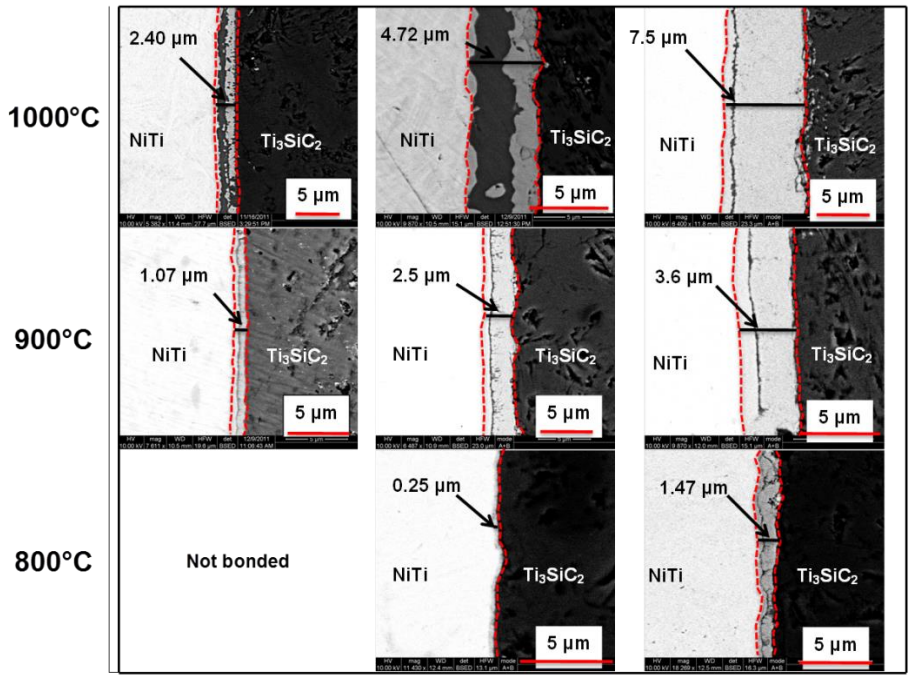

Figure 6.1 Microstructural evolution of the NiTi-Ti_3SiC_2 interface with time and temperature obtained by SEM. Red (dotted) line indicates the start and end of the interface region between NiTi and Ti_3SiC_2. The numbers shown in each of the micrographs are the thicknesses of the interface as indicated by the black horizontal lines on each image in the interface region.

As it can be seen in Figures 6.1 and 6.2, at each bonding condition, formation of three distinct layers in the interface is observed. One light grey layer adjacent to NiTi and the other adjacent to Ti_3SiC_2. These two light grey layers are separated by a third dark grey layer in between. To determine theses reaction phases in the interface, EPMA was used. Figure 6.2 shows the selected, but typical, back-scattered electron micrographs of the interface for the bonding condition of 1000°C, 5 hours.

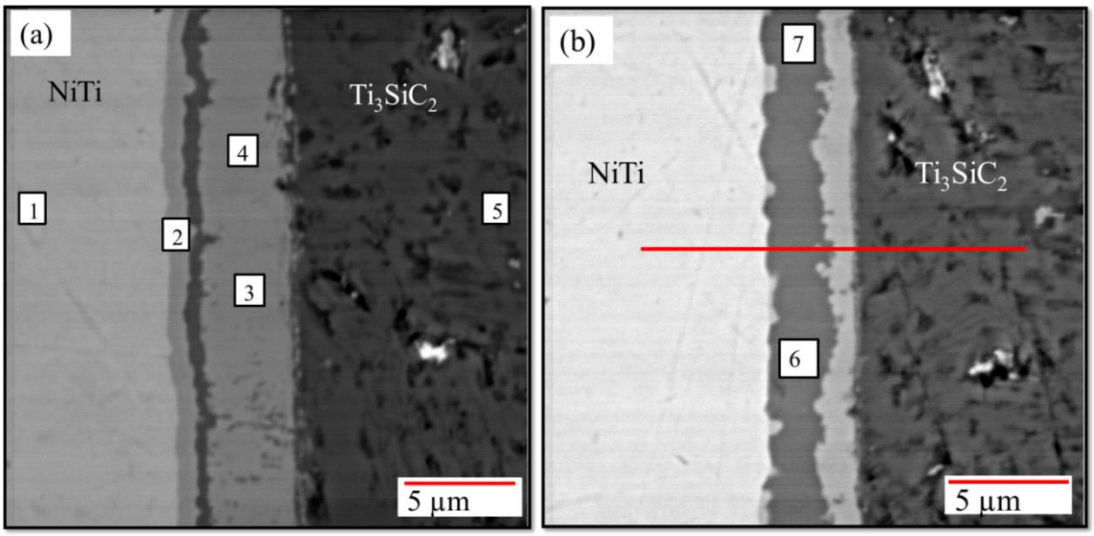

Figure 6.2 Back-scattered electron images of the NiTi-Ti_3SiC_2 interface for the bonding condition of 1000°C, 5 hours. Points 1-5 in (a) and 6-7 on (b) show the location where quantitative spot spectra are obtained by electron microprobe for determining the composition of different reaction phases formed in the interface. Table 6.1 lists the composition of all the points shown in this figure. Points 1 and 5 are 10 microns away from the interface in the NiTi and Ti_3SiC_2 regions, respectively. The horizontal red line in Figure 6.2 (b) indicates the location of the line scan shown in Figure 6.4.

Points 1-5 in Figure 6.2 (a) and 6-7 on Figure 6.2 (b) show the location where quantitative spot spectra are obtained by EPMA. Table 6.1 lists the atomic percentages of Si, Ni, Ti and C at the locations marked in Figure 6.2. The percentage of C was calculated by taking the difference between the total (100%) and the sum of the measured atomic percentages of Si, Ni and Ti. Point 1 corresponds to equiatomic NiTi as ratio of Ni to Ti is almost 1:1 and point 5 to Ti_3SiC_2 as the ratio of Ti to Si is 3:1. Points

3 and 4 are on the same light grey phase adjacent to Ti_3SiC_2 and their compositions suggest it to be NiTiSi phase. Points 6 and 7 in Figure 6.2 (b) are on the dark grey phase

Table 6.1. Atomic percentages of Si, Ni and Ti from electron microprobe spot analysis of the different points marked in Figure 2 and also the probable phases for each location in the interface. BDL means below detection limit, which was 0.2 % for Ni.

Location (Figure 6.2)	**Atomic %**				**Probable phase**
	Si	Ni	Ti	C	
1	0.2	49.2	50.6	0	NiTi
2	6.3	35.4	58.3	0	Ti_2Ni
3	31.6	29.8	33.5	5.1	NiTiSi
4	31.2	29.5	33.5	5.8	NiTiSi
5	16.8	BDL	51.8	31.4	Ti_3SiC_2
6	36.0	1.2	62.8	0	Ti_5Si_3
7	35.4	1.8	62.8	0	Ti_5Si_3

which separates the two light grey phases in the interface. The compositions of these points suggest the phase to be Ti_5Si_3 with the ratio of Ti to Si being close to 5:3. Low Ni (around 1%) is also observed due to scattering from adjacent Ni containing phases. Composition of point 2 in Figure 6.2 (a), which is located in light grey phase adjacent to NiTi, is slightly off from that of Ti_2Ni phase. This is due to the fact that its thickness is

less than 1 μm and the beam from the microprobe scatters more than a micron during quantitative analysis, thereby detecting extra Ni from the adjacent NiTi phase. All the probable phases (Ti_2Ni, Ti_5Si_3 and NiTiSi) in the interface are also present in the ternary phase diagrams of Ni, Ti and Si at 900 [175] and 1000°C [176], as shown with a schematic in Figure 6.3 following the phase diagram at 1000°C [176]. All the three phases observed in the interface form continuous layers as shown in Figure 6.2 (a) whereas in Figure 6.2 (b), the light grey phase (Ti_2Ni) closer to NiTi is discontinuous. Both the images are obtained for the same condition of 1000°C, 5 hours. Also the micrograph shown in Figure 6.1 for 1000°C, 5 hours is similar to the one in Figure 6.2 (b). The most probable reason is the amount of local pressure experienced in these locations in the diffusion couple is different possibly due to surface asperities.

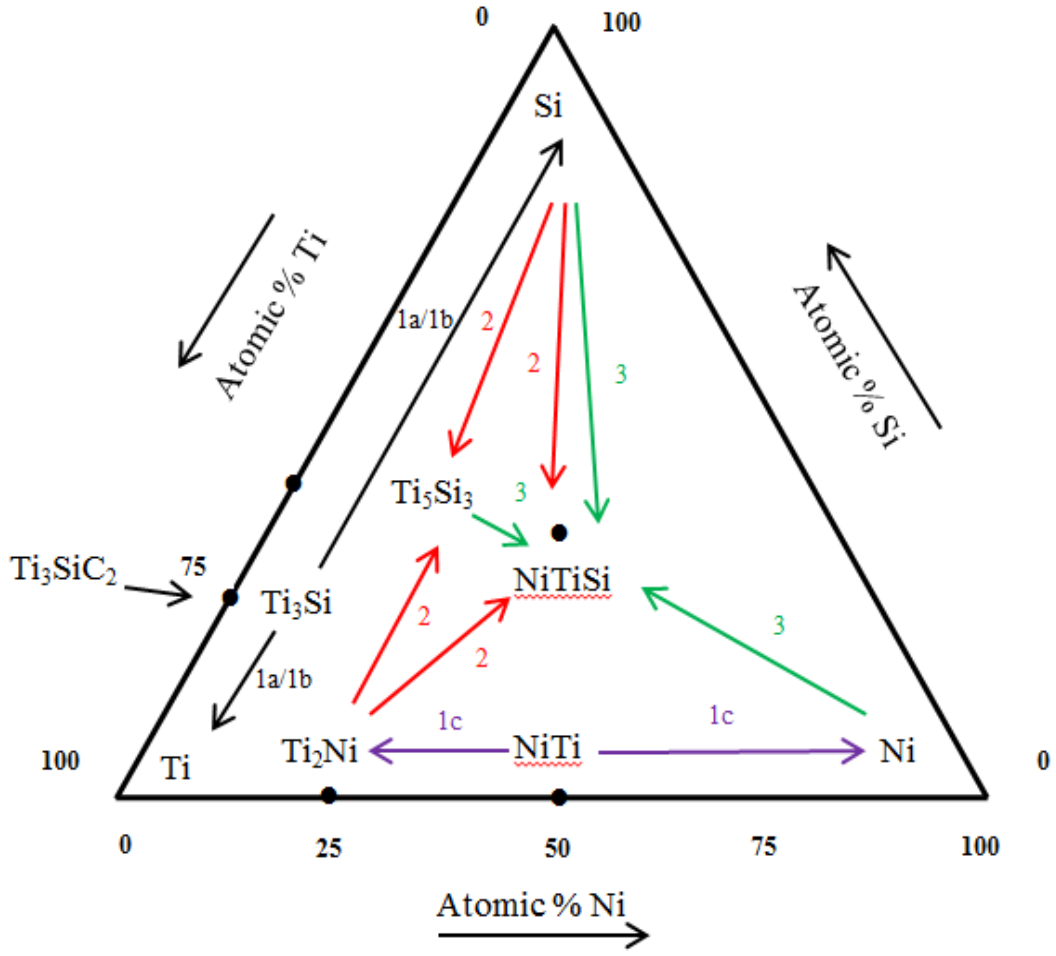

Figure 6.3 Schematic of the Ni-Ti-Si ternary phase diagram at 1000°C following [176], showing the phases observed at interface after the 1000°C, 10 hours bonding. The numbers labeled 1 (a, b, c, red), 2(purple) and 3 (green) on the schematic correspond to the equations 9-11 shown in the text.

Elemental distribution of Ni, Si and Ti across the interface determined using the EDS line scan analysis for the bonding condition of 1000°C, 5 hours is shown in Figure 6.4. The horizontal line (red) marked in the Figure 6.2 (b) shows the location of the line scan across the interface. For each element, the normalized intensity is obtained by

dividing the intensity at each point with the maximum intensity. Three regions, NiTi, interface and Ti_3SiC_2 are clearly marked on the line scan. Very low intensities of Si and Ni are observed in NiTi and Ti_3SiC_2 regions respectively suggesting minor diffusion of Si and Ni away from the interface. At the NiTi side of the interface region, the intensity of Ni first drops to near zero and then locally increases before going down again. The region without Ni in the interface corresponds to Ti_5Si_3 phase where only Ti and Si elements are detected. When the Ni intensity reaches a local maximum before dropping to near zero, Ti and Si elements are also detected and this region in the interface adjacent to Ti_3SiC_2 corresponds the NiTiSi phase. Thus, the line scan is consistent with the results shown in Table 6.1 and Figure 6.2 (b).

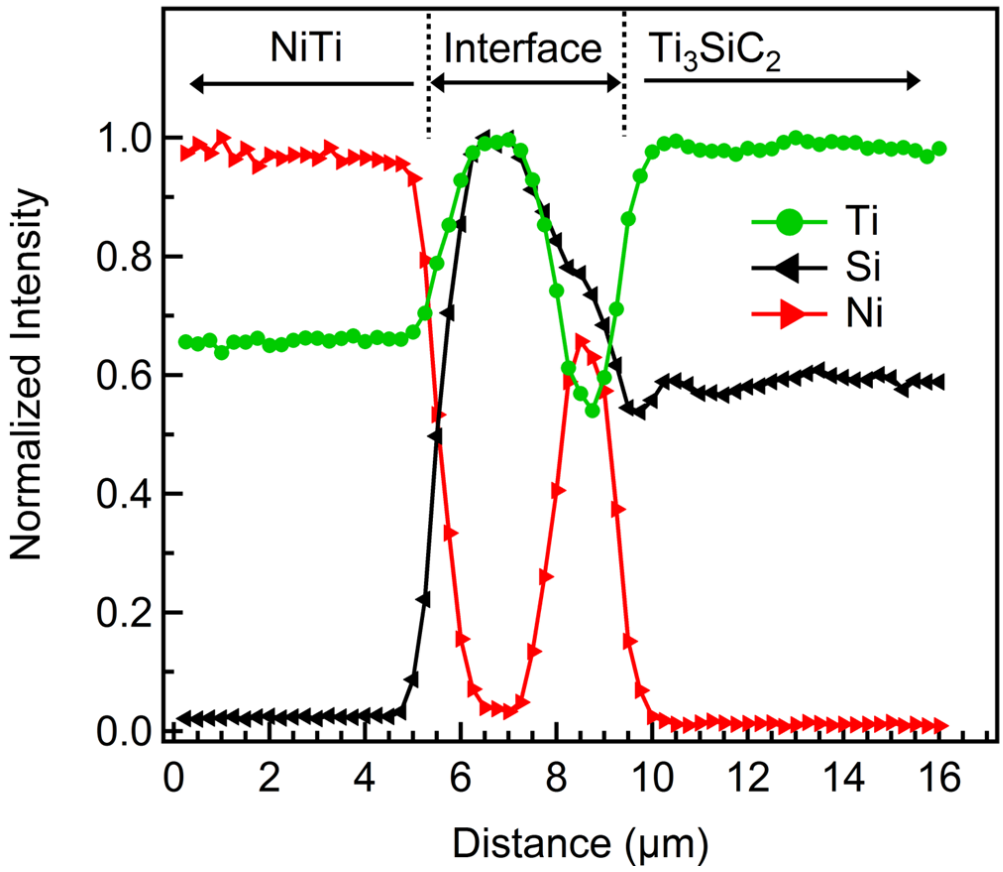

Figure 6.4 Line scan for Ni (red), Si (black) and Ti (green) across the NiTi-Ti_3SiC_2 interface for the bonding condition of 1000°C, 5 hours indicated on Figure 2 (b) with a horizontal (red) line.

6.2 Electron Backscatter Diffraction (EBSD) Observations and Reaction Mechanisms

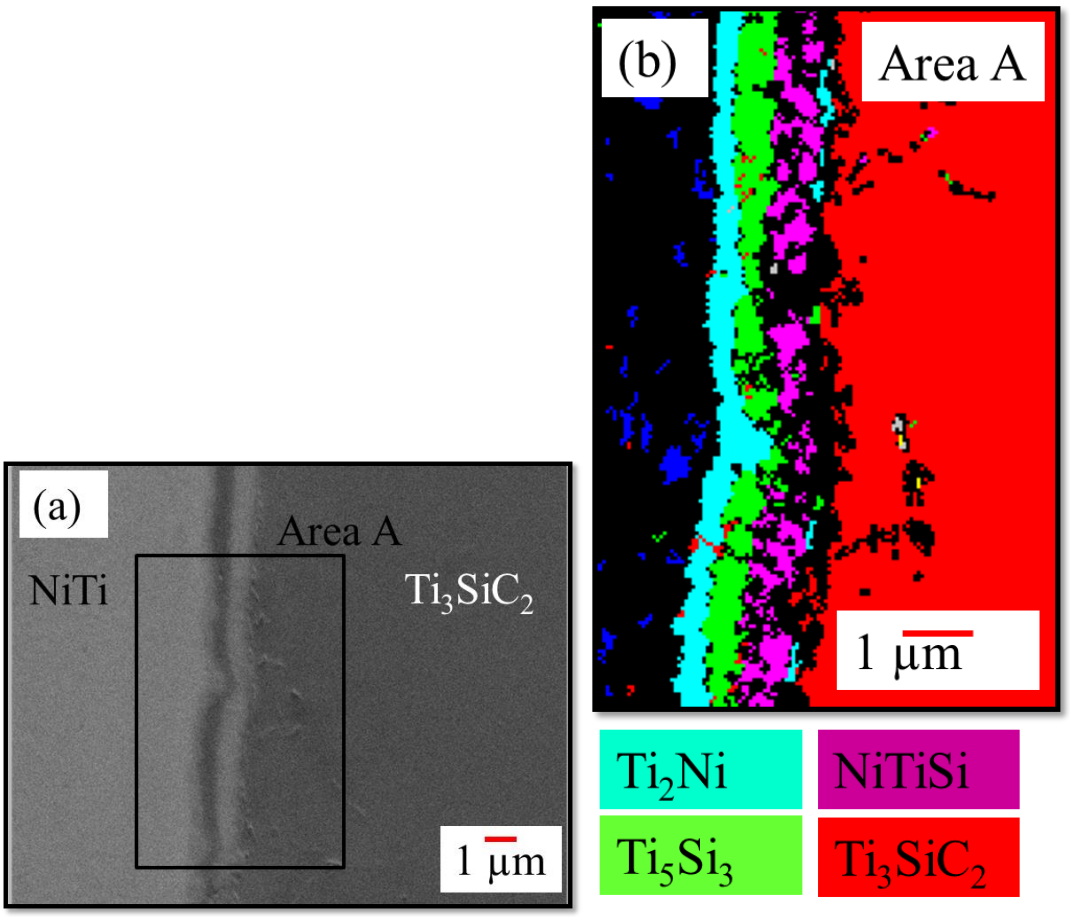

Figure 6.5 Images of the NiTi-Ti_3SiC_2 interface for the bonding condition of 900°C, 5 hours (a) BSE image, and (b) Electron backscattered diffraction (EBSD) phase map of the "Area A" marked in (a) showing the distribution of the reaction phases, NiTiSi (pink), Ti_5Si_3 (green) and Ti_2Ni (light blue) in the interface. The MAX phase is indicated in red and the blue areas are the NiTi phase that could be indexed. The black areas in the map represent areas where diffraction patterns could not be obtained due to sample preparation issues or resolution limit of the technique (this second explanation is especially true for the NiTi phase that its martensite phase consists of very thin needles).

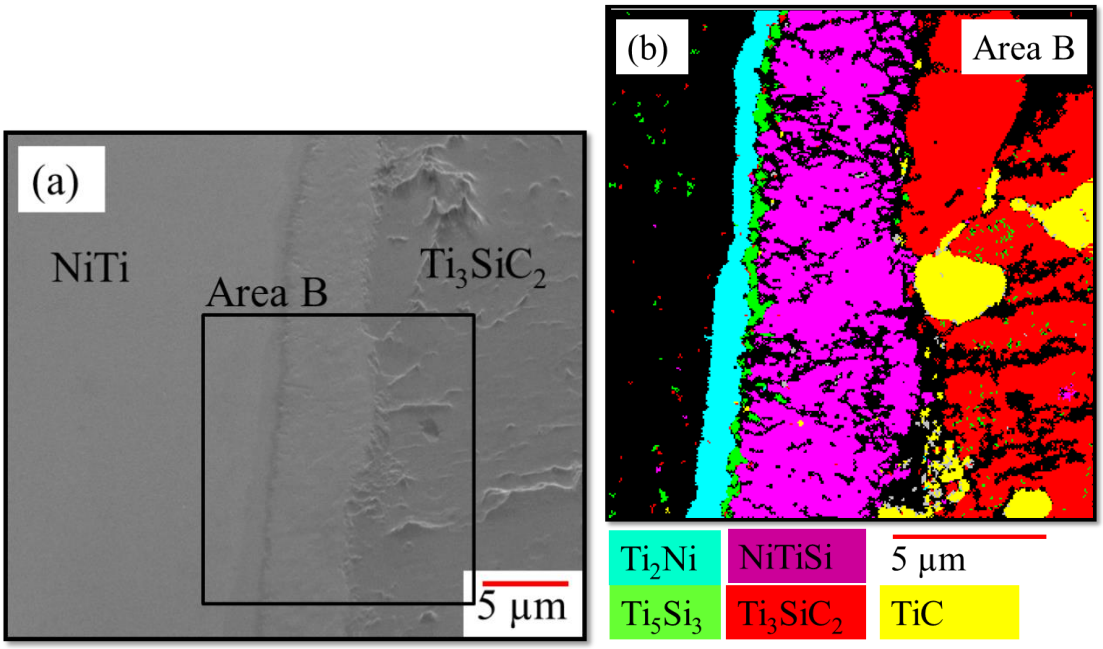

Figure 6.6 Images of the NiTi-Ti_3SiC_2 interface for the bonding condition of 1000°C, 10 hours (a) BSE image, and (b) Electron backscattered diffraction (EBSD) phase map of the area B marked in (a) showing the distribution of the reaction phases, Ti_2Ni (light blue),), Ti_5Si_3 (green) and NiTiSi (pink) and in the interface. Also shown are TiC (yellow) and Ti_3SiC_2 (red).

Figure 6.5 and Figure 6.6 show the distribution of different phases in the NiTi-Ti_3SiC_2 interface for the conditions of 900°C, 5 hours and 1000°C, 10 hours, respectively, obtained using EBSD analysis. EBSD analysis confirmed and substantiated the formation of Ti_2Ni, Ti_5Si_3 and NiTiSi reaction phases in the interface, earlier inferred from the results of quantitative analysis and Ni-Ti-Si ternary phase diagram [176], schematically shown in Figure 6.3. Figure 6.5 (a) shows the backscattered electron image of the NiTi-Ti_3SiC_2 interface formed at 900°C, 5 hours, marked with area A from where the phase map shown in Figure 6.5 (b) is obtained using EBSD. Clearly, the interface has a structure of NiTi / Ti_2Ni / Ti_5Si_3 / NiTiSi / Ti_3SiC_2. A similar interface

structure is observed in Figure 6.6 wherein all the reaction phases form continuous layers in the interface at 1000°C, 10 hours. TiC phases are detected in the Ti_3SiC_2 phase and also along the boundary between NiTiSi and Ti_3SiC_2. Small amount of TiC is expected to form as a result of Si de-intercalation and as Ti_3SiC_2 phase usually contains few percent impurities in the form of TiC. From the combined results of EBSD, quantitative EPMA analysis, micrographs of the microstructures of the NiTi-Ti_3SiC_2 interface at various bonding conditions, and the ternary phase diagram, a reaction mechanism has been proposed as described in the equations 9-11

$$Ti_3SiC_2 \rightarrow x\ Si + Ti_3Si_{1-x}C_2 \quad (9a)$$

$$4\ Ti_3SiC_2 \rightarrow Si + Ti_5Si_3C_{y} + 7\ TiC_{1-x} \quad \text{where } y = 1 + 7x \quad (9b)$$

$$2\ NiTi \rightarrow Ni + Ti_2Ni \quad (9c)$$

$$5\ Ti_2Ni + 8\ Si \rightarrow Ti_5Si_3 + 5\ NiTiSi \quad (10)$$

$$Ti_5Si_3 + 5\ Ni + 2\ Si \rightarrow 5\ NiTiSi \quad (11)$$

As “A” element is the most weakly bonded element in the MAX phase [86], the decomposition of Ti_3SiC_2 by de-intercalation of Si may lead to the formation of non-stoichiometric $Ti_3Si_{1-x}C_2$ as per equation 9a, whereas formation of $Ti_5Si_3C_y$ and non-stoichiometric TiC_{1-x} phase may occur on further decomposition of Ti_3SiC_2, where $y = 1 + 7x$, according to equation 9b. The reaction (equation 9b) has been previously observed when bulk NiTi and Ti_3SiC_2 are diffusion bonded at 1100°C [87]. Various researchers have studied the reactions and stability of MAX phases in the presence of metals and

alloys at elevated temperatures [87-95]. The study of reactions between Ti and Ti_3SiC_2 in the temperature range of 1000-1300°C found out that de-intercalation of Si is one of the ways that leads to the decomposition of Ti_3SiC_2. In this study, on the other side of the interface, Ni from NiTi diffuses out leaving behind a Ti-rich Ti_2Ni phase according to equation 9c. Study on the microstructure and diffusion bonding of Ni - Ti_3SiC_2 joints found out that diffusion of Ni towards the reaction zone is the main controlling step in the bonding process [91]. Here, equations 9a, 9b and 9c occur simultaneously followed by the combination of Si from Ti_3SiC_2 with the Ti-rich Ti_2Ni phase to form Ti_5Si_3 and NiTiSi phase according to equation 10. Ni coming out of NiTi as per equation 9c gets consumed by reacting with Ti_5Si_3 formed as per equation 10, and Si diffusing through NiTiSi phase, leading to the formation of more NiTiSi phase according to equation 11. On further increasing the time, more Ti_2Ni phase is formed which gets consumed in forming Ti_5Si_3 and NiTiSi phase. However, Ti_5Si_3 also gets consumed by Ni and Si to form NiTiSi phase. Thus, NiTiSi phase could be imagined to moving towards NiTi formed by consuming Ti_2Ni phase and Ti_5Si_3 phase. Thus, arguably the most probable location of the original interface would lie between the current Ti_3SiC_2 and NiTiSi phase. At 1000°C, 10 hours, TiC phase is also observed due to possible complete loss of Si from Ti_3SiC_2 phase at higher temperatures and longer time compared to other bonding conditions. The presence of intermetallic phases such as Ti_5Si_3, Ti_2Ni and NiTiSi were also observed in the reaction layer formed between NiTi and Ti_3SiC_2 composites sintered at 960°C, for 8 minutes under 100 MPa uniaxial pressure using spark plasma sintering (SPS) technique [159].

6.3 Bonding Kinetics

From the results of quantitative analysis using EPMA and EBSD, the presence of Ti_2Ni, Ti_5Si_3 and NiTiSi reaction phases in the NiTi-Ti_3SiC_2 interface is confirmed. The total thickness of the reaction layer which is a combination of all the three sublayers (Ti_2Ni, Ti_5Si_3 and NiTiSi rich sublayers) is measured at each bonding temperature and time using backscattered electron imaging. Total reaction layer thickness and standard deviations are calculated from an average of at least 15 measurements for each bonding condition. Figure 6.7 (a) shows the plot of total reaction layer thickness versus square root of the bonding time at 800, 900 and 1000°C. At each temperature, as the holding time is increased, the thickness of the total reaction layer also increases, while for the same holding time, the thickness increases as the holding temperature is increased. Good linear relationships are observed in Figure 6.7 (a), for all the temperatures wherein all the best fit lines have an R^2 value > 0.98 indicating that the growth of the reaction layer follows the parabolic kinetic law, i.e. $d^2=2K_p.t$ where d is the total thickness of the reaction layer, K_p is the parabolic rate constant and t is time. The total reaction layer thicknesses vary from less than a micron at 800°C, 5 hours to 7 microns at 1000°C, 10 hours bonding conditions. These layer thicknesses are an order of magnitude smaller when compared to the 45-55 microns reaction layers reported in the temperature range of 1100-1200°C between NiTi-Ti_3SiC_2 diffusion couples [87]. The difference lies in the mechanism of diffusion bonding, liquid state diffusion bonding above 1000°C [87] whereas solid state diffusion bonding below 1000°C obtained here. The presence of liquid phase also leads to increased reaction and higher number of reaction phases

present in the interface at 1100-1200°C [87] as compared to those obtained in this study below 1000°C.

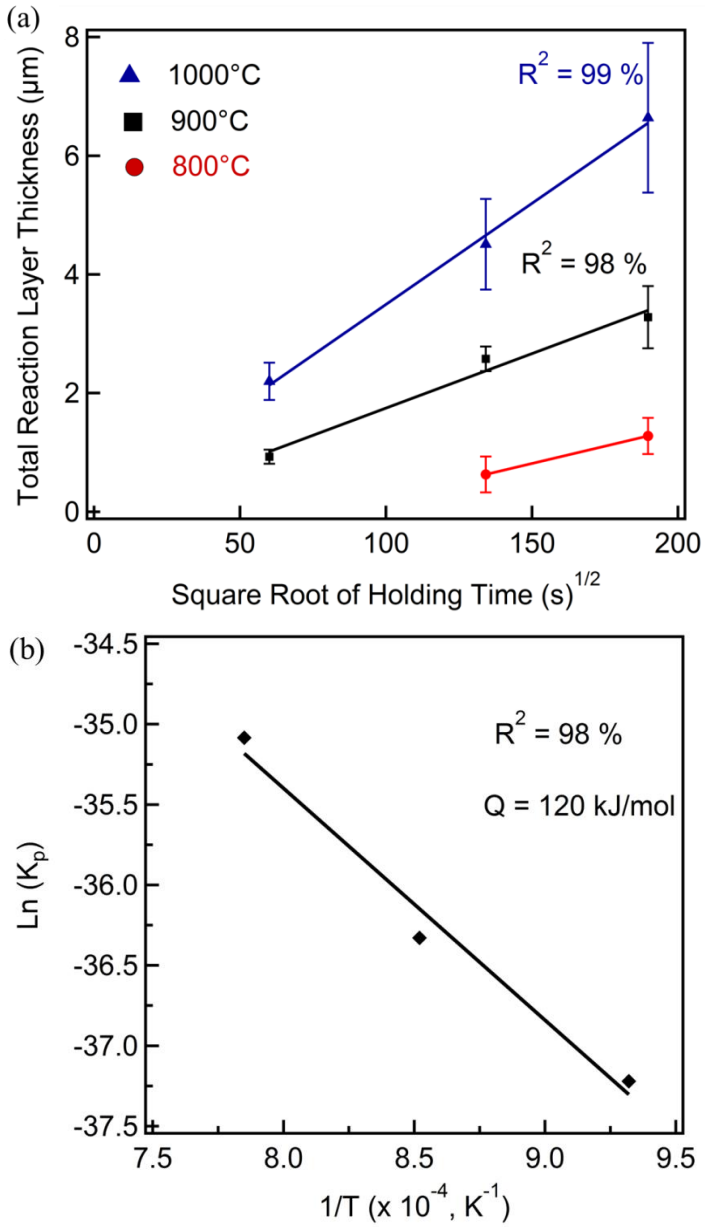

Figure 6.7 (a) Evolution of the total reaction layer thickness with the square root of holding time at different temperatures for the NiTi-Ti_3SiC_2 interface, and (b) Arrhenius plot of the parabolic rate constant versus the reciprocal of the absolute bonding temperature in the temperature range of 800-1000°C.

Parabolic rate constant is obtained for each bonding temperature from the slopes of the curves shown in Figure 6.7 (a). However, one needs to be careful while determining K_p from the slopes of the curves in Figure 6.7, as the calculated K_p is for a combination of reactions given in Eq. 1-3 and not for a single reaction. To obtain an approximate value for the activation energy of the overall bonding process, the K_p is plotted as a function of bonding temperature in the temperature range of 800-1000°C. Figure 6.7 (b) indicates a good linear relationship with an R^2 value = 0.98 between Ln (K_p) and the inverse of absolute temperature in accordance with the Arrhenius equation, $K_p = A \exp(- Q/RT)$ where A is the pre-exponent factor, Q is bonding activation energy, R is universal gas constant and T is absolute temperature. Using the slope and the intercept of the straight line in Figure 6.7 (b), the bonding activation energy (Q) and the pre-exponent factor (A) are found to be 120 kJ/mol and 4.34 x 10^{-11} m^2/s, respectively. Thus the Arrhenius equation for the NiTi-Ti_3SiC_2 interface in the temperature range of 800-1000°C can be written as

$$K_p = 4.34 \times 10^{-11} exp\left(\frac{-120000}{RT}\right) m^2/s \quad (12)$$

For the Ni-Ti_3SiC_2 diffusion couple, the activation energy in the temperature range of 800-1100°C is reported to be 118 kJ/mol [91], which is very close to the observed value of 120kJ/mol between NiTi and Ti_3SiC_2 in the temperature range of 800-

1000°C. This substantiates the argument that Ni diffuses out from NiTi forming another intermetallic compound, Ti_2Ni, and behaves in a similar fashion as in the case of pure Ni-Ti_3SiC_2 diffusion couple. Activation energy values for other metal-Ti_3SiC_2 systems have also been reported in the literature: 156 kJ/mol for Ti-6Al-4V - Ti_3SiC_2 in the range of 1200-1300°C [90] and 132 kJ/mol for Si-Ti_3SiC_2 in the range of 1200-1350°C [93]. Therefore the value obtained here falls within the range of previously measured values for similar material couples.

6.4 Summary

- Successful bonding between bulk NiTi and Ti_3SiC_2 components using solid state diffusion was realized in the temperature range of 800-1000°C for the times of 1 to 10 hours except at 800°C, 1 hour. Possibly, a sub-micron reaction layer forms at the interface at 800°C after 1 hour, but was unable to withstand the thermal residual stresses generated during cooling to the room temperature, leading to debonding.
- The reaction phases in the NiTi-Ti_3SiC_2 interface were characterized and the reaction mechanisms were proposed. Three uniform, distinct layers of Ti_2Ni, Ti_5Si_3, NiTiSi phases were formed between NiTi and Ti_3SiC_2, thus making the interfacial structure of the form NiTi / Ti_2Ni / Ti_5Si_3 / NiTiSi / Ti_3SiC_2.
- The overall reaction layer thickness grows as a square root of the time at each temperature indicating that mechanism of solid state diffusion in the interface follows a parabolic kinetic law. Diffusion of Si into NiTi from Ti_3SiC_2 and Ni

from NiTi into the reaction zone is responsible for the formation of reaction layers in the interface and thus the bonding at these conditions. However, the rate limiting step is diffusion of Si from Ti_3SiC_2.

7. MECHANICAL CHARACTERIZATION AND FRACTURE OF BILAYER*

Mechanical characterization of the NiTi-Ti_3SiC_2 interface was done using nano-indentation and Vickers micro hardness tests. Here, nano-indentation is used to perform quantitative analysis and obtain hardness and elastic modulus values for the interface. Owing to the small size of the interfaces formed at these conditions, Vickers micro-hardness test is used as a qualitative tool to investigate crack initiation/propagation, if any, in and around the interface regions. Both tests were performed at room temperature where the NiTi is completely in the martensite phase.

7.1 Nanoindentation

Figure 7.1 (a) and (b) show 3-dimensional plots of the hardness and elastic modulus, respectively, obtained using nano-indentation across the NiTi-Ti_3SiC_2 interface for the bonding condition of 1000°C, 5 hours. A grid of 100 indents (10 x 10) each separated by a distance of 3 μm is made across the interface as shown in Figure 7.1 (c). Indents lie partially in NiTi, interface and Ti_3SiC_2. Hardness and elastic modulus are obtained for each indent using the Oliver-Pharr method [177]. Hardness of the reaction zone in the interface is higher than that observed for both NiTi and Ti_3SiC_2. An average

*Part of this section is reprinted with permission from "Interfacial study of NiTi–Ti_3SiC_2 solid state diffusion bonded joints" by Kothalkar et. al., Materials Science and Engineering: A, 622, 168-177, [2015] by Elsevier

hardness of 17.55 ± 0.95 GPa is obtained for the interface as compared to 5.44 ± 0.73 GPa for NiTi and 11.86 ± 1.80 GPa for Ti_3SiC_2. Elastic modulus of the reaction zone is higher than NiTi and close to that of Ti_3SiC_2. An average elastic modului of 278.68 ± 10.02 GPa is obtained for the interface as compared to 91.62 ± 11.16 GPa for NiTi and 263.21 ± 31.89 GPa for Ti_3SiC_2. Elastic moduli obtained for pure components are similar to the previously reported literature values for martensitic NiTi [166] and Ti_3SiC_2 [178, 179] using nano-indentation. Most of the indents within the interface lie in the NiTiSi phase which is responsible for the increased hardness as compared to the individual components.

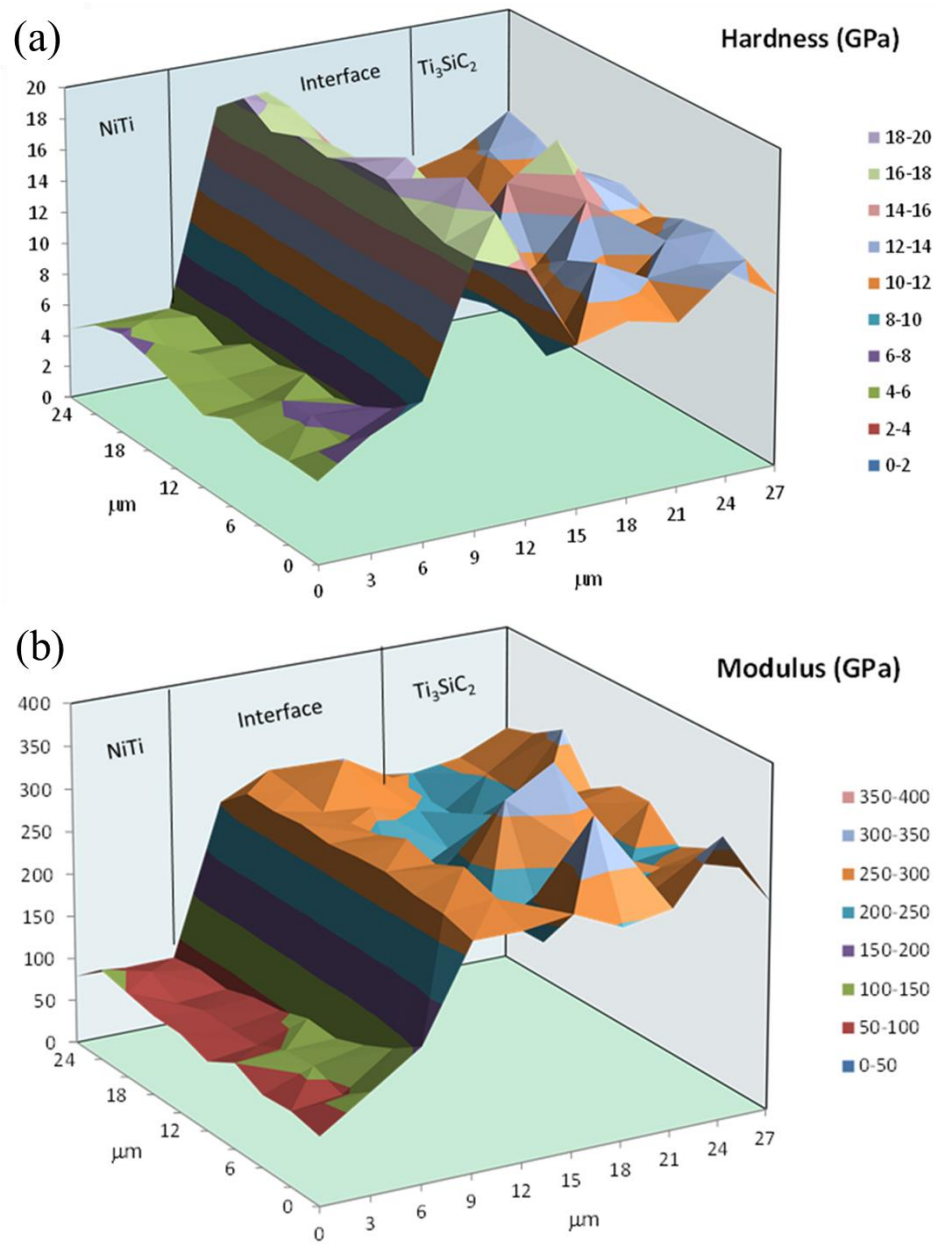

Figure 7.1 A 3-dimensional plot of the (a) hardness in GPa and (b) elastic modulus in GPa, obtained using nano-indentation across the NiTi-Ti_3SiC_2 interface for the bonding condition of 1000°C, 5 hours. (c) BSE image of the locations of the indents where the plots in (a) and (b) were generated and (d) high magnification BSE image showing indents in different reaction phases.

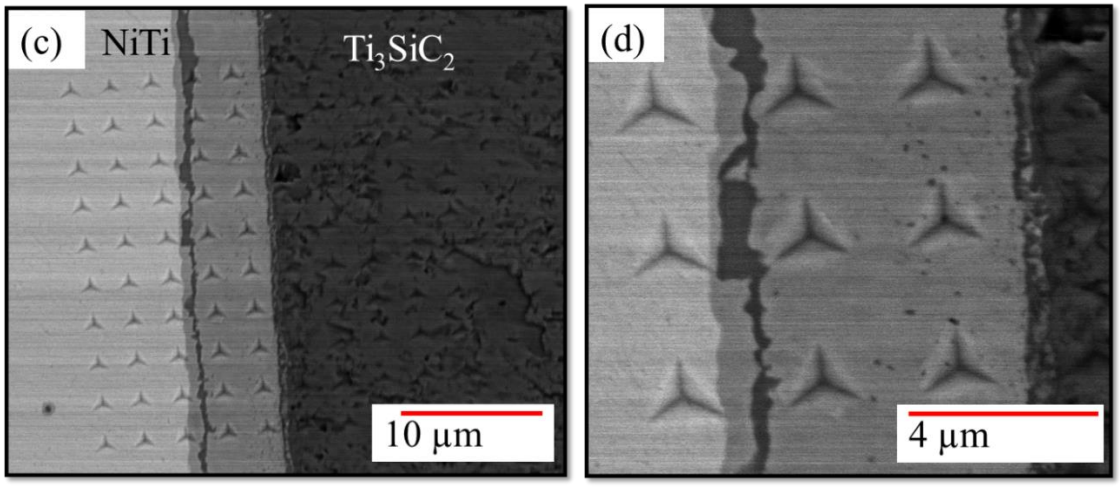

Figure 7.1 continued

7.2 Vickers Micro-Hardness Test

Vickers micro-hardness test is used to obtain indents on/near the NiTi-Ti_3SiC_2 interface and investigate whether any cracks initiate and/or propagate near the interface. Any further quantitative analysis of these results is difficult to perform as most of the indents are larger than the interface thickness for most of the bonding conditions. As the interface thickness is in the order of few microns compared to the indent size which is in the range of tens of microns, the indents lie partially in NiTi, interface and Ti_3SiC_2 regions. Interestingly for few cases, cracks near the NiTi-Ti_3SiC_2 interface are observed around the indents. One such indent obtained at a test load of 0.5 kg is shown in Figure 7.2 (a). No cracks are observed in the NiTi region whereas initiation of a single crack is observed at the bottom edge of the indent in the Ti_3SiC_2 regions close to the interface. This is expected as NiTi is known for its ductility and Ti_3SiC_2 for its high damage

tolerance. In brittle solids, Vickers indentation leads to crack initiation at the corners of the indents [55]. However, for pure MAX phases, it is very difficult to induce cracking from the corners of the Vickers indents [180-182]. Rather, damage in the form of delaminations, kinking and grain pushout and pullouts [182-184] is observed, as shown at the top right corner of Figure 7.2 (a). These mechanisms dissipate energy in the process and lead to confinement of damage around the indentation leading to the high damage tolerance in the MAX phases [55, 182]. The crack which initiated at the bottom edge of the indent propagates through Ti_3SiC_2 and terminates at the interface, as it is shown in high magnification image in Figure 7.2 (b).

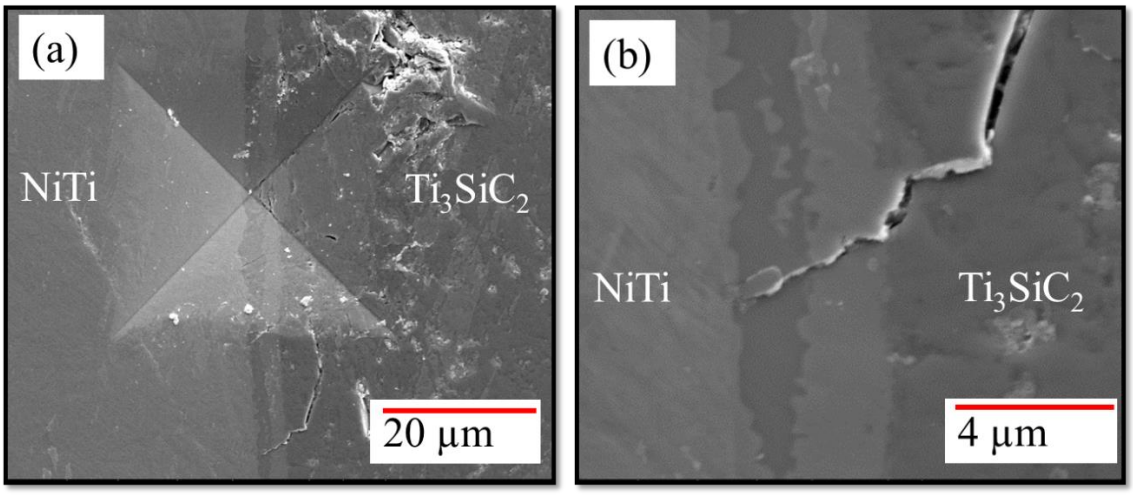

Figure 7.2 (a) Secondary electron (SE) image of the indent obtained during Vickers micro-hardness tests at a load of 0.5 kg on the NiTi-Ti_3SiC_2 interface bonded at 1000°C, 5 hours. (b) High magnification SE image of the crack initiated at the bottom edge of the indent terminating at the interface shown in Figure 7.2 (a).

When the indent was oriented, so that its diagonal lies along the interface between the two phases, some corner cracks that propagate along the interface were observed. For example, Figure 7.3 shows an indent obtained at a test load of 0.3 kg in the NiTi-Ti_3SiC_2 interface for the bonding condition of 1000°C, 1 hour. A large (~ 60 μm) crack initiates very close to the NiTi-Ti_3SiC_2 interface and propagates between Ti_3SiC_2 and interfacial reaction layer, and partially through Ti_3SiC_2. Some damage in the form of delamination is observed near the corners and edges of the indent on the Ti_3SiC_2 side. Figure 7.3 (b) shows a BSE image of the area marked as "Area A" in Figure 7.3 (a). Apart from the large crack, small cracks and crack patterns are also observed in the NiTi-Ti_3SiC_2 interface. These sub-cracks branch from the large crack in Ti_3SiC_2 and stop at the interface as it is depicted in Figure 7.3 (c) that shows a high magnification BSE image of the zigzag crack pattern obtained in the interface. The zigzag crack pattern and crack branching in the interface (Figure 7.3 c) is unlike straight crack paths commonly observed in typical brittle materials. The common phenomena of cracks originating elsewhere and terminating at the interface, as well as their torturous propagation path in the interface suggests the formation of a strong interface between bulk NiTi and Ti_3SiC_2 components at these temperatures, regardless of the fact that interfacial reaction layer has higher hardness and, in some locations, stiffness than parent phases. Nevertheless, more quantitative testing such as interracial fracture toughness tests is needed to characterize and effectively comment on the mechanical properties of the NiTi-Ti_3SiC_2 interface.

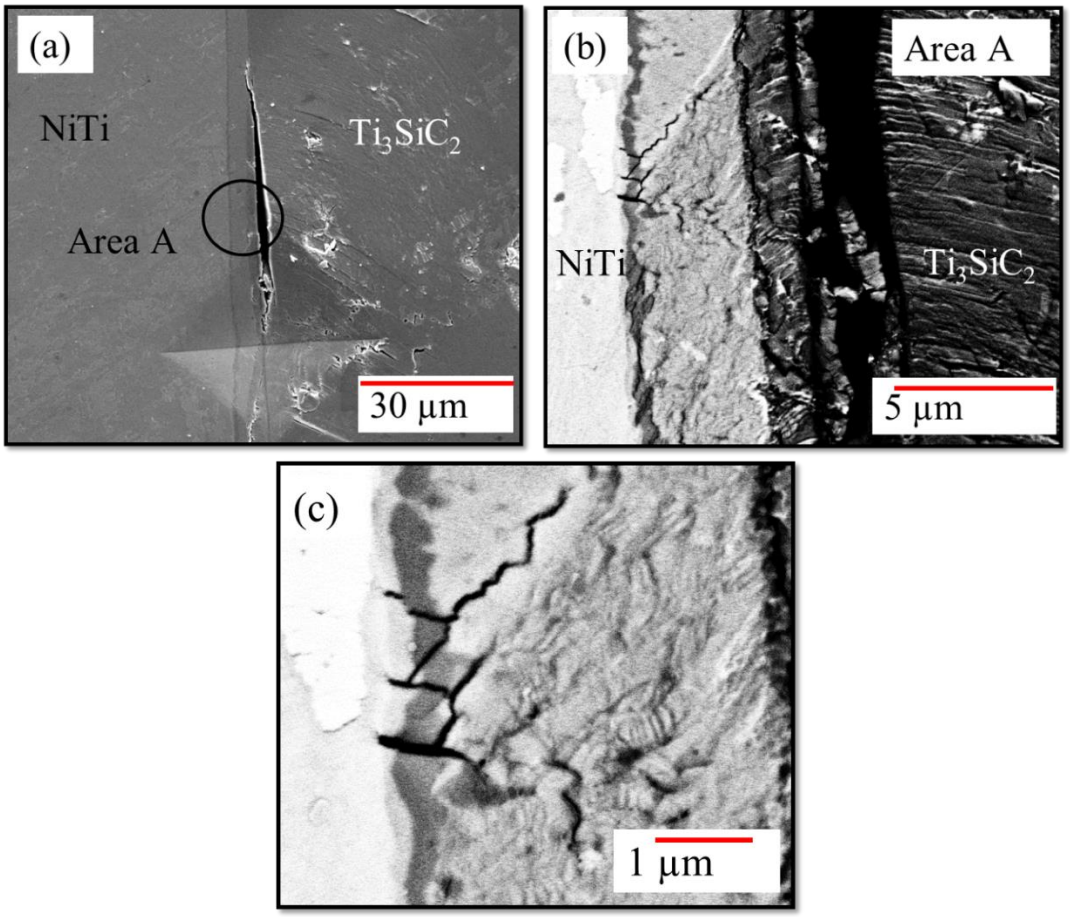

Figure 7.3 (a) Secondary electron (SE) image of the indent obtained during Vickers micro-hardness tests at a load of 0.3 kg on the NiTi-Ti_3SiC_2 interface bonded at 1000°C, 1 hour. (b) Backscattered electron (BSE) image of the "Area A" marked in Figure 7.3 (a), (c) High magnification BSE image of the zigzag crack pattern obtained in the interface as shown in Figure 7.3 (b).

7.3 Four Point Bend Delamination Test

Figure 7.4 shows the schematic of the bilayer sample along with the loading configuration for the four point bending tests [115]. A bilayer sample is notched through the thickness in the top layer, and a symmetric pre-crack (shown as a dotted line) is present along the interface between the two layers. Figure 7.4 also shows the coordinate

axis, height of top and bottom layer, (h_1 and h_2, respectively), distance between the inner and outer loading points (*l*), the width (b) and the load (P).

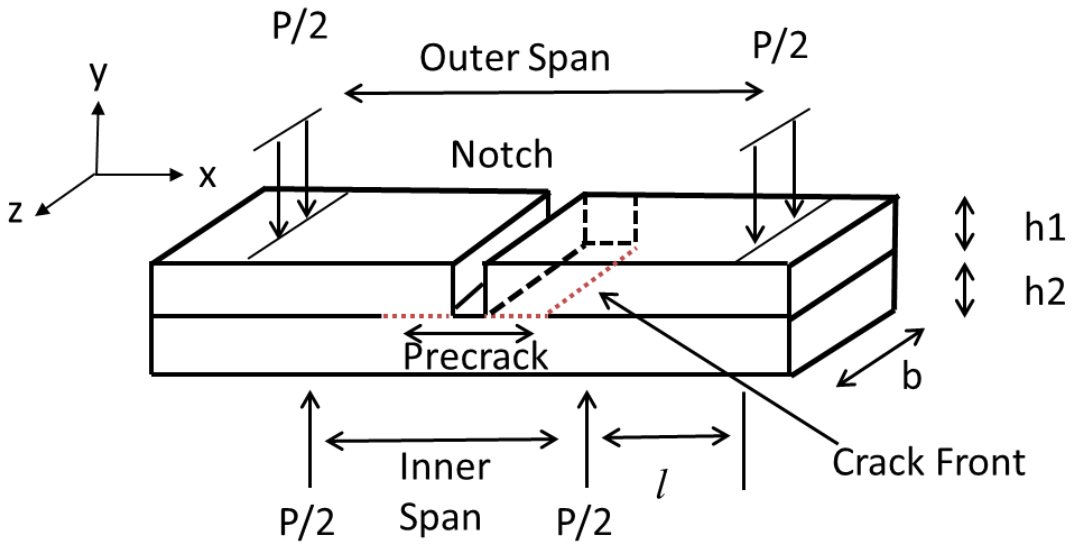

Figure 7.4 A schematic of the bilayer, notched four-point bending specimen showing symmetrical interfacial pre-cracks and crack front (red color) dotted lines

Considering the fact that the bilayer system undergoes a mixed mode fracture, it is important to characterize the mode mixity of the configuration chosen. Figure 7.5 shows the percentage of the total energy release rate for the different modes (I, II and III) as a function of the thickness ratio (h_1/h_2) for the configuration having Ti_3SiC_2 as the top layer. The prediction was obtained assuming both the material layers remain linear elastic and the virtual crack closure technique (VCCT). This technique is a numerical method to obtain the strain energy by mode assuming the energy required to close a

small area of the crack is the same energy required to grow the crack by the same area. For all the values of h_1/h_2 ratios considered, mode II, is found to be the most dominant followed by mode I, and mode III. For this study, h_1/h_2 ratio of 1 is selected for which the mode mixity is expected to be about 75 % mode II, 20 % mode I and 5 % mode III.

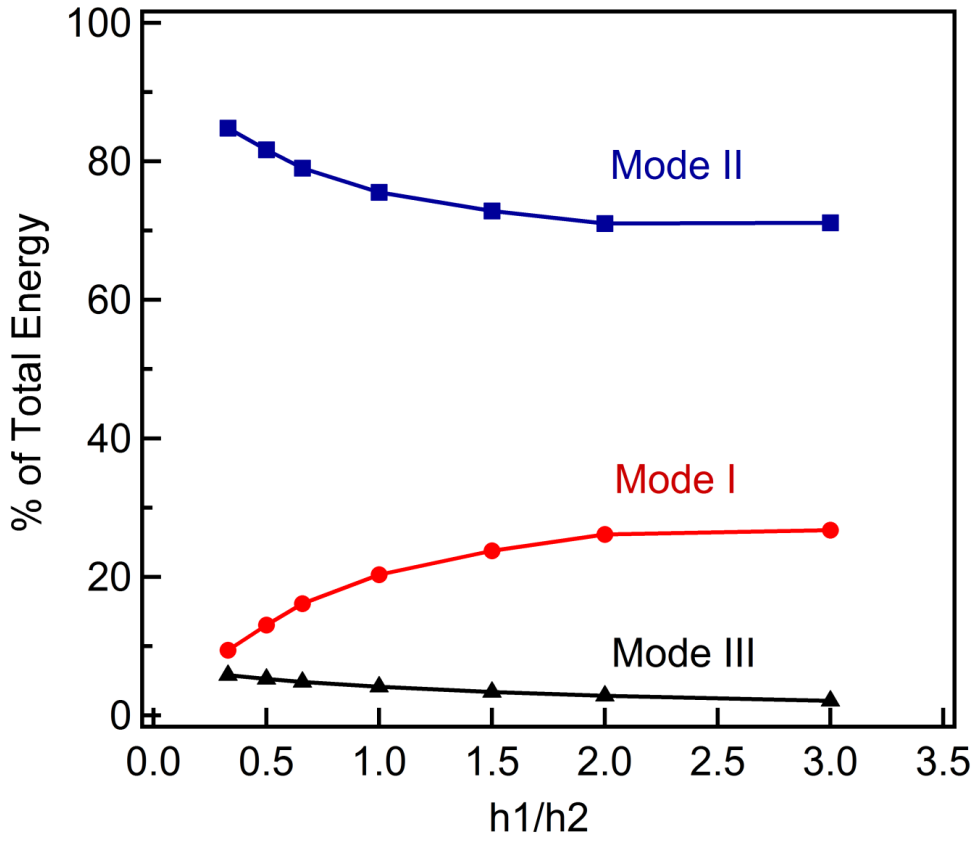

Figure 7.5 Percentage of the total energy for the different modes (I, II and III) as a function of the thickness ratio (h_1/h_2) for the configuration having Ti_3SiC_2 as the top layer (Figure courtesy of Keith Ballard [185])

7.3.1 Diffusion Bonding

Before studying the fracture of the interface between bilayer material systems and quantitatively measuring the interfacial fracture toughness or the critical strain energy release rate, they need to be joined first. The nature of the joining technique and corresponding processing conditions are bound to affect their fracture behavior. In this study, diffusion bonding mechanism is used as the joining technique for the NiTi-Ti_3SiC_2 bilayer system. The selection of joining mechanism and their corresponding parameters is guided by the results of our previous studies on diffusion bonding of NiTi and Ti_3SiC_2 bulk components [87] and their composites [159]. Herein, SPS is used as the joining technique at processing conditions similar to those used for processing NiTi-Ti_3SiC_2 composites to keep interfacial reactions and their layer thicknesses comparable. The end goal is to utilize the knowledge of the interfacial fracture behavior and their properties obtained in this NiTi-Ti_3SiC_2 bilayer study to better understand the fracture behavior of NiTi-Ti_3SiC_2 composites, in future studies.

The sample geometry for the four point bend delamination test [115] requires the creation of a notch and symmetric pre-cracks, as shown in Figure 7.4. The notch and the pre-cracks can be formed either before or after joining the individual bulk components. The literature reports a few ways to make the notch and pre-crack after joining [106, 108, 186-188]. The notch can be created by cutting in the material above the interface followed by loading under three-point bending with displacement control. It is loaded until the crack propagates from the notch to the interface and gets deflected a few millimeters along the interface [106, 187, 188]. Another technique is to use Knoop

indentation at the center of the beam and load the specimen under three-point bending to create and propagate the crack to and along the interface, similar to the technique described above [108]. Creating the notch after joining requires removal of the material from the top layer up to the or slightly above the interface followed by loading the specimen under three-point bending to propagate the notch to the interface. The problem with this technique is the large number of attempts required to achieve a successful specimen. Unsuccessful attempts lead the notch tip being either slightly above the interface in the top layer or slight below in the bottom layer, possibly leading to large scatter in the experimental results. When the notch tip is in the top layer, due to the non-homogeneous or textured top layer, the notch may not propagate vertically from its tip leading to the loss of symmetry in the bilayer geometry. The difficulty is further increased when the bimaterial system forms a new, thin reactive layer between the two components, as earlier observed for the NiTi-Ti_3SiC_2 bimaterial system. It was decided to make a notch in the top layer prior to joining and creating the pre-cracks by utilizing the fact that applied stress during solid state diffusion bonding is important for obtaining strong joints between the two components.

Figure 7.6 (a) shows a schematic of the punch and die set up used for the joining of NiTi and Ti_3SiC_2 components inside the vacuum chamber of the SPS machine. The novelty of the design lies in the fact that the top punch has been modified to generate symmetric pre-cracks in the bilayer along the interface. The top punch is symmetrically notched along its center axis so that little or no stress is applied to the region adjacent to the notch in the Ti_3SiC_2 layer. Stress plays an important role in the joining of two

components, especially when there is no presence of liquid phase at joining temperatures. Due to the lower stress in the region around the central notch, no or weak, sporadic bonding is expected leading to the formation of pre-crack along the interface. The pre-crack formed using the above technique is shown in Figure 7.6. Figures 7.6 (b) and (c) show low and high magnification SEM micrographs respectively of the notch and the pre-crack region. The top and bottom layers are Ti_3SiC_2 and NiTi respectively; with the dark vertical region at the center being the notch. The debonded region between the two layers is the pre-crack and is obtained on both sides of the notch. Figure 7.6 (c) shows another high magnification image of the interface region around the notch wherein the arrow depicts crack direction. The dark region on the right top corner is the notch.

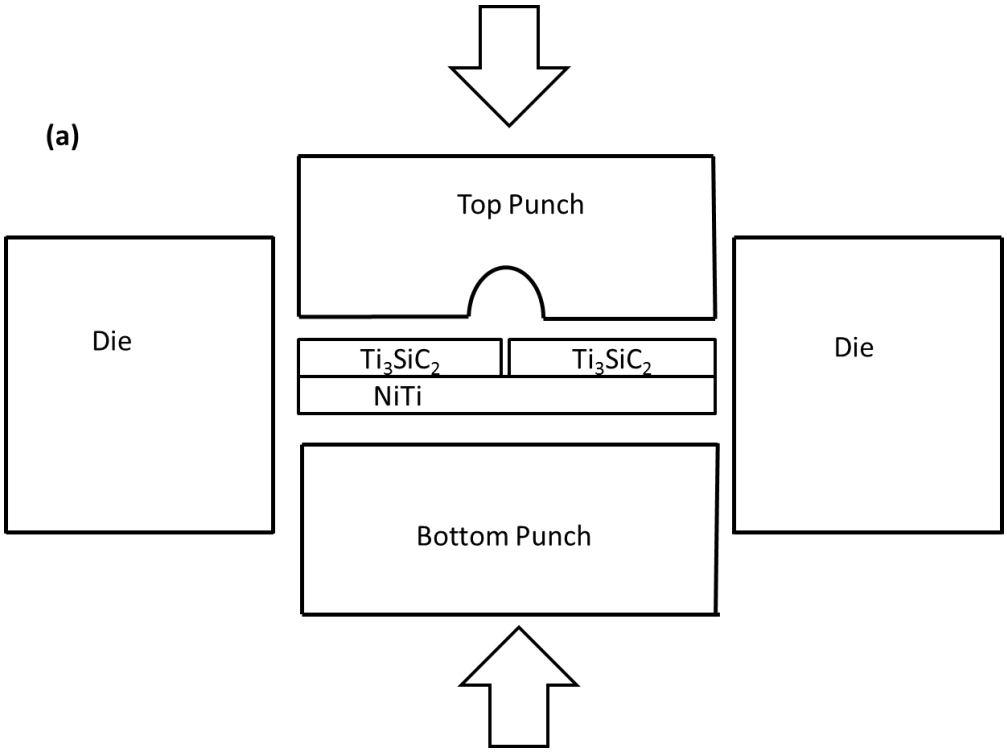

Figure 7.6 (a) Schematic of the punch and die set up used for the joining of NiTi and Ti_3SiC_2 components inside the vacuum chamber of the SPS machine

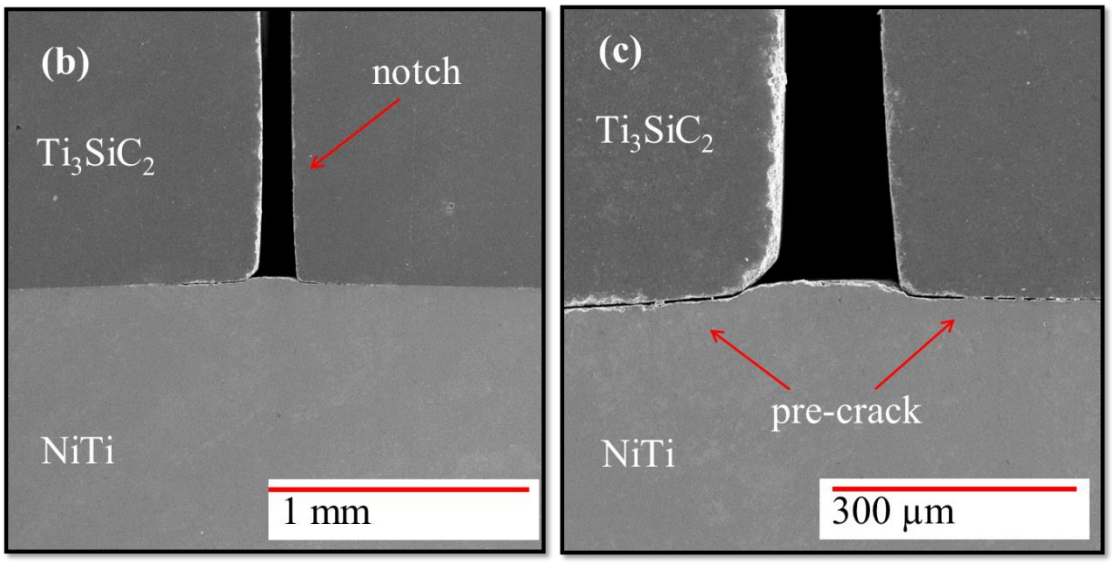

Figures 7.6 (b) and (c): Low (b) and high (c) magnification SEM micrographs of the notch and the pre-crack region respectively

7.3.2 Limiting Elastic Load

Before obtaining G_c using equation 1-5, one needs to check whether either of the two individual materials will yield before crack propagation and undergo large scale plastic deformation. Very few studies in the literature concerning the measurement of a bimaterial interfacial G_c have mentioned the phenomena of yielding in the bulk metal layer. Hardly any study in the literature, among those that mention yielding, calculate and check whether large scale yielding will occur prior to crack propagation. This is very important because plastic deformation can dissipate a significant amount of energy. Thus, if significant plastic deformation occurs far away from the crack tip prior to crack propagation, then the interfacial G_c values reported can be inaccurate.

In one study [113], the limiting elastic load (P_y) is estimated using simple bending theory given by the equation 13 below

$$P_y = \frac{bh_2^2\sigma_y}{3l} \tag{13}$$

where σ_y is the uniaxial yield strength of the metal layer. The limiting elastic load (P_y) is the load above which yielding occurs in the bottom layer in the region between the crack tips. Applying the equation 13 to the NiTi-Ti_3SiC_2 bilayer system, a limiting elastic load, P_y, of 110 N is obtained. This suggests that when the applied load exceeds 110 N, in this case, the region of NiTi between the inner loading points starts to plastically deform. From the uniaxial stress-strain curve of NiTi at room temperature (in martensite), the stress at which the curve starts to become non-linear is obtained. That

stress can be considered to be "yield" stress of NiTi. Yield stress of most metals is defined to be the stress at which they start to deform plastically (irreversible deformation) through movement of dislocations. SMAs (NiTi), rather detwin and this deformation is irrecoverable on unloading of stress. However, detwinning of NiTi (reorientation of different martensitic variants) is recoverable by heating the SMAs (NiTi) past a particular temperature, A_f, Austenite finish. For the purpose of discussion here, deformation through both detwinning and motion of dislocations can be considered permanent as no heating is carried out and the fact that both mechanisms dissipate energy in the process. If the critical load drop (P_c) is obtained before the load reaches a value of P_y, then G_c can be calculated from the P_c using the equations 1-5. On the other hand, if $P_c > P_y$, then plastic deformation of NiTi in between the inner loading points starts to occur before crack propagation. P_c value cannot be obtained *a priori* and has to be obtained through experiments.

7.3.3 Load-Displacement Curves

Figure 7.7 (a) shows a typical load displacement curve of NiTi-Ti_3SiC_2 bilayer sample obtained using a four-point bend test under cyclic loading. Critical strain energy release rate (G_c) of the interface can be obtained by using the critical load (P_c) from the load–displacement curve at which the crack propagates along the interface. The critical load drops are obtained by plotting the slope of the load-displacement curve of the fourth cycle from Figure 7.7 (a) as a function of the load (Figure 7.7 (b)). When the slope becomes negative, a load drop occurs. Care is taken to consider only those load values as

critical which have highly negative slope values. Multiple load drop values are obtained and they increase with an increasing applied displacement. On measuring the crack length just before each of the critical load drops, Figure 7.7 (c) is obtained. It plots the crack length values of the left crack with the load at critical load drop values. As the crack propagates from the pre-crack length to the inner loading point, the critical load, P_c, increases. Directly applying the equations 1-5 apparently suggests that G_c of the interface increases with increasing crack length. More energy is required to propagate the crack as the crack length increases, suggesting an apparent increasing R-curve (resistance curve) behavior. This is quite contrary to what is expected from the four point bend delamination test. No dependence on the crack length of G_c is expected due the constant moment between the inner loading points. G_c should have a steady state value, and one expects a single critical load drop at which the crack propagates until it meets the inner loading point, thus giving a unique value of interfacial G_c. This leads us the following questions: 1) Is the interface G_c value intrinsically different at different locations along the interface; 2) Why does the NiTi-Ti_3SiC_2 bilayer system show increasing R-curve behavior; 3) Does the NiTi starts to deform plastically away from the crack tip before crack propagation; 4) Is the crack always propagating along the interface; If not, then are we actually quantifying interfacial G_c? These questions will be discussed in the following sections.

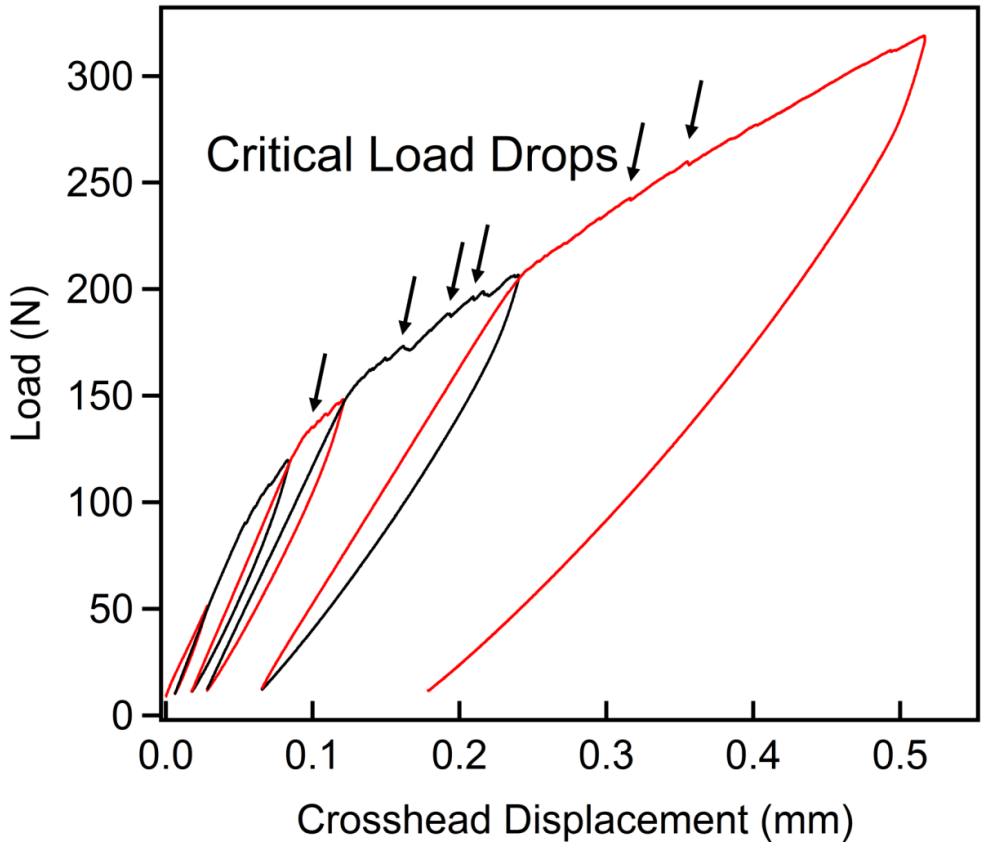

Figure 7.7 (a) Typical load displacement curve of NiTi-Ti_3SiC_2 bilayer sample obtained using a four-point bend test under cyclic loading

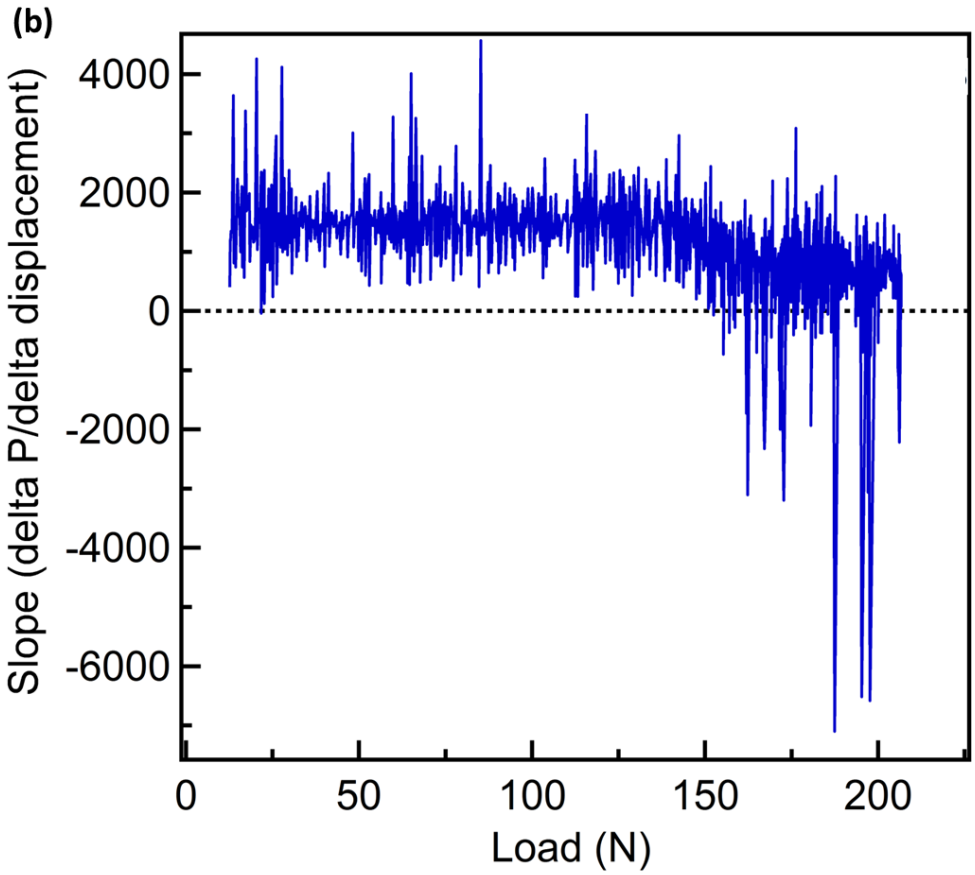

Figure 7.7 (b) Slope of the load-displacement curve of the fourth cycle from Figure 7.9 (a) as a function of the load

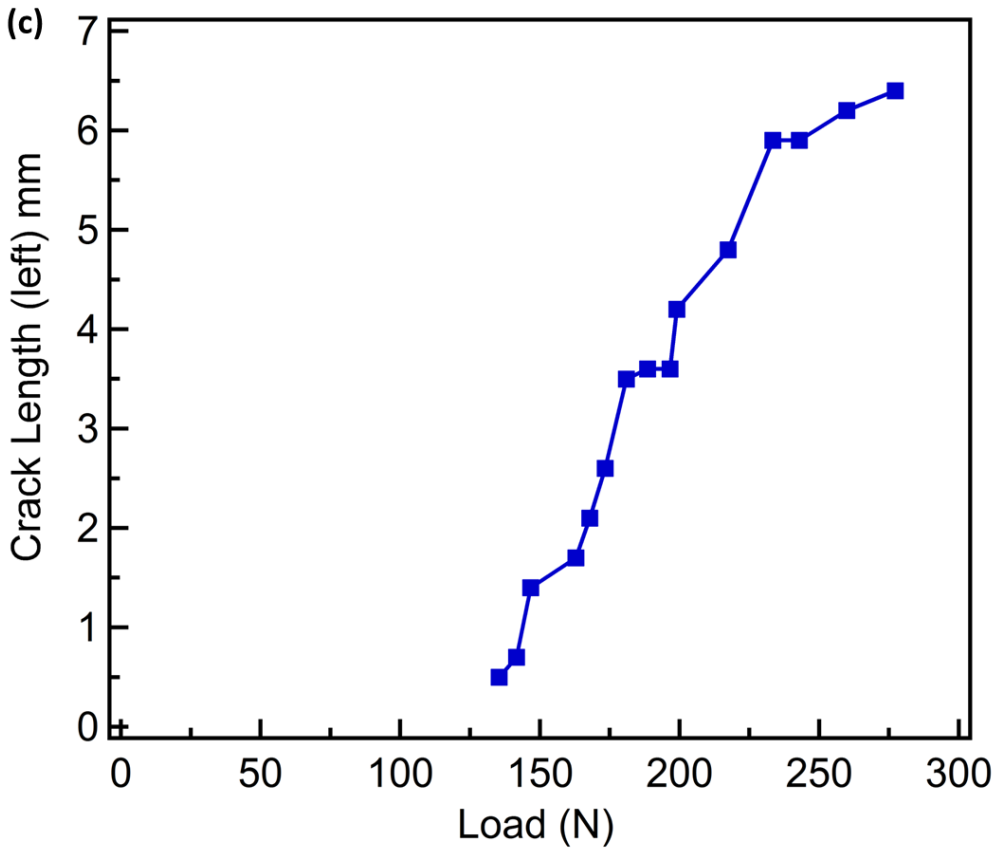

Figure 7.7 (c) Crack lengths (left) as a function load just before the critical load drops

7.3.4 NiTi Deformation

For the NiTi-Ti_3SiC_2 bilayer system, the limiting elastic load (P_y) of 110 N is obtained using equation 13. In this study, several bilayer samples are tested using a four point bend delamination test. An average value for the first critical load drop when both the crack lengths are at least 1.5 mm long is 130 N. The 1–1.5 mm region on each side of the notch is the pre-crack region where no or weak, intermittent bonding is observed due to the design of the die, described in section 7.3.1. Hence, load drops which are

observed until the crack length on both sides before 1.5 mm are not considered, as they do not represent the crack propagation in bonded interface.

Since the average value of the first critical load drop (130N) is higher than the limiting elastic load (110), nonlinear deformation starts in the NiTi layer before the crack propagates. Finite element analyses are used to calculate stress fields for three critical loads using the measured crack lengths at those loads. Linear elastic material properties are used, and the volume of NiTi experiencing a Von Mises stress greater than the detwinning stress is plotted, as shown in Figure 7.8. The percent volume exceeding the detwinning stress for the critical loads (P_c) and crack lengths (a_1, a_2) are (a) 0.5 % for P_c = 135N, (0.5, 1.2) mm; (b) 2.9 % for P_c = 181N, (3.5, 2.1) mm; and (c) 13.7 % for P_c = 277N, (6.4, 6.1) mm. These critical load drop values and corresponding crack lengths are from the same sample and represent a state before the crack has grown out of the precrack region (both crack lengths are less than 1.5 mm), after some crack propagation, and late in the experiment before it reaches the loading points, respectively. The percent volume of NiTi over the detwinning stress is considered to be a first order approximation of the significance of the energy dissipated via detwinning. Unfortunately, it is difficult to quantify the amount of energy dissipated by detwinning.

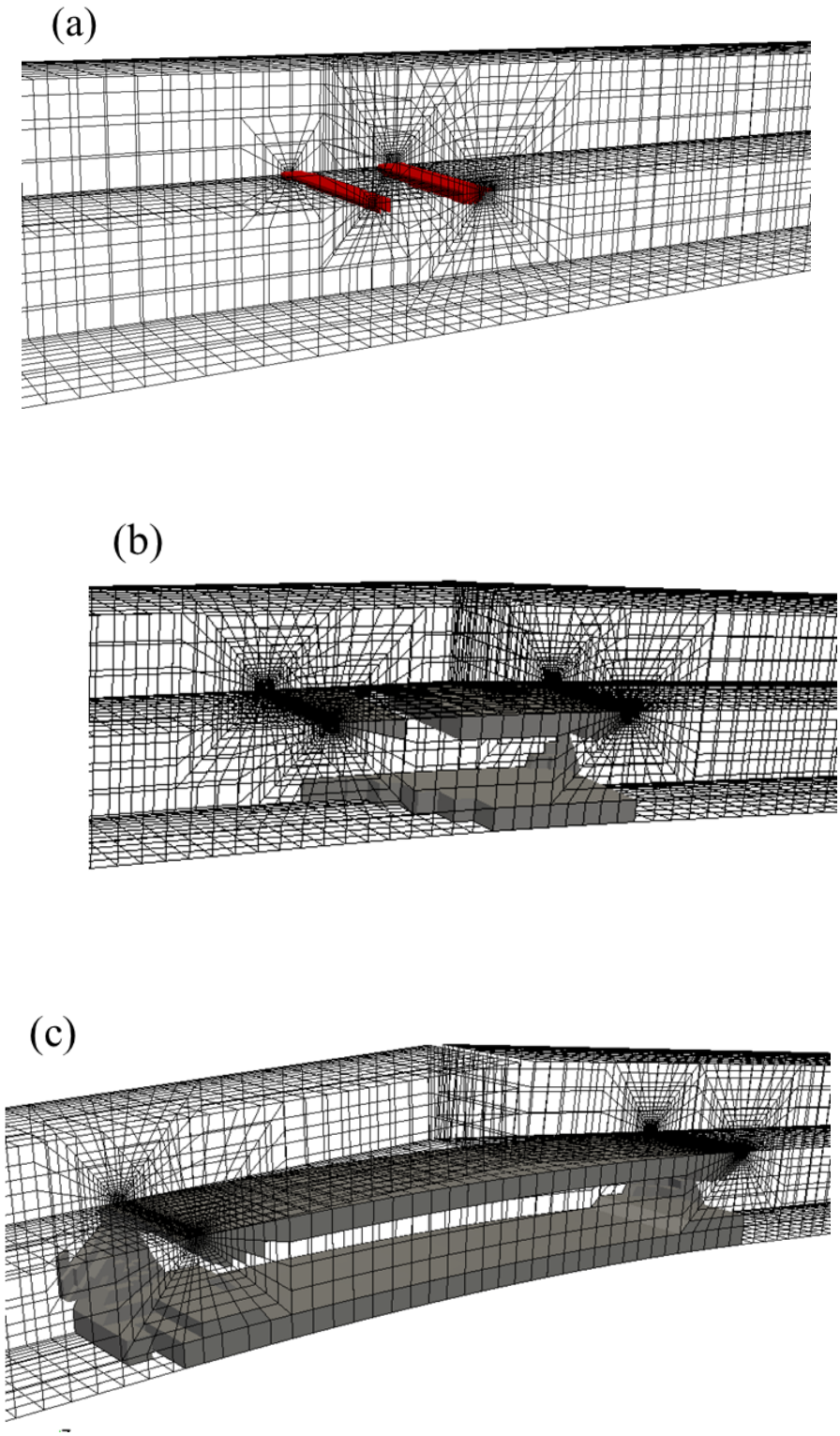

Figure 7.8 Percent volume of NiTi experiencing stresses higher than detwinning stress increases at different critical loads (Figure courtesy of Keith Ballard [185])

Crack growth is predicted to occur when the available energy for fracture is enough to overcome the resistance of the material. Energy release rate (G) is the measure of energy available for crack growth and is defined as the rate of change of potential energy with crack area [189]. The crack propagates when G reaches a critical value (G_c) which is a measure of resistance to crack propagation (or fracture toughness of the material). The analytical solution [113] (equations 1-5) for calculating G_c using the measured P_c assumes that the material remains linear elastic and plastic deformation, if any, is confined to a small region near the crack tip. However, for the NiTi-Ti_3SiC_2 bilayer system, NiTi deformation occurs away from the crack tip in the region between the inner loading points. As the NiTi starts to nonlinearly deform prior to crack propagation, part of the available energy is being dissipated through the nonlinear deformation of NiTi and the rest is being spent in crack propagation. Thus equations 1-5 are not valid for the NiTi-Ti_3SiC_2 bilayer considered here. For the first critical load drop of 135 N, a very small region of the NiTi is predicted to detwin, so the error may not be as significant. However, much more of the NiTi detwins at higher critical loads. Since it is difficult to quantify the amount of energy dissipated by detwinning, there is no basis for assuming that the 0.5% of NiTi over the detwinning stress at the lowest critical load may consume either negligible amount or large amounts of energy compared to energy spent in crack propagation. To quantify the energy spent in propagating the crack to obtain G_c of interface, one must determine the energy dissipated by detwinning the NiTi, which requires nonlinear analyses that were not conducted as part of the present work.

However, one can use the limiting elastic load value (P_y) to calculate a lower bound for G_c using equations 1-5, since the NiTi is not predicted to detwin until an applied load of P_y. This results in a minimum G_c value of 115 J/m^2. It is important to note that this minimum value of G_c is calculated without the results of the experiments, but this is only possible because the experiments showed critical load drops at loads which exceeded the limiting elastic load. Since the actual value of G_c is unknown, this minimum G_c at least allows comparisons to other material systems. Another interesting observation from the Figures 7.7 (c) is that the P_c values increase with increasing displacement/crack length. This suggests that higher energy is required to propagate the crack as the crack length increases, suggesting an apparent increasing R-curve (resistance curve) behavior. One clear reason for this observation is the increased energy absorption caused by the increased deformation of NiTi between the inner loading points. From Figure 7.8, it is evident that the percent volume of NiTi experiencing stresses higher than detwinning stress increases as the load is increased from 135 N (Figure 7.8 (a)) to 277 N (Figure 7.8 (c)). This contributes to the increased energy absorption by the NiTi-Ti_3SiC_2 system.

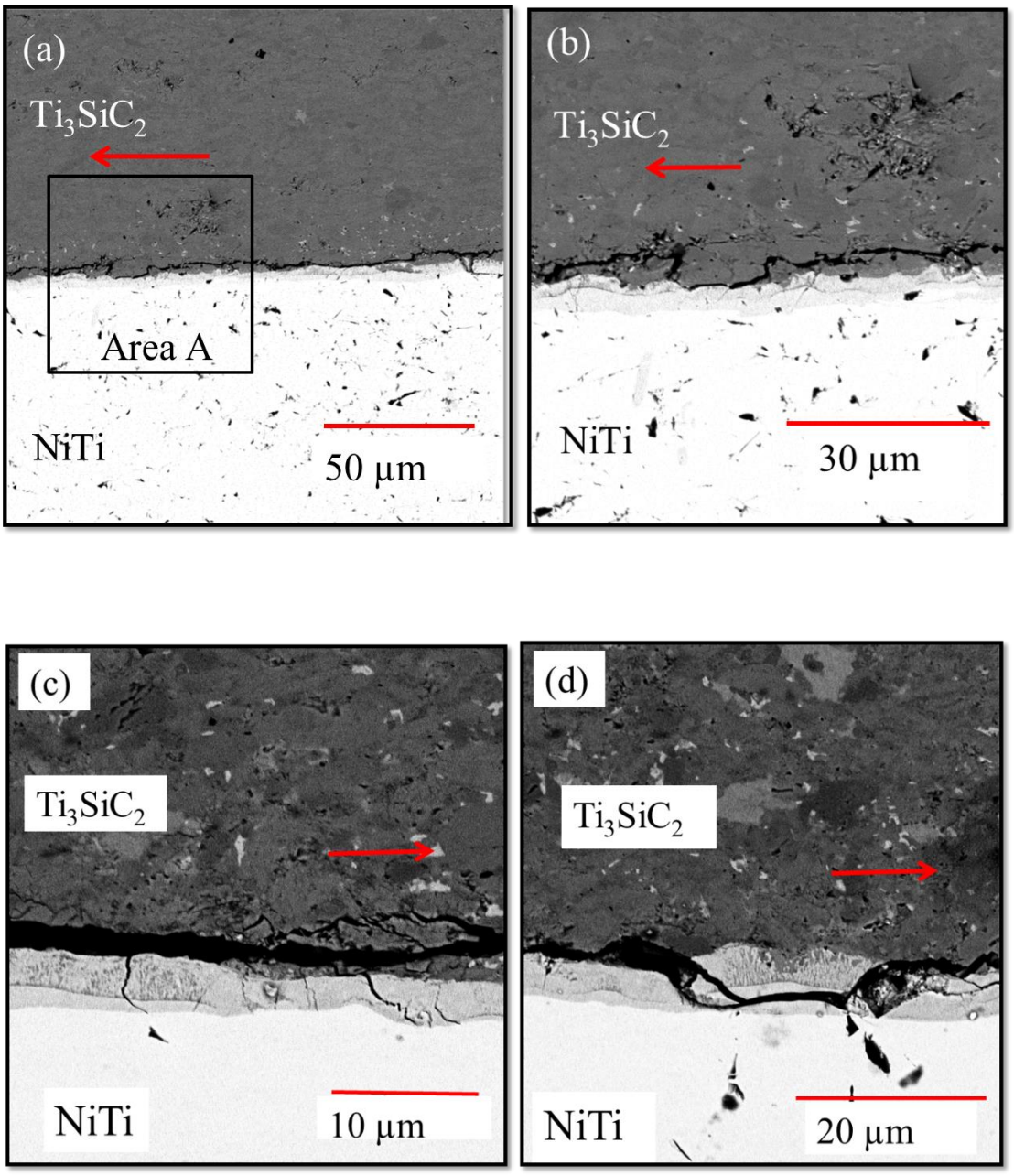

Figure 7.9 Backscatter electron (BSE) images of the crack propagation around the interfacial region between the joined NiTi and Ti_3SiC_2 layers. The direction of crack propagation is indicated by the red arrow. Figure 7.9 (b) shows the location marked Area A in Figure 7.9 (a). Figures 7.9 (c) and (d) show BSE images of the interface obtained from different locations where the crack is propagating to the right of the image as indicated by the arrow (red)

7.3.5 Crack Path

Figure 7.9 shows backscatter electron (BSE) images of the crack propagation around the interfacial region between the joined NiTi and Ti_3SiC_2 layers. The direction of crack propagation is indicated by the red arrow. Figure 7.9 (b) shows the location marked Area A in Figure 7.9 (a). All the BSE images in Figure 7.9 are obtained after the NiTi-Ti_3SiC_2 bilayer has experienced the load-displacements cycles depicted in Figure 7.7 (a).

The light grey region, between the dark grey Ti_3SiC_2 phase (top layer) and the bright white NiTi phase, is the interfacial reaction layer. Previous studies on NiTi-Ti_3SiC_2 bilayer couple have also demonstrated the formation of new a interfacial reaction layer wherein their morphology and reaction phases are extensively characterized under a wide range of temperatures and processing times [87]. The reaction layer itself is comprised of many layers of reaction phases (interphases) and the interfacial structure has the form NiTi / Ti_2Ni / Ti_5Si_3 / NiTiSi / Ti_3SiC_2. Si and Ni are the diffusing elements that lead to the formation of these reaction layers between the NiTi and Ti_3SiC_2 phase. Therein, the total interfacial reaction layer thickness varied from sub-micron to 55 microns when the joining temperatures are varied from 800 to 1100°C respectively. In this study, the total interfacial reaction layer thickness is observed to be around 5 microns.

Fracture in the NiTi-Ti_3SiC_2 bimaterial system manifests itself in the form of various crack trajectories as shown in Figure 7.9. Fracture occurs, (a) along the interface between Ti_3SiC_2 and the reaction layer, (b) inside the Ti_3SiC_2 phase and, (c) in the

different phases of the reaction layer. Along with the primary crack, secondary cracks are also observed, which propagate through the reaction layer terminating at the NiTi layer. The intermetallic reaction phase closer to the Ti_3SiC_2 phase in the reaction layer is NiTiSi, and fracture is observed at the interface of NiTiSi and Ti_3SiC_2. The crack is also observed to alternate between the Ti_3SiC_2 layer and along the interface between NiTiSi and Ti_3SiC_2.

7.3.5.1 Crack Propagation inside the Ti_3SiC_2 Layer

Figure 7.9 (b) shows a high magnification BSE image of the crack propagation path. Moving from the right to the left of the image, initially the crack is completely inside the Ti_3SiC_2 phase, then it gets back between the reaction layer and Ti_3SiC_2, and again back to the Ti_3SiC_2 phase. This alternating trajectory of the crack between the interface and its adjacent layer is not uncommon in two bulk materials joined using a third interlayer or sandwich specimens and has been observed previously in the literature. For example, in an alumina bilayer specimen joined using pure Al or Al-Mg alloy interlayer, the crack alternated between Al_2O_3 and the Al_2O_3/interlayer interface [110]. There is an excellent review on the mixed mode cracking in bilayer systems [99], with a specific section on failure modes of joints. Therein, a multitude of cracking morphologies, including interface cracking, straight and wavy cracking in the interlayer, and alternate cracking between the interlayer and adjacent layer are depicted in a schematic and issues surrounding the selection of these cracking morphologies have been discussed. Similar multiple crack trajectories are also observed in this study in the

NiTi-Ti_3SiC_2 bimaterial system, and the interface fracture toughness may have a strong dependence on these crack morphologies. The alternating path of crack propagation between the Ti_3SiC_2 layer and the interface between reaction layer and Ti_3SiC_2 may be due to relative toughness of these regions [99]. To predict the crack trajectory at an interface, characterization of local stress fields is very important, since they affect the direction of crack propagation and the corresponding interfacial fracture energy [108]. These local stress fields are commonly described by the phase angle ψ, which is equal to the ratio of the arc tangent of shearing to opening stress intensity factors at the crack tip, wherein pure mode I and II correspond to ψ of 0° and 90° respectively [187]. This assumes the mode III component is negligible and does not play a significant role. The critical strain energy release rate (G_c) of the bimaterial interface depends on the phase angle ψ and is typically found to increase with an increase in ψ (higher shear component), which is attributed to the increased work of friction in the wake of the crack tip[108, 187, 190]. Thus, it is important to report the ψ along with the G_c for bimaterial systems for comparsion of different material systems. For this NiTi-Ti_3SiC_2 bimaterial system, ψ is 75°, assuming both the constituent materials remain linear elastic or that the detwinning does not change the ratios of stress at the crack tip.

Another factor that could contribute to the apparent R-curve behavior is the nonlinear fracture behavior of MAX phase ceramics. The crack is observed to propagate into the Ti_3SiC_2 layer, and MAX phases in general and especially Ti_3SiC_2 are known for their high fracture toughness and increasing R-curve behavior [48, 55]. MAX phases are believed to possess one of the highest values of fracture toughness ever reported for a

monolithic, single phase, non-transforming ceramic [55]. At room temperature, coarse grained Ti_3SiC_2 shows increasing R-curve behavior with fracture toughness values of crack growth initiation of 8.5-11 MPa-$m^{1/2}$ to peak values of 14-16 MPa-$m^{1/2}$ after 2.7 - 4 mm of crack extension [66]. Apart from the presence of bridging and frictional pullout mechanisms, similar to processes observed in Al_2O_3 [67], Si_3N_4 [68], and SiC [69], Ti_3SiC_2 exhibits crack bridging through heavily deformed lamellae, along with a significant amount of delamination and bending [66]. These mechanisms contribute to the high fracture toughness values of Ti_3SiC_2. The ability of MAX phases to contain damage through the mechanisms of delamination, kinking of individual grains makes them an exceptional damage tolerant material [55]. These attributes of the Ti_3SiC_2 is expected to contribute to the apparent increasing R-curve behavior of the NiTi-Ti_3SiC_2 bilayer system.

7.3.5.2 Crack Diversion inside the Reaction Layer

Figure 7.9 (c) shows a BSE image of the interface obtained from another location where the crack is propagating to the right of the image as indicated by the arrow (red). Along with the observation of a major crack between the Ti_3SiC_2 phase and the NiTiSi phase, secondary (minor) cracks are also observed. These secondary cracks propagate through the reaction layer terminating in the NiTi also contribute to the increased high G_c value of the NiTi-Ti_3SiC_2 phase bilayer system. The secondary cracks observed in Figure 7.9 (c) are similar to those previously observed for the NiTi-Ti_3SiC_2 material system. These diversions of the crack front into different regions consume energy

making the crack propagation difficult through the NiTi-Ti_3SiC_2 bilayer system. A few cases of the crack propagating through the different phases of the interfaces have also been observed (Figure 7.9 (d)). Here, the crack is observed to enter from the Ti_3SiC_2/NiTiSi interface into the reaction layer, and then continue to propagate through the Ti_2Ni phase and divert back to the weaker Ti_3SiC_2-NiTiSi interface.

7.3.6 G_c Value Comparison with Literature

The NiTi-Ti_3SiC_2 material system has a minimum G_c of 115 J/m^2 for a phase angle ψ value of 75°. It is important to report the G_c values with the corresponding ψ values, as G_c depends on ψ. Table 7.1 summarizes the interfacial G_c values of some of the material systems studied in the literature using four point delamination tests along with their corresponding mode mixity values. For the model Al-PMMA system joined using epoxy, the interfacial G_c is measured to be in the range of 11-13 J/m^2 [113]. Interfacial strain energy release rate of the Al-Glass system joined using a thermoplastic adhesive, which is translucent and brittle at room temperature, is found to be in the range of 5-25 J/m^2 with slight differences between Glass/adhesive and Aluminum/adhesive values [112]. For the NiAl/Cu system, G_c is reported to be in the range of 37-62 J/m^2 and crack extension occurred prior to large scale specimen yielding [191].

Table 7.1 Interfacial G_c values of some of the material systems studied in the literature using four point delamination tests along with their corresponding mode mixity values

Material	**Interlayer**	**J/m^2**	**Mode Mixity, Ψ (degrees)**
Glass-Steel	Epoxy	26	53 [24]
PMMA-Al	Epoxy	6	68 [24]
PMMA-Al	Epoxy	11-14	68-74 [22]
Al_2O_3-Glass	thermoplastic	7-9	42 [24]
Glass-Glass	thermoplastic	7	42 [24]
Al_2O_3-Al_2O_3	Glass	10	42 [24]
Sapphire-Sapphire	Au	~50	52 [53]
Stainless Steel-Cu	-	91-734	42 [52]
NiAl-Steel	-	37-62	45 [52]
Al_2O_3-Al_2O_3	Ti	10-45	45 [40]
NiTi-Ti_3SiC_2	-	> 115	75

However, for the stainless steel/Cu system, the large variation in the G_c calues is observed due to variation in the interface toughness. Such large toughness variation is attributed to the variation in the temperatures during microcasting process, leading to non-uniform interface. In our study, the minimum G_c of the NiTi-Ti_3SiC_2 material system is much higher than materials systems joined using a polymer interlayer [113, 115] and comparable to other systems which are joined either with a metallic interlayer [186, 192] or without an interlayer [191].

As shown in Figure 7.9 and described in section 7.3.5, the crack is observed to enter the Ti_3SiC_2 layer multiple times and has undulating trajectory. This suggests that the resistance to crack propagation along the interface between the reaction layer and Ti_3SiC_2 is comparable to that of the pure Ti_3SiC_2 layer under similar mode mixity conditions. If the interface was considerably weaker than Ti_3SiC_2 layer, then crack would have propagated all along the interface, instead of going in the Ti_3SiC_2 layer several times. This inference is based on the observation of the crack propagation path after the four point delamination test. When a high strength Al-4% Mg interlayer is used to join two alumina layers, crack propagation is observed to occur in the alumina layer [193]. In the same study, when a comparatively lower strength pure Al layer is used instead of Al-4% Mg, crack propagation is observed in the Al layer. In both cases, crack propagation is observed in the bulk of the constituents instead of the interfaces between them suggesting higher resistance to crack propagation along the interface as compared to constituent materials [108, 193]. The NiTi-Ti_3SiC_2 material system has a minimum G_c of 115 J/m^2 and qualitatively, G_c value comparable to that of Ti_3SiC_2 for a phase angle ψ

value of 75°. As interfaces are critical in determining the overall properties of the composite, the fact that NiTi-Ti_3SiC_2 material system form strong reaction layer is useful in fabricating tough NiTi/Ti_3SiC_2 composites. As G_c is a non-unique value and depends on the phase angle ψ, this study needs to complemented with future interface fracture studies in the different range of mode mixity values to generate a fracture locus (G_c as a function of ψ).

7.4 Summary

- Nano-indentation results show that the elastic moduli of the phases in the interface are higher than that of NiTi and close to that of Ti_3SiC_2. An average elastic modulus of 278.68 ± 10.02 GPa is obtained for the interface as compared to 91.62 ± 11.16 GPa for NiTi and 263.21 ± 31.89 GPa for Ti_3SiC_2. The hardness of the phases in the interface is higher than that of Ti_3SiC_2 and NiTi. An average hardness of 17.55 ± 0.95 GPa is obtained for the interface as compared to 5.44 ± 0.73 GPa for NiTi and 11.86 ± 1.80 GPa for Ti_3SiC_2.
- Vicker's micro-hardness tests are employed for qualitative mechanical characterization of the NiTi-Ti_3SiC_2 interface. The indents obtained by Vickers test near the interface region lead to cracks which terminate at the interface. Secondary zigzag crack patterns are also observed in the interface indicating a good resistance to the crack propagation. However, quantitative analysis of fracture toughness measurements is needed to effectively comment on the mechanical properties of the interface.

Four point bend delamination test is used to characterize and investigate interfacial fracture of NiTi-Ti_3SiC_2 bilayer system under mixed mode loading configuration. The major findings of this study are as follows:

- Bulk components of NiTi and Ti_3SiC_2 have been successfully joined using spark plasma sintering technique.
- NiTi starts to deform plastically in the region between the inner loading points prior to crack propagation. Thus, critical strain energy release rate of the interface cannot be obtained using analytical equations 1-5 obtained by linear elastic fracture mechanics. A part of available energy is being dissipated through the nonlinear deformation of NiTi and the rest is being spent in crack propagation.
- NiTi is predicted to detwin between the inner loading points at an applied load of 110 N and the first critical load drop occurs at 135 N. Detwinning of NiTi between the inner loading points is one of the reasons for the observed increasing R-curve behavior in NiTi-Ti_3SiC_2 bilayer system.
- The minimum interfacial critical strain energy release rate (G_c) for the NiTi-Ti_3SiC_2 bilayer system is 115 J/m^2 and qualitatively, G_c value comparable to that of Ti_3SiC_2 for a phase angle ψ value of 75°. This G_c value is obtained by using the load at which NiTi yields between the inner loading points, prior to crack propagation. As interfaces are critical in determining the overall properties of the composite, the fact that NiTi-Ti_3SiC_2 material system forms strong reaction layer is useful in fabricating tough NiTi/Ti_3SiC_2 composites.

- Fracture occurs along the interface between Ti_3SiC_2 and NiTiSi phase, inside the Ti_3SiC_2 phase and also in the different phases in the reaction layer. It is also observed to alternate between the Ti_3SiC_2 layer and along the interface between NiTiSi and Ti_3SiC_2. Secondary cracks are also observed and they propagate through the reaction layer terminating on reaching NiTi.
- Reasons for the observed R curve behavior in the NiTi-Ti_3SiC_2 bilayer system are as follows: 1. Higher energy dissipation due to plastic deformation of NiTi between the inner loading points far away from the crack tip, 2. Increasing R-curve behavior of MAX phases, 3. Initiation and propagation of the secondary cracks through the various layers of the interface terminating in the NiTi. 4. Crack diversion into the different reaction phases in the reaction layer and back to the weak Ti_3SiC_2–NiTiSi interface.

8. OVERALL SUMMARY AND FUTURE WORK

8.1 Summary

In the present work, for the first time, a novel shape memory alloy / MAX phase composites has been processed using spark plasma sintering. Thermo-mechanical response and damping behavior of NiTi/Ti_3SiC_2 composites has been studied in detail. The major findings of this work are as follows:

Composites:

- Microstructural characterization via scanning electron microscopy clearly depicted the presence of two distinct, interconnected phases, NiTi and Ti_3SiC_2, along with some remnant porosity in the composites. Martensitic transformation in NiTi/Ti_3SiC_2 composites was confirmed by the transformation peaks observed using differential scanning calorimetry. One way and two way shape memory effects were observed in the composites during thermo-mechanical characterization.
- The stress-temperature phase diagrams of the composites are analyzed and compared to those of pure NiTi. For the composite, M_s and A_f are shifted to higher values whereas M_f and A_s stayed the same or are shifted to slightly lower values, as compared to pure NiTi, at each stress. The increase in the M_s and A_f is due to the creation of local stress concentrations when external load is applied as a result of porosity and non-transforming reaction phases at the interface between

NiTi and Ti_3SiC_2. Lowering of M_f and A_s is attributed to two factors: firstly, the presence of non-transforming ceramic regions around the transforming NiTi may cause a back stress due to deformation mismatch when the martensite plates propagate, thus requiring higher driving force to finish the transformation. Secondly, the stiffness of the NiTi phase is lowered during the transformation, thus decreasing the stress experienced by the NiTi phase, leading to a decrease (respectively, increase) in the forward (respectively, reverse) transformation finish temperatures.

- Transformation and irrecoverable strains in the composites show similar trend as observed in pure NiTi; both increase with increasing applied external stress. However, the ratio of irrecoverable to transformation strains of the composite is higher when compared to that of pure NiTi and the additional irrecoverable strain is caused because of the constraints imposed by the Ti_3SiC_2 phases around the transforming regions in NiTi and possible deformation of Ti_3SiC_2 phase (e.g. formation of permanent kink bands).
- Similar to the one way effect, increase in TWSM strain is observed with increase in applied external stress during prior thermo-mechanical cycling. The ratio of TWSM to transformation strain in the composite is lower than that in pure NiTi because the presence of Ti_3SiC_2 interpenetrating regions and the complex stress state at the interface between NiTi and Ti_3SiC_2 upon transformation prevents the accumulation of enough directional internal stresses that lead to TWSME.

- All the composites show fully reversible, closed, non-linear hysteretic stress-strain loops up to the stress of 200 MPa. The as-sintered (AS) NiTi/Ti_3SiC_2 composite shows higher energy dissipation than its individual components. At 200 MPa applied stress, the energy dissipation measured in the AS composite is thirteen times larger than fine grain fully dense pure Ti_3SiC_2 and two times larger than pure NiTi. This increase is due to the following reasons: First, higher stress experienced by the Ti_3SiC_2 phase due to difference in elastic moduli of NiTi and Ti_3SiC_2 phases which lead to higher damping in the Ti_3SiC_2 phase; second, damping due to hysteretic movement of twins and twin boundaries in NiTi phase; third, newly formed twins and twin boundaries in the NiTi phase near the interface region due to relaxation of residual stresses in the composite; and lastly, the presence of porosity.
- The highest energy dissipation, (W_d), is observed at all stress values for the thermo-mechanically cycled (TC) composite followed by the as-sintered (AS) composite. At 200 MPa, the energy dissipation, W_d, in the TC composite is eighteen times larger than fine grain fully dense pure Ti_3SiC_2 and three times larger than pure NiTi. The superb energy dissipation capacity of the composite is attributed to the dislocations and other defects formed due to thermo-mechanical cycling leading to more twin boundary motion in addition to the reasons listed for the AS composite. At this time, this hypothesis is unsubstantiated with experimental results and the need for specially designed experiments and finite element modeling cannot be overemphasized.

Joining and Microstructural Characterization of Interface:

- Successful bonding between bulk NiTi and Ti_3SiC_2 components using solid state diffusion was realized in the temperature range of 800-1000°C for the times of 1 to 10 hours except at 800°C, 1 hour. Possibly, a sub-micron reaction layer forms at the interface at 800°C after 1 hour, but was unable to withstand the thermal residual stresses generated during cooling to the room temperature, leading to debonding.
- The reaction phases in the NiTi-Ti_3SiC_2 interface were characterized and the reaction mechanisms were proposed. Three uniform, distinct layers of Ti_2Ni, Ti_5Si_3, NiTiSi phases were formed between NiTi and Ti_3SiC_2, thus making the interfacial structure of the form NiTi / Ti_2Ni / Ti_5Si_3 / NiTiSi / Ti_3SiC_2.
- The overall reaction layer thickness grows as a square root of the time at each temperature indicating that mechanism of solid state diffusion in the interface follows a parabolic kinetic law. Diffusion of Si into NiTi from Ti_3SiC_2 and Ni from NiTi into the reaction zone is responsible for the formation of reaction layers in the interface and thus the bonding at these conditions. However, the rate limiting step is diffusion of Si from Ti_3SiC_2.

Mechanical Characterization of Interface:

- Nano-indentation results show that the elastic moduli of the phases in the interface are higher than that of NiTi and close to that of Ti_3SiC_2. An average elastic modulus of 278.68 ± 10.02 GPa is obtained for the interface as compared to 91.62 ± 11.16 GPa for NiTi and 263.21 ± 31.89 GPa for Ti_3SiC_2. The hardness

of the phases in the interface is higher than that of Ti_3SiC_2 and NiTi. An average hardness of 17.55 ± 0.95 GPa is obtained for the interface as compared to 5.44 ± 0.73 GPa for NiTi and 11.86 ± 1.80 GPa for Ti_3SiC_2.

- Vicker's micro-hardness tests are employed for qualitative mechanical characterization of the NiTi-Ti_3SiC_2 interface. The indents obtained by Vickers test near the interface region lead to cracks which terminate at the interface. Secondary zigzag crack patterns are also observed in the interface indicating a good resistance to the crack propagation. However, quantitative analysis of fracture toughness measurements is needed to effectively comment on the mechanical properties of the interface.

Fracture Toughness of Interface:

- NiTi starts to deform plastically in the region between the inner loading points prior to crack propagation. Thus, critical strain energy release rate of the interface cannot be obtained using analytical equations 1-5 obtained by linear elastic fracture mechanics. A part of available energy is being dissipated through the nonlinear deformation of NiTi and the rest is being spent in crack propagation.
- NiTi is predicted to detwin between the inner loading points at an applied load of 110 N and the first critical load drop occurs at 135 N. Detwinning of NiTi between the inner loading points is one of the reasons for the observed increasing R-curve behavior in NiTi-Ti_3SiC_2 bilayer system.

- The minimum interfacial critical strain energy release rate (G_c) for the NiTi-Ti_3SiC_2 bilayer system is 115 J/m^2 and qualitatively, G_c value comparable to that of Ti_3SiC_2 for a phase angle ψ value of 75°. This G_c value is obtained by using the load at which NiTi yields between the inner loading points, prior to crack propagation. As interfaces are critical in determining the overall properties of the composite, the fact that NiTi-Ti_3SiC_2 material system forms strong reaction layer is useful in fabricating tough NiTi/Ti_3SiC_2 composites.
- Fracture occurs along the interface between Ti_3SiC_2 and NiTiSi phase, inside the Ti_3SiC_2 phase and also in the different phases in the reaction layer. It is also observed to alternate between the Ti_3SiC_2 layer and along the interface between NiTiSi and Ti_3SiC_2. Secondary cracks are also observed and they propagate through the reaction layer terminating on reaching NiTi.
- Reasons for the observed R curve behavior in the NiTi-Ti_3SiC_2 bilayer system are as follows: 1. Higher energy dissipation due to plastic deformation of NiTi between the inner loading points far away from the crack tip, 2. Increasing R-curve behavior of MAX phases, 3. Initiation and propagation of the secondary cracks through the various layers of the interface terminating in the NiTi. 4. Crack diversion into the different reaction phases in the reaction layer and back to the weak Ti_3SiC_2–NiTiSi interface.

8.2 Future Work

Preliminary interfacial fracture toughness results obtained for one processing condition studied here suggest that it is strong and tough. In this study, microstructural characterization of various processing conditions has been done. The next question that comes to mind is how does the fracture toughness of these interfaces obtained under different processing condition compare to that of studied here. One way answer is to build on the results of this study which suggests that the interfacial structure between NiTi and Ti_3SiC_2 comprises of the Ti_2Ni, Ti_5Si_3 and NiTiSi intermetallic reaction phases. Under different processing parameters, temperatures and times for joining studied here, the amount of these intermetallic phases varies. For example, the processing condition of 1000°C under 10 hours selected for joining, the NiTiSi phase is the major reaction phase in the interface. This interfacial condition has been characterized using EBSD, Nanoindentation, Vickers Microhardness and mixed mode delamination beam test. By selecting the processing condition of 1000°C 5 hours, one would obtain the interfacial structure which has the Ti_5Si_3 as the major reaction phase. Thus, by characterizing this interfacial structure using above mentioned techniques, one could obtain its mechanical properties and be able to comment on which is preferred for a set of application. This way, one could obtain a processing, microstructure and property relationship between for NiTi-Ti_3SiC_2 interface.

This relationship is useful in selecting the processing parameters for the NiTi-Ti_3SiC_2 composites so as to obtain interface structure that can give possibly the highest fracture toughness of the composites. This leads us to the following set of future work

- Fracture toughness of composites, their comparison with pure MAX phases and other composites in the literature
- Energy Dissipation characterization of SMA-MAX phase composites
    - As a function of temperature, in complete austenite phase and when both phases, austenite-martensite, coexist, by cyclic mechanical loading
    - As a function of frequency, strain amplitude and temperature, under isothermal conditions, using dynamic mechanical analysis (DMA)
- Further detailed investigation in the ability of SMAs to tune/improve the properties of MAX phases such as damping, fracture toughness and compressive strength, through selective thermomechanical loading path, based on the exciting preliminary results obtained in this study
- Similar study on fabrication and characterization of HTSMAs (NiTiHf, NiTiZr) and MAX phase composites and bilayer for high temperature applications. Results obtained in the current NiTi-MAX phase composite study would serve as a guideline for future work.

REFERENCES

[1] J. Zhang, R. J. Perez, E. J. Lavernia, Journal of Material Science, 1993, 28, 2395–2404

[2] J. Zhang, R. J. Perez, C. R. Wong, E. J. Lavernia, Materials Science and Engineering, 1994, R13, 325–390

[3] J.V. Humbeeck, Journal of Alloys and Compounds, 2003, 355, 58-64

[4] M.W. Barsoum, T. Zhen, S.R. Kalidindi, M. Radovic, A. Murugaiah, Nature Materials, 2003, 2, 107–111

[5] M. Radovic, M.W. Barsoum, A. Ganguly, T. Zhen, P. Finkel, S.R. Kalidindi, E. Lara-Curzio, Acta Materialia, 2006, 54, 2757-2767.

[6] T. W. Clyne, P. J. Withers, An Introduction to Metal Matrix Composites, Great Britain, Cambridge University Press; 1993

[7] G. Cam, M. Kak, International Materials Reviews, 1998, 43 (1), 1–44

[8] S. Suresh, A. Mortensen, A. Needleman, Fundamentals of Metal Matrix Composites, United States of America, Butterworth-Heinemann, 1993

[9] K. K. Chawla, Ceramic Matrix Composites, Great Britain, Cambridge University Press, 1993

[10] S. Suresh, C. F. Shih, A. Morrone, N. P. O'Dowd, Journal of American Ceramic Society, 1990, 73 (5), 1257–67

[11] T. Duerig, A. Pelton, D. Stockel, Materials Science and Engineering A, 1999, 149, 273–275

[12] J.V. Humbeeck, Materials Science and Engineering A, 1999, 134, 273–275

[13] J. M. Jani, M. Leary, A. Subic, M. A. Gibson, Materials and Design, 2014, 56, 1078–1113

[14] K. N. Melton, General applications of shape memory alloys and smart materials. In: K. Otsuka, C.M. Wayman, editors. Shape Memory Materials, Cambridge University Press, 1999, 220–239

[15] S. D. Oehler, D. J. Hartl, R. Lopez, R. J. Malak, D. C. Lagoudas, Smart Materials and Structures, 2012, 21, 094016

[16] D. J. Hartl, D. C. Lagoudas, F. T. Calkins, J. H. Mabe, Smart Materials and Structures, 2010, 19, 015020

[17] D. J. Hartl, D. C. Lagoudas, F. T. Calkins, J. H. Mabe, Smart Materials and Structures, 2010, 19, 015021

[18] D. Stockel, The shape memory effect: phenomenon, alloys, applications, In: Shape memory alloys for power systems, EPRI, 1995, 1–13

[19] T. Duerig, Applications of shape memory, In: Materials science forum, Switzerland: Trans Tech Publication, 1990, 679–692

[20] M. H. Wu, L. M. Schetky, Industrial applications for shape memory alloys, In: International conference on shape memory and superelastic technologies, Pacific Grove, California, USA, 2000, 171–182

[21] D. Stoeckel, T. Waram, Use of Ni–Ti shape memory alloys for thermal sensor actuators, In: Active and adaptive optical components. San Diego, CA, USA, international society for optics and photonics, 1992, 382–387

[22] D. J. Hartl, B. Volk, D. C. Lagoudas, F. T. Calkins, J. Mabe**,** In Proceedings of ASME, International Mechanical Engineering Congress and Exposition (IMECE), Chicago, IL, 2006, 1–10

[23] D. J. Hartl, D. C. Lagoudas, Proceedings of the Institution of Mechanical Engineers, Part G: Journal of Aerospace Engineering, 2007**,** 221 (4), 535-552

[24] O. J. Godard, M. Z. Lagoudas, D. C. Lagoudas, Design of space systems using shape memory alloys, In: Smart structures and materials: international society for optics and photonics, 2003, 545–558

[25] B. Huettl, C. E. Willey, Design and development of miniature mechanisms for small spacecraft, 14th AIAA/USU Conference on Small Satellites, 1–14

[26] A. D. Johnson, Non-explosive separation device, In: US Patents 5119555, 1992

[27] H. Qian, H. N. Li, G. Song, H. Chen, W. J. Ren, S. Zhang, Earth and Space, Engineering, Science, Construction, and Operations in Challenging Environments, 2010 American Society of Civil Engineers, 3377–3395

[28] M. Dolce, D. Cardone, R. Marnetto, Smart Structures and Materials, 2001: Smart Systems for Bridges, Structures, and Highways, S. C. Liu, Editor, Proceedings of SPIE, 2001, 4330, 238–249

[29] M. Dolce, D. Cardone, R. Marnetto, Earthquake Engineering and Structural Dynamics, 2000, 29 (7), 945–968

[30] J. Ma, I. Karaman, R. D. Noebe, International Materials Reviews, 2010, 55 (5), 257–315

[31] S. Saadat, J. Salichs, M. Noori, Z. Hou, H. Davoodi, I. Bar-on, Y. Suzuki and A. Masuda, Smart Materials and Structures, 2002, 11, 218–229

[32] K. Bhattacharya, R.V. Kohn, Acta Materialia, 1996, 44, 529

[33] P.K. Kumar, D. Lagoudas, Shape memory alloys: modeling and engineering applications, Ed. D. Lagoudas, New York, Springer, 2008

[34] I. Saburi, S. Nenno Scripta Metallurgica, 1974, 8, 1363

[35] Y. Liu, Y. Liu, J. V. Humbeeck, Acta Materialia, 1999, 47, 19

[36] S. Eucken, T. W. Duerig, Acta Metallurgica, 1989, 37, 2245

[37] Y. Liu, Z. Xie, J.V. Humbeeck, Materials Science and Engineering A, 1999, 273–275, 673–678

[38] R. R. Hasiguti, K. Iwasaki, Journal of Applied Physics, 1968, 39, 2182–2186

[39] W. Dejonghe, R. D. Batist, L. Delaey, M. D. Bonte, J. Perkins, Shape Memory Effects in Alloys, Ed. J. Perkins, Plenum Press, New York, 1975, 451–66.

[40] O. Mercier, K.N. Melton, Y. D. Preville, Acta Metallurgica, 1979, 27, 1467-1475

[41] Y. T. Huang, G. P. Yang, P. He, Scripta Metallurgica, 1985, 19, 1033–1038

[42] Y. T. Huang, G. P. Yang, P. He, Scripta Metallurgica, 1985, 19, 1039–1044

[43] S. K. Wu, H. C. Lin, T. S. Chou, Acta Metallurgica, 1990, 38, 95–102

[44] K. Iwasaki, and R.R. Hasiguti, Transactions of Japan Institute of Metals, 1987, 28, 363–367.

[45] W. Dejonghe, L. Delaey, R. D. Batist, J. V. Humbeeck, Metal Science, 1977, 11, 523–530

[46] H. C. Lin, S. K. Wu, M. T. Yeh, Metallurgical Transactions A, 1993, 24, 2189–2194

[47] K. Sugimoto, T. Mori, K. Otsuka, K. Shimizu, Scripta Metallurgica, 1974, 8, 1341–1348.

[48] M. W. Barsoum, Progress in Solid State Chemistry, 2000, 28, 201–281

[49] M. W. Barsoum, T. El-Raghy, American Scientist, 2001, 89, 334–343

[50] http://max.materials.drexel.edu/wpcontent/uploads/2010/05/MaxPhases PTable.jpeg

[51] M. W. Barsoum, H. I. Yoo, I. K. Polushina, V. Y. Rud, Y. V. Rud, T. El-Raghy, Physical Review B, 2000, 62, 10194–10196

[52] T. El-Raghy, M. W. Barsoum, A. Zavaliangos, S. R. Kalidindi, Journal of American Ceramic Society, 1999, 82, 2855–2860

[53] M. W. Barsoum, T. El-Raghy, and L. U. J. T. J. Ogbuji, Journal of The Electrochemical Society, 1997, 144 (7), 2508–2516

[54] J. D. Hettinger, S. E. Lofland, P. Finkel, T. Meehan, J. Palma, K. Harrell, S. Gupta, A. Ganguly, T. El-Raghy, M. W. Barsoum, Physical Review B, 2005, 72, 1151201-1151206

[55] J. M. Schneider, D. P. Sigumonrong, D. Music, C. Walter, J. Emmerlich, R. Iskandar, and J. Mayer, Scripta Materialia, 2007, 57, 1137–1140

[56] M. Radovic, M. W. Barsoum, T. El-Raghy, S. Wiederhorn, Acta Materialia, 2001, 49, 4103–4112

[57] M. Radovic, M. W. Barsoum, T. El-Raghy, J. Seidensticker, S. M. Wiederhorn, Acta Materialia, 2000, 48, 453–459

[58] M. Radovic, M. W. Barsoum, T. El-Raghy, S. M. Wiederhorn, W.E. Luecke, Acta Materialia, 2002, 50, 1297–1306

[59] Z. Sun, Y. Zhou, M. Li, Corrosion Science, 2001, 43, 1095–1109

[60] M. W. Barsoum, M. Radovic, Annual Review of Materials Research, 2011, 41, 195–227

[61] A. G. Zhou, S. Basu, M. W. Barsoum, Acta Materialia, 2008, 56, 60–67

[62] F. Barcelo, S. Doriot, T. Cozzika, M. L. Flem, J. L. Bechade, M. Radovic, M. W. Barsoum, Journal of Alloys and Compounds, 2009, 488, 181

[63] M. Radovic, M. W. Barsoum MW, T. El-Raghy, S. Wiederhorn, Journal of Alloys and Compounds, 2003, 361, 299

[64] Z. M. Sun, International Materials Reviews, 2011, 56 (3), 143

[65] G. Guilera, B. Gorges, S. Pascarelli, H. Vitoux, M. A. Newton, C. Prestipino, Y. Nagai and N. Hara: Journal of Synchrotron Radiation, 2009, 16, 628–634

[66] S. Gupta, D. Filimonov, T. Palanisamy, T. El-Raghy and M. W. Barsoum: Wear, 2007, 262, 1479–1489

[67] M. Sundberg, G. Malmqvist, A. Magnusson, T. El-Raghy, Ceramics International, 2004, 30, 1899

[68] S. L. Shi, W. Pan, M. H. Fang, Z. Y. Fang, Journal of American Ceramic Society, 2006, 89, 743–745

[69] N. F. Gao, Y. Miyamoto, H. Oonishi, D. Zhang, Journal of Materials Science Letters, 2002, 21, 783–785

[70] J. Lis, L. Chlubny, M. Lopacinski, L. Stobierski, M. A. Buck, Journal of European Ceramic Society, 2008, 28, 1009

[71] W. T. Lo, C. A. Jeng, J. L. Huang, H. H. Lu, D.F. Lii, Journal of Alloys and Compounds, 2008, 455, 413

[72] X. H. Wang, Y. C. Zhou, Journal of Materials Science & Technology, 2010, 26(5), 385–416

[73] C. J. Gilbert, D. R. Bloyer, M. W. Barsoum, T. El-Raghy, A. P. Tomsia, R. O. Ritchie, 2000, Scripta Materialia, 238, 761–67

[74] P. L. Swanson, C. J. Fairbanks, B. R. Lawn, Y. -W. Mai, B. J. Hockey, Journal of American Ceramic Society, 1987, 70, 279

[75] C. W. Li, D. J. Lee, S. C. Lui, Journal of American Ceramic Society, 1992, 75, 1777

[76] C. J. Gilbert, R. O. Ritchie, Acta Materialia, 1998, 46, 609

[77] D. Chen, K. Shirato, M. W. Barsoum, T. El-Raghy, R. O. Ritchie, Journal of American Ceramic Society, 2001, 84 (12), 2914–2920

[78] M. W. Barsoum, T. Zhen, A. Zhou, S. Basu, S. R. Kalidindi, Physical Review B - Condensed Matter and Materials Physics,2005, 71, 1–8

[79] M. W. Barsoum, M. Radovic, T. Zhen, P. Finkel, S. R. Kalidindi, Physical Review Letters, 2005, 94, 1–4

[80] S. R. Kalidindi, T. Zhen, M. W. Barsoum, Materials Science and Engineering A, 2006, 418, 95–98

[81] A. G. Zhou, S. Basu, G. Friedman, P. Finkel, O. Yeheskel, M. W. Barsoum, Physical Review B - Condensed Matter and Materials Physics, 2010, 82, 094105-1–10

[82] B. Poon, L. Ponson, J. Zhao, G. Ravichandran, Journal of the Mechanics and Physics of Solids, 2011, 59, 2238–2257

[83] N. G. Jones, C. Humphrey, L. D. Connor, O. Wilhelmsson, L. Hultman, H. J. Stone, F. Giuliani, W. J. Clegg, Acta Materialia, 2014, 69, 149–161

[84] R. Benitez, W. H. Kan, H. Gao, M. O'Neal, G. Proust, M. Radovic, Room Temperature Stress-Strain Hysteresis in Ti_2AlC Revisited, Acta Materialia, under review

[85] J. A. Fernie, R. A. L. Drew, K. M. Knowles, International Materials Reviews, 2009, 54 (5), 283

[86] Y. Zhou, Z. Sun, Journal of Physics-Condensed Matter, 2000, 12, L457–462

[87] S. Basu, M. F. Ozaydin, A. Kothalkar, I. Karaman, M. Radovic, Scripta Materialia, 2011, 65, 237–240

[88] J. Zhang, J. Y. Wang, Y. C. Zhou, Acta Materialia, 2007, 55, 4381–4390

[89] T. L. Ngai, W. Zheng, C. Hu, H. Xie, Y. Li, Advanced Materials Research, 2011, 211-212, 1051–1055

[90] N. F. Gao, Y. Miyamoto, Journal of Materials Research, 2002, 17, 52–59

[91] X. H. Yin, M. S. Li, Y. C. Zhou, Journal of Materials Research, 2006, 21(9), 2415–2421

[92] O. Dezellus, R. Voytovych, A. P. H. Li, G. Constantin, F. Bosselet, J. C. Viala, Journal Of Materials Science, 2010, 45, 2080–2084

[93] T. El-Raghy, M. W. Barsoum, M. Sika, Materials Science and Engineering A, 2001, 298, 174–178

[94] W. L. Gu, C. K. Yan, Y. C. Zhou, Scripta Materialia, 2003, 49, 1075–1080

[95] W. L. Gu, Y.C. Zhou, Transactions of the Nonferrous Metals Society of China, 2006, 16, 1281–1288

[96] M. S. Hu, A. G. Evans, Acta Metallurgica, 1989, 37 (3), 917–925

[97] T. S. Oh, J. Rodel, R. M. Cannon, R. O. Ritchie, Acta Metallurgica, 1988, 36 (8), 2083–2093

[98] R. Xu, X. L. Fan, W. X. Zhang, Y. Song, T. J. Wang, Materials and Design, 2013, 47, 566–574

[99] J. W. Hutchinson, H. Suo, Advances in Applied Mechanics, 1992, 29, 63

[100] K. Kendall, Proceedings of the Royal Society A, 1975, 344, 287

[101] K. Kendall, Proceedings of the Royal Society of London, 1975, 341, 409

[102] J. W. Hutchinson, M. E. Mear, J. R. Rice, Journal of Applied Mechanics, 1987, 54 (4), 828–832

[103] A. G. Evans, J. W. Hutchinson, Acta Metallurgica, 1989, 37, 909

[104] M. -Y. He, J. W. Hutchinson, Journal of Applied Mechanics, 1989, 56, 270

[105] Y. -H. Chiao, D. R. Clark, Acta Metallurgica, 1989, 37, 251

[106] M. -Y. He, J. W. Hutchinson, International Journal of Solids and Structures, 1989, 25, 1053

[107] P. P. L. Matos, R. M. McMeeking, P. G. Charalambides, M. D. Drory, International Journal of Fracture, 1990, 40, 235

[108] A. G. Evans, M. Ruhle, B. J. Dalgleish, P. G. Charalambides, Materials Science and Engineering A, 1990, 126, 53

[109] N. A. Fleck, J. W. Hutchinson, Z. Suo, International Journal of Solids and Structures, 1991, 27, 1683

[110] A. G. Evans, B. J. Dalgleish, M. Y. He, J. W. Hutchinson, Acta Metallurgica, 1989, 37, 3249

[111] C. Atkinson, R. E. Smelser, J. Sanchez, International Journal of Fracture, 1982, 18, 279

[112] H. C. Cao, A. G. Evans, Mechanics of Materials, 1989, 7, 295

[113] P. G. Charalambides, J. Lund, A. G. Evans, R. M. McMeeking, Journal of Applied Mechanics, 1989, 56, 77

[114] M. Y. He, Acta Metallurgica, 1990, 38, 839

[115] P. G. Charalambides, H. C. Cao, J. Lund, A. G. Evans, Mechanics of Materials, 1990, 8, 269

[116] J. -S. Wang, Z. Suo, Acta Metallurgica, 1990, 38, 1279

[117] R. J, Kearns, T. A. Parathasarathy, Journal of American Ceramic Society, 1991, 74, 1585

[118] Z. G. Wei, R. Sandstrom, S. Miyazaki, Journal of Materials Science, 1998, 33, 3763

[119] C. A. Rogers, D. K. Barker, In Proceedings of the 31st AIAA/ASME/ASCE/AHS/ASC Structures, Structural Dynamics and Materials Conference, 1990, 2234

[120] C. A. Rogers, C. R. Fuller, C. Liang, Journal of Sound and Vibration, 1990, 136 (1), 164

[121] J. S. N. Paine, C. A. Rogers, In Proceedings of the American Society of Mechanical Engineers, Aerospace Division, ASME, 1994, 54

[122] Idem, in Proceedings of the American Society of Composites 3rd Technical Conference on Composite Materials Technomic, Lancaster, 1988, 719

[123] Idem, Journal of the Acoustical Society of America, 1990, 88, 2803

[124] Y. Furuya, A. Sasaki, M. Taya, Materials Transactions JIM, 1996, 34 (3), 224

[125] W. D. Armstrong, H. Kino, Journal of Intelligent Material Systems and Structures, 1995, 6, 809

[126] K. Escher, E. Hornbogen, J Phys I 1991, 1, C4Đ427

[127] R. Barrett, R. S. Gross, Smart Materials & Structures, 1996, 5, 255

[128] Y. Furuya, A. Sasaki, M. Taya, Materials Transactions JIM, 1993, 34, 224

[129] Y. Furuya, Journal of Intelligent Material Systems and Structures, 1996, 7, 321

[130] E. R. Strutt, E. A. Olevsky, M. A. Meyers, Journal of Materials Science, 2008, 43, 6513

[131] E. R. Strutt, T. Radetic, E. A. Olevsky, M. A. Meyers, Journal of Materials Science, 2008, 43, 5905

[132] X. Zhang, G. Lu, M. J. Hoffmannc, R. Metselaar, Journal of European Ceramic Society, 1995, 15, 225

[133] D. Mari, D. C. Dunand, Metallurgical and Materials Transactions A, 1995, 26, 2833

[134] D. Mari, L. Bataillard, D. C. Dunand, R. Gotthardt, J Phys IV 1995: 5: 659

[135] K. L. Fukami-Ushiro, D. C. Dunand, Metallurgical and Materials Transactions A, 1996, 27, 183

[136] K. L. Fukami-Ushiro, D. Mari, D. C. Dunand, Metallurgical and Materials Transactions A, 1996, 27, 193

[137] D. C. Dunand, D. Mari, M. A. M. Bourke, J. A. Goldstone, J Phys IV 1995: 5 C8: 653

[138] D. C. Dunand, D. Mari, M. A. M. Bourke, J. A. Roberts, Metallurgical and Materials Transactions A, 1996, 27, 2820

[139] K. Johansen, H. Voggenreiter, G. Eggeler, Materials Science and Engineering A, 1999, 273–275, 410

[140] R. Vaidyanathan, D. C. Dunand, U. Ramamurty, Materials Science and Engineering A, 2000, 289, 208

[141] P. Filip, J. Musialek, K. Michalek, M. Yen, K. Mazanec, Materials Science and Engineering A, 1999, 273–275, 769

[142] Z. Xiu, J. Laeng, X. Suna, Q. Li, S. K. Hur, Y. Liu, Journal of Alloys Compounds, 2008, 458, 398

[143] Y. Yamada, M. Taya, R. Watanabe, Materials Transactions JIM, 1993, 34, 254

[144] Y. Zhang, Z. Sun, Y. Zhou, Materials Research Innovations, 1999, 3, 80–84

[145] Y. C. Zhou, B. Q. Chen, X.H. Wang, C. K. Yan, Materials Science and Technology, 2004, 20, 661–665.

[146] Z. Zhang, S. Xu, Rare Metals, 2007, 26, 359–364

[147] L. M. Peng, Scripta Materialia, 2007, 56, 729–732

[148] J. Zhang, Y. C. Zhou, Journal of Materials Research, 2008, 23, 924–932

[149] J. Y. Wu, Y. C. Zhou, J. Y. Wang, Materials Science and Engineering A, 2006, 422, 266–71

[150] W. J. Wang, V. Gauthier-Brunet, G. P. Bei, G. Laplanche, J. Bonneville, A. Joulain, S. Dubois, Materials Science and Engineering A, 2011, 530, 168–173

[151] H. Li, L. M. Peng, M. Gong, L. H. He, J. H. Zhao, Y. F. Zhang, Materials Letters, 2005, 59, 2647–2649

[152] S. Amini, C. Ni, M. W. Barsoum, Composites Science and Technology, 2009, 69, 414–420

[153] S. Amini, M. W. Barsoum, Materials Science and Engineering A, 2010, 527, 3707–3718

[154] ASTM C20-00, Standard test methods for apparent porosity, water absorption, apparent specific gravity, and bulk density of burned refractory brick and shapes by boiling water, ASTM International, West Conshohocken, PA, 2010

[155] Z. G. Wei, R. Sandstrom, S. Miyazaki, Journal of Materials Science, 1998, 33, 3743–62.

[156] J. L. Murray, Ni–Ti (nickel–titanium), in: T.B. Massalski (Ed.), Binary Alloy Phase Diagrams, 1990, 3, 2874–2876

[157] M. G. Nicholas, Joining Processes, The Netherlands, Kluwer Academic Publishers, 1998

[158] ASTM F2004-05, Standard test method for transformation temperature of nickel–titanium alloys by thermal analysis, ASTM International, West Conshohocken, PA, 2004

[159] L. Hu, A. Kothalkar, I. Karaman, M. Radovic, Journal of Alloys and Compounds, 2014, 610, 635–644

[160] H. C. Lin, S. K. Wu, Metallurgical Transactions A, 1993, 24 (2), 293–299

[161] B. T. Lester, Y. Chemisky, D. C. Lagoudas, Smart Materials & Structures, 2011, 20, 094002-1–13

[162] R. J. Salzbrenner, M. Cohen, Acta Metallurgica, 1979, 27, 739–748

[163] A. Hedayat, J. Rechtien, K. Mukherjee, Journal of Materials Science, 1992, 27, 5306–5314

[164] P. Sittner, D. Vokoun, G. N. Dayananda, R. Stalmans, Materials Science and Engineering A, 2000, 286, 298–311

[165] M. Morin, G. Guenin, Journal de Physique Colloques, 1983, 44 (C9), 247–52

[166] S. Rajagopalan, A. L. Little, M. A. M. Bourke, R. Vaidyanathan, Applied Physics Letters, 2005, 86, 081901-1–3

[167] M. Vogelsang, R. Arsenault, R. Fisher, Metallurgical Transactions, 1986, 17, 379–89

[168] D. Dunand, A. Mortensen, Acta Metallurgica Et Materialia, 1991, 39, 127–139

[169] E. Carreno-Morreli, S. E. Urreta, R. Schaller, Acta Materialia, 2000, 48, 4725–4733

[170] A. G. Zhou, M. W. Barsoum, S. Basu, S. R. Kalidindi, T. El-Raghy, Acta Materialia, 2006, 54, 1631–1639

[171] M. Fraczkiewicz, A. G. Zhou, M. W. Barsoum, Acta Materialia, 2006, 54, 5261–5270

[172] R. Schaller, G. Fantozzi, G. Gremaud (Ed.), Mechanical Spectroscopy Q-1 2001: with Applications to Material Science, Trans Tech Publications Limited, Switzerland, 2001, 382–415

[173] S. Kustov, S. Golyandin, K. Sapozhnikov, J. V. Humbeeck, R. D. Batist, Acta Materialia, 1998, 46, 5117–5126

[174] E. Carreno-Morreli, Metallurgical and Materials Transactions A, 2004, 35, 25–35

[175] Y. Du, C. He, J. C. Schuster, S. Liu, H. Xu, International Journal of Materials Research, 2006, 97, 543

[176] N. Lebrun, G. Effenberg, S. Ilyenko (Eds.) Germany, Springer Materials - The Landolt-Bornstein Database, 2006

[177] W. C. Oliver, G. M. Pharr, Journal of Materials Research, 2004, 19, 3

[178] N. F. Gao, Y. Miyamoto, D. Zhang, Journal of Materials Science, 1999, 34, 4385

[179] B. J. Kooi, R. J. Poppen, N. J. M. Carvalho, J. Th. M. D. Hosson, M. W. Barsoum, Acta Materialia, 2003, 51, 2859–2872

[180] R. Pampuch, J. Lis, L. Stobierski, M. Tymkiewicz, Journal of European Ceramic Society, 1989, 5, 283

[181] M. W. Barsoum, T. El-Raghy, Journal of American Ceramic Society, 1996, 79, 1953

[182] T. El-Raghy, A. Zavaliangos, M. W. Barsoum, S. R. Kalidindi, Journal of American Ceramic Society, 1996, 80, 513

[183] A. Procopio, M. W. Barsoum, T. El-Raghy, Metallurgical and Materials Transactions A, 2000, 31, 333

[184] N. Tzenov, M. W. Barsoum, Journal of American Ceramic Society, 2000, 83, 801

[185] Keith Ballard Thesis, Department of Aerospace Engineering, Texas A&M University, College Station, 2015 [unpublished work]

[186] H. F. Wang, W. W. Gerberich, C. J. Skowronek, Acta Metallurgica Et Materialia, 1993, 41 (8), 2425–2432

[187] S. J. Howard, A. J. Phillipps, T. W. Clyne, Composites, 1993, 24 (2), 103

[188] A. J. Phillipps, W. J. Clegg, T. W. Clyne, Composites, 1992, 24 (2), 166–176

[189] T. L. Anderson, Fracture Mechanics: fundamentals and applications, USA, CRC Press, 2005

[190] A. J. Phillipps, W. J. Clegg, T. W. Clyne, Acta Metallurgica Et Materialia, 1993, 41 (3), 819–827,

[191] N. W. Klingbeil, J. L. Beuth, Engineering Fracture Mechanics, 1997, 113–126

[192] I. E. Reimanis, B. J. Dalgleish, M. Brahy, M. Ruhle, A. G. Evans, Acta Metallurgica Et Materialia, 1990, 38 (12), 2645–2652

[193] B. J. Dalgleish, K. P. Trumble, A. G. Evans, Acta Metallurgica, 1989, 37 (7), 1923–1931